DEPARTMENT OF PHYSICS

JANUARY 2023

THERMOELECTRIC PROPERTIES OF ORGANIC THIN FILMS FABRICATED BY THERMAL SUBLIMATION AND SOLUTION SELF-ASSEMBLY

SOPHIE AU-YONG

A thesis submitted for the degree of Doctor of Philosophy

January 2023

Declaration

I declare that the thesis has been composed by myself and that the work has not been submitted for any other degree or professional qualification. I confirm that the work submitted is my own, except where states otherwise by reference or acknowledgement.

Abstract

As the nanotechnology industry continues to find ways to further the miniaturisation of electronic components a single chip, alternative methods and materials are being explored. This poses new challenges for the scientific community. Due to their size which allows for alternative transport mechanisms to occur, molecular electronics have gained much traction in the community and in particular, their thermoelectric properties have gained attention due to their unusual phenomena, showing their potential to substitute typical semiconductor materials.

Organic molecules were carefully selected to be deposited on an Au(111) surface either under an ultra-high vacuum (UHV) environment or in solution self-assembly (SA) to form self-assembled monolayers (SAMs). These two methods were proven to produce high-quality films. The advantages of these two methods are highlighted throughout this thesis with the support of the topography obtained through atomic force microscopy (AFM). AFM in combination with X-ray photoelectron (XPS) can provide vital information about the structural composition of the monolayers and their interaction with the surface, allowing the conformation to be deduced. AFM can be adapted to study the conductive properties of "softer" (C-AFM) materials without damaging the conformation and properties.

This thesis studies a series of dialkynylferrocenes which exhibit attractive electronic and rotational properties. Previously, work on these molecules was carried out on single molecular junctions whereas here, properties of the SAM were investigated and deposited via solution. The single molecular junctions showed that the molecules adopt an 'open' conformation as opposed to the self-assembled monolayer where it preferentially forms a 'hairpin' conformation (both alkynes pointing to the surface).

Using the same deposition method, a series of parallel anthracene molecules were explored. These molecules offer the potential to harvest energy at room temperature and their thermoelectric properties can be tuned due to their quantum interference effects. These 'sticky' anthracene bases are bound to the metal electrodes through their anchor groups and underwent further deposition to form a 3D architecture using zinc porphyrin as its 'slippery' linker.

Taking inspiration from the 'slipper linkers' concept, the following chapter shows zinc porphyrin deposited via thermal sublimation to form a highly pristine base monolayer. Two derivatives of bipyridine were studied as the potential for a linker to the zinc centre of the porphyrin. Deposition methods of the second layer were attempted with both thermal sublimation and solution self-assembly.

The findings presented in this research demonstrate that well-ordered self-assembled monolayers can be formed using two different methods of deposition: thermal sublimation and solution self-assembly. It is found that these molecular structures and their interactions with the surface can greatly alter the thermoelectrical and electrical properties leading to exciting and novel ways of fabrication methods highlighting the importance of molecular structures within a monolayer.

Contents

Chapter 1

Introduction

Throughout history, energy has played an important role in society. Energy comes in many different forms such as chemical, electrical, mechanical, thermal and more. Wind, fire and humans were the basic types of energies exploited that created the world we live in. Past methods of harnessing energy have evolved greatly, from steam-powered devices to nuclear power stations. The decrease in the abundance of non-renewable sources has caused a massive change in how we are doing things today. Besides depletion of these sources, it is also damaging to the environment to use them. Climate change is one of the main global issues of our time, and a lot of attention has been focused on reducing our carbon footprints as individuals and a population as a whole. Renewable energies have been considered a vital alternative for slowing down climate change and thus, much research has gone into finding the most efficient yet affordable way to advance the field. Whilst it is practical to think about the cost, it is also necessary to evaluate the consequences that come from harnessing energy, using it and storing it from the beginning to obtain a true idea of 'sustainability'.

One of the most important forms of energy we rely on today is electrical energy, i.e. that which is converted from electric potential into other useful work. Almost every aspect of our lives in virtually every part of the world now relies on electrical energy of some form. Considered at a general level, electrical energy is probably the most versatile energy type able to be converted into other, less noble forms, such as kinetic (mechanical), light, and their various subdivisions. Converting to and

from each energy type is not always practical and will always result in losses due to the second law of thermodynamics. Ultimately then, all energy eventually turns, or indeed is lost into heat, causing us to regard heat as the lowest 'quality' form of useful work despite this it generates more than 90% of energy usage.[1]

How can we avoid or even recover this 'lost' useful energy? The thermoelectric effect is one such phenomenon that has significant application in this area. Thermoelectric (TE) materials are a simple technology that can directly convert heat to electricity and has gained widespread attention for their potential applications as mini-cooling systems, TE generators, and self-powered sensors.[2] They are attractive materials as they enable heat to be converted back into electric voltage, utilising, for instance, waste heat as mentioned above from natural sunlight, automobiles, central processing units (CPUs), human heat etc., thus exploiting a huge range of energies that are already present. Research into thermoelectric materials, therefore, focuses on 1) improving the efficiency of such materials, and 2) developing materials that are cheap and 3) industrially viable.

1.1 An Example of Thermoelectricity

Thinking about sustainability in terms of energy or devices involves taking into account the energy required to obtain the end product. For example, the energy used to create a mobile phone is very large. Major components include the display unit, CPU and battery. The CPU is mostly made up of silicon and the process of extracting pure silicon from silicon dioxide involves heating it at high temperatures at around 2200°C with carbon. This takes 1000-1500 MJ/kg, also known as embodied energy. (Compared to that of aluminium which uses around 170 MJ/kg).[3] The embodied energy can also go even further back in the manufacturing process and account for the energy in getting the energy in the first place. If silicon dioxide was heated using oil, what would the energy be for transporting the oil from one country to another? The complication with calculating embodied energy is how far back would you stop.

The amount of energy used is governed by the way society behaves. As our everyday lives have incorporated the use of electricity, the higher demand from consumers

means higher supply. One method of reducing the supply and still meeting demands is to increase the efficiency resulting in the amount necessary to decrease but due to Jevon's paradox (the rebound effect) which states that as a process becomes more efficient, the consumption increases thus, a rise in demand.[4] The infrastructure of societies allows the rebound to arise at a faster rate and consequently the demand eventually increases to a point where we end up consuming more than we did when it was less efficient. This can also be true for the use of thermoelectrics, e.g. in phones. Normal working phone temperatures operate between 25-30°C but can get up to ∼50°C and if some of that waste heat can be converted into electricity to power our phones then less power is needed for charging our phones.[5] Although if we apply Jevons paradox, similarly to what we commonly see from battery development, we can expect rather than a reduction in energy use, an increase in the capabilities of the phone meaning that no energy is saved at all.

The opposite of embodied energy is energy output or exergy from a particular source. It is the amount of usable or available energy. In devices that release energy such as thermoelectric devices, Li-ion batteries and solar panels, an estimation of efficiency can be determined by the ratio between the energy input and the output and is also known as energy return on investment (EROI). The benefits will outweigh the costs (in terms of energy) if the ratio is at least 3:1.[6]

The efficiency of converting heat into electricity in the desired end product can be predicted if the ZT of a material is known. ZT is the dimensionless figure of merit of the primary measure of a thermoelectric material's performance (synonymous with ZT_m) and helps in finding its efficiency. Most TE materials' ZT values are between 1 and 2.5.[1] If we were to take a material with a ZT of 2, theoretically the maximum efficiency of power generated, η, is:

$$\eta = \left(\frac{T_{hot} - T_{cold}}{T_{hot}}\right)\left[\frac{\sqrt{1+ZT_m}-1}{\sqrt{1+ZT_m}+\left(\frac{T_{cold}}{T_{hot}}\right)}\right] \tag{1.1}$$

[7]

where T_m, is the average temperature. This equation is a product of the Carnot efficiency $(T_{hot} - T_{cold})/T_{hot}$ and a reduction factor as a function of the material's

figure of merit, Z.[7] If we take the hot temperature of the mobile phone to be 30°C at its max and the cold to be approximately just below room temperature at 25°C. The equation simplifies to:

$$\eta = \left(\frac{5}{303}\right)\left[\frac{\sqrt{3}-1}{\sqrt{3}+0.9834}\right] = 4.4 \times 10^{-3} \times 100 = 0.44\% \tag{1.2}$$

To compare, solar thermoelectric generators also have a ZT of 2 and can achieve an efficiency of 15.9 % if the hot temperature is at 1000°C.[8] One solution could be to insert a cooling system on one side of the film to ensure a gradient though that could possibly defy the point of attempting to produce a 'green' device if we require an additional energy source for its function.

If the ZT of the material can be improved to 3, the efficiency will increase by 0.10%:

$$\eta = \left(\frac{5}{303}\right)\left[\frac{\sqrt{4}-1}{\surd+0.9834}\right] = 5.5 \times 10^{-3} \times 100 = 0.55\% \tag{1.3}$$

Following this equation and estimation of an EROI can be done by first trying to find a value for the embodied energy of the material. To make the calculations simpler, the energies included will be: the molecules and materials used (imine deposition on gold), the amount required to power a UHV (ultra-high vacuum) deposition system and the voltage applied to obtain the right temperature for molecule sublimation. Although it is difficult to find exact values to represent the energy embodied, it can be seen that this is a very energy intensive process. Synthesising pure chemicals alone (depending on the chemical) would require isolation and purification. Secondly, the energy flow from the material will be 0.23% of the energy expelled as heat from the mobile phone and finally, the EROI can be found.

When thinking about sustainability and the 'bigger picture', it is important to think about the value of the material compared to the effort put into making it. Is it worth the embodied energy as a finished product? For example, the embodied energy in making steel is around 38 MJ/kg but this embodiment allows for structures (buildings/bridges) to be built therefore increasing its value.[3]

Steel production has not always required 'little' amounts of energy. Through many years of research, today's production is far less energy intensive. So, although the embodied energy of making thermoelectric films is extremely high recently and currently does not hold the same value as solar cells, for example, research is essential in eventually producing a product in which they may be equally beneficial. Discovering a thermoelectric material which can produce a high ZT, would mean that it could find applications in many disciplines in the future. Although in this particular example we used the idea of implementing them in mobile phones, if the future of thermoelectrics can successfully be scaled down to produce sufficient EROI, the possibilities are not limited to mobile devices.

1.2 Nanoscale Thermoelectrics

Nanoscale thermoelectrics is intrinsically linked with their molecular counterparts – molecular electronics. These two communities work closely together to fully optimise the future of nanodevices. As we begin to near the end of Moore's law, the need to discover new technologies and methodologies to continue the miniaturisation of electrical components on a single chip is becoming increasingly important to obtain superior devices. And so, much of the focus in recent years has been focused on understanding devices at the nanoscale. New materials are being explored as alternatives to conventional semiconductors and molecules have piqued particular interest due to their potential arising from the possible complexity in their synthesis design and quantum properties at small sizes.

Richard Feynman's talk, 'There's plenty of room at the bottom', gathered a lot of attention about bottom-up fabrication and the current methods of building nanoscale devices.[9] Feynman proposed that if atoms can be manipulated, it would be possible to store data in an arrangement of atoms and additionally new properties could be discovered as a result. Molecules open up a wide range of possibilities, their chemical structure can be manipulated to alter their physical properties such as magnetism, electricity and thermal conductivity.

1.3 Aim and Overview of this thesis

Bringing together these two aspects, this thesis focuses on the design, fabrication and characterisation of thin-film thermoelectrics. Chapter 2 introduces the concept of thermoelectricity and introduces why nanoscale and bottom-up methods based on small molecules can be useful. Following this, Chapter 3 begins to talk about the major factors that influence molecular thermopower and the forces that are prevalent in self-assembled monolayers (SAMs). We also address the different methodologies used in this thesis for SAM deposition, vacuum and solution self-assembly. Chapter 4 details the experimental techniques and preparations required for the work carried out in the later chapters. Additionally, the characterisation methods are described here, including atomic force microscope (AFM) and its variations and X-ray photoelectron spectroscopy (XPS).

In Chapter 5, we investigate the assembly of various dialkyl ferrocene molecules using a combination of XPS and AFM. We show that the positioning of the ferrocene arms is dependent on the anchor groups and examine how this affects their electrical properties. We then begin to explore 3D molecular architectures with anthracenes and zinc tetraphenylporphyrin (ZnTPP). Here, anthracene 'sticky' linkers are deposited onto template stripped gold and proceeded to be submerged in ZnTPP solution for complexation to the anthracene as a 'slippery' linker. This chapter shows the impact of complexing a ZnTPP to an anthracene on its conductivity and thermoelectric power. We then attempt to reverse this process, forming a pristine well-ordered monolayer using planar molecules such as porphyrin and phthalocyanine as the foundation. The results are presented in Chapter 7 and we attempt to combine two different methods of deposition, vacuum deposition and solution self-assembly.

This thesis will then investigate a series of molecules and how they will self-assemble on the surface and their electrical transport properties. This work will focus on experimenting with methods and materials to fabricate molecular thin-film thermoelectrics whilst considering that the findings could be utilised for devices in the future. The overall arching aim of this thesis is then three-fold: firstly, we will test the feasibility of translating single molecular measurements to SAMs which are

needed for devices. Secondly, to discover if thermoelectrical/electrical properties of SAMs can be enhanced with phonon-suppression by pi-stacking molecules, and finally, to address whether a combination of two deposition methods can be combined to create the perfect SAMs.

Chapter 2

Thermoelectricity

2.1 Introduction

Since the emergence of Moore's law, a prediction made by Gordon Moore in 1965, where he observes that the number of transistors fabricated on a computer chip tends to double every two years, has ended, further miniaturisation of computer chips remains a great challenge. Conventionally, silicon is used for mass manufacturing, however, due to its bulk properties, uniform doping became difficult to achieve as the size of the components decreased.[10] Richard Feynman's talk, 'There's plenty of room at the bottom', could be considered as one of the major inspirations for investigating molecules as an alternative to inorganic semiconductors, where he suggested that large amounts of data can be stored in a tiny space such as molecules.[9]

Molecular electronics is a branch of nanoscience that investigates electrical and thermal transport properties of either single or an assembly of molecules. The first proposal of a single molecule as a diode came in the early 1970s from a theoretical study by Aviram and Ratner.[11] Since this, many techniques have been developed to experimentally investigate monolayers and single molecules such as the scanning tunnelling microscope and break junctions.[12] Molecules have a desirable characteristic whereby their electronic properties can be tuned by altering their chemical design, meaning the possibilities are infinite.[13]

Molecules, therefore, have potential in many different electronic applications includ-

ing rectification[14], switching[15, 16] and memory[17] and has also attracted the thermoelectric community. The phenomenon of thermoelectricity - the conversion of heat into electricity - was observed many decades ago.[18] This effect has been exploited in devices for thermoelectric generators and refrigerators and has gained a lot of popularity in recent years.[2] Generating over 90% of the energy used today, thermal power is ubiquitous, and despite this, it is regarded as the most wasted form of energy at ∼60% of the world energy consumption.[1, 19] The heat used to obtain electricity transformation can come as a by-product of other processes and in a sense can be regarded as renewable as it is inevitable and ubiquitous.[1]

Most commercialised TE are large bulk structures and thus are only applicable in large-scale waste heat recovery. However, theoretical calculations and experimental results of scaling down TE to nanostructures such as nanowires, quantum wells and dots suggest that size effects could enhance efficiency and figure of merits.[20, 21, 22, 23, 24] Thus, recent research has been focused on investigating molecular electronics. The first evidence of molecules displaying thermoelectric effects was discovered by Reddy et al. in 2007 and from then, the attention on molecular thermoelectrics has increased and is seen as a potential solution for the ever-growing energy crisis.

The Seebeck effect, one of the fundamental principles of thermoelectricity, was first discovered in the 1820s. This is a phenomenon where a small voltage is observed in the presence of a temperature gradient. It is intrinsically linked with the Peltier effect, which occurs when an electrical current flows through a junction, heat can either be absorbed at one end and emitted through the other or *vice versa*.[2, 1]

Although these effects are well known, the materials and devices are not extremely widespread due to the low efficiency of conversion. Presently, TE falls below other energy conversion technologies in terms of efficiency (Figure 1). High efficiencies require high temperatures and this results in heat being generated through combustion of non-renewables such as coal.

In short, experimental research into molecular thermoelectrics has its advantages. Firstly, it can provide insights into the transport properties of a junction, secondly, it can open up a door for novel approaches to assembly and formation of devices which could replace traditional silicon-based electronics and thirdly, due to the ease

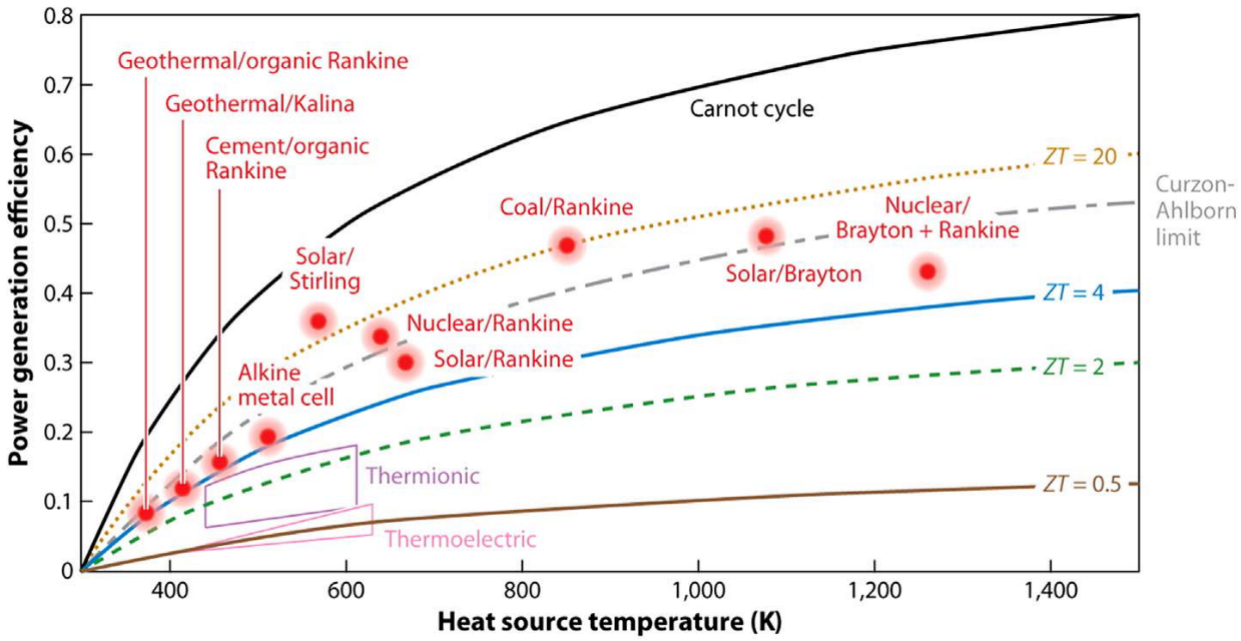

Figure 1: Comparison of energy conversion of various thermoelectrics used globally. The efficiency of the Carnot cycle curve shows the most efficient energy conversion can be depending on the temperature of the heat source. The ZT values here are assumed to be independent of temperature. Thermoelectric materials display a ZT of around 0.5 which lies far below current energy conversion devices with ZT's between 4 and 20. Figure from [1].

of bulk synthesis of readily available molecules mass manufacturing should have a low-cost.[25, 26, 27, 13]

2.2 Thermoelectric Effect

The term thermoelectric effect encompasses two parallel phenomena: the Seebeck effect and the Peltier effect. These effects arise when a circuit of two different conductors, a and b, is formed where junction a and b are both maintained at two different temperatures, leading to an unequal balance of charge between the two. Until thermal equilibrium is achieved, an electric field is induced between a and b.[28, 27] The following sections will now focus on the Seebeck effect.

2.2.1 Thermal Conductance

To begin exploring the thermoelectric effect, both the electrical and thermal transport properties need to be considered as whilst electrons conduct electricity, they

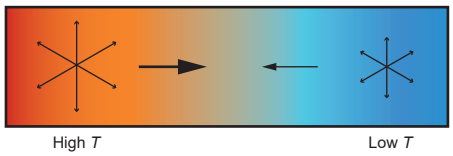

Figure 2: Simple diagram of a one-dimensional conductor showing the movement of electrons. The larger arrows indicate higher energy of the electrons due to the higher temperature.

also conduct heat. The link between thermal conductance κ and electrical conductivity σ of a material can be expressed through the ratio in the Wiedemann-Franz law $\kappa/\sigma T$ and is dependent on temperature T. This is also known as the Lorenz number.

To show this, consider a gradual temperature gradient within a metal or a semiconductor, with an external heat source and sink, assuming the gradient can be maintained and uniform across the material. At small temperature differences, the thermal conductivity κ is directly proportional to the negative of the temperature gradient $-\nabla T$, showing that the current flows in an opposite direction to the temperature gradient. This is Fourier's law and thus, thermal current density, j^q can be defined as

$$j^q = -\kappa \nabla T = -\kappa \frac{dT}{dx} \tag{2.1}$$

Consider a one-dimensional system such that electrons can only flow along the x-axis (Figure 2). At the centre of this system x, half the electrons will have arrived from the hot side and the other half from the cold. If we take the thermal energy $\epsilon(T)$ of an electron at an equilibrium temperature T, then electrons which have their last collision at a particular point $x - \upsilon\tau$, where υ equals the velocity of the electron and τ is the time constant, the thermal energy carried for each electron will be $\epsilon(T[x - \upsilon\tau])$. Therefore the contribution of electrons from the high temperature to the thermal current density j^q at point x will be the thermal energy multiplied by the number of electrons per unit volume, $n/2$, and its velocity υ. Similarly, the electrons arriving from the cold will have a velocity of $-\upsilon$ as they are moving from a positive to negative x-direction. Adding these two terms together j^q becomes:[29]

$$j^q = \frac{1}{2} n\upsilon[\epsilon(T[x - \upsilon\tau]) - \epsilon(T[x + \upsilon\tau])] \tag{2.2}$$

If the temperature over the free mean path is extremely small then the expansion of the equation around x can be

$$j^q = n\upsilon^2\tau \frac{d\epsilon}{dT}\left(-\frac{dT}{dx}\right) \tag{2.3}$$

To make this applicable for three dimensional cases, the resulting equation becomes

$$j^q = \frac{1}{3}\upsilon^2\tau c_\upsilon(-\nabla T) \tag{2.4}$$

where c_υ is the heat capacity of an electron, τ is the relaxation time and υ^2 is the mean square electronic speed. This can be arranged make κ the subject

$$\kappa = \frac{1}{3}\upsilon^2\tau c_\upsilon \tag{2.5}$$

As equation 2.5 can be complex, the formula can be independent from relaxation time τ by introducing electrical conductivity, σ and applying to ideal gas laws such as $c_\upsilon = \frac{3}{2}nk_B$ and $\frac{1}{2}m\upsilon^2 = \frac{3}{2}k_BT$, where k_B is the Boltzmann's constant, leading to the Wiedemann-Franz law:

$$\frac{\kappa}{\sigma} = \frac{3}{2}\left(\frac{k_B}{e}\right)^2 T \tag{2.6}$$

As equation 2.6 shows, in order maximise electrical current, thermal conductivity should be as small as possible. These calculations presume that electrons upon their last collision will hold a thermal energy dependent on the temperature at that time, however it should be noted that if an electron bears more energy after a collision then the velocity should also be higher. Therefore, this effect should be taken into account but in reality the end result is only effected by an order of unity.

The proportionality constant, the Lorenz number, is then

$$L_0 = \frac{\kappa}{\sigma T} = \frac{3}{2}\left(\frac{k_B}{e}\right)^2 = 2.44 \times 10^{-8} W\Omega K^{-2} \tag{2.7}$$

After a temperature gradient has been established, electrons will flow towards the colder side resulting in an electrical current. This phenomenon is the Seebeck effect.[29]

2.2.2 Seebeck Coefficient (Thermopower)

The Seebeck coefficient S or the thermopower is defined as the ratio between the thermoelectric voltage observed and the difference in temperature between two different conductors.

$$S = -\frac{\Delta V}{\Delta T} \tag{2.8}$$

or in terms of electromotive force, E_{emf}

$$E_{emf} = S\nabla T \tag{2.9}$$

And if the electrical current density can be represented as[29]

$$j = \sigma E_{emf} + T\mathbf{L}(-\nabla T) \tag{2.10}$$

where $\mathbf{L}$ equals

$$\mathbf{L} = -\frac{\pi^2}{3e} k_B^2 T \sigma' \tag{2.11}$$

and σ prime indicating the derivative with respect to energy. When negligible current is produced, $j = 0$, equation 2.10 can be substituted into 2.9 and the thermopower can be determined to be

$$S = -\frac{\pi^2}{3}\frac{k_B^2 T}{e}\frac{\sigma'(E_F)}{\sigma(E_F)} \tag{2.12}$$

Equation 2.12 is Mott's semiclassical theory for determining thermopower in bulk materials where E_F is the Fermi level.[30] Generally, electrons and phonons are major contributions to thermopower. At ambient temperatures of metals, the phonon drag is insignificant. Phonon drag happens as any temperature gradient will cause heat transport *via* phonons, the electrical current will always transfer some of its momentum to the lattice vibrations and 'drag' them as it travels.

In contrast, although similar to Mott's semiclassical formula, the Seebeck coefficient is defined in terms of transmission functions. For example, in molecular junctions, the phonon contribution becomes negligible, and therefore analysis of the Seebeck can be related to the Landauer formula S can be expressed as [31]

$$S = \frac{1}{eT} \frac{\int_{-\infty}^{\infty} (E - E_F) T(E) [\delta f(E,T)/\delta E] dE}{\int_{-\infty}^{\infty} T(E) [\delta f(E,T)/\delta E]} \tag{2.13}$$

Hence, it is evident from the above equation that to obtain significant thermopower $E \neq E_F$. Thus, at low temperatures

$$S = -\frac{\pi^2}{3} \frac{k_B^2 T}{e} \frac{T'(E_F)}{T(E_F)} \tag{2.14}$$

where T' indicates derivative with respect to energy. The final term in equation 2.14, $T'(E_F)/T(E_F)$, determines the sign of Seebeck which can be used to characterise the material as p-type (electron holes) or n-type (electrons) semiconductors. The reason for this is due to the diffusion of charge carriers towards the cold junction until compensating voltage is produced being the main contributor in the Seebeck effect. Most conductors, however, contain both hole-like and electron-like behaviours and thus, negative values of Seebeck indicate the predominant carrier in the material, where n-type materials show a negative Seebeck and positive values are p-type.

2.2.3 The Figure of Merit

The Seebeck effect can be exploited in applications such as thermoelectric generators. The efficiency of such devices can be determined with the dimensionless figure of merit, ZT. The figure of merit spurred innovation in the design and fabrication in

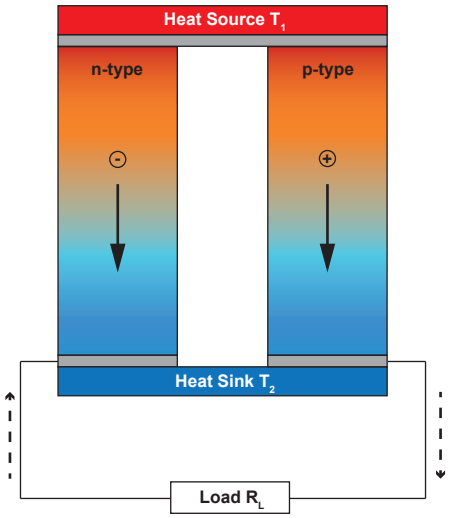

Figure 3: Diagram of a simple thermoelectric generator composed of electrically connected (grey bars) n-type and p-type semiconductors connected to a heat source T_1 and a heat sink T_2. The electrons in the n-type material and the holes in the p-type material flow towards the heat sink. The dashed line represents the direction of the current flow.

optimising thermoelectrics, by achieving a high ratio of electrical conductivity to thermal conductivity.

The most simple example to show this can be constructed using a p-type and an n-type material, for example in Figure 3 creating a thermocouple. The two conductors are connected to an resistive load, R_L.

R_L, determined by the electrical power generated from the semiconductors, directly relates to how efficient the generator is. Efficiency is the ratio of the power output compared the rate of heat leaving the source.[32] So, the current through the junction becomes:

$$I = \frac{(S_p - S_n)(T_1 - T_2)}{R_p + R_n + R_L} \tag{2.15}$$

where the total thermopower equals $(S_p - S_n)(T_1 - T_2)$. S_p and S_n are the Seebeck coefficients of each material and R_p and R_n is the resistance of the corresponding semiconductors. (T_1) and (T_2) correspond to the hot and cold temperature, respectively. Therefore the power w that reaches the load can be expressed as[18]

$$w = I^2 R_L = \left[\frac{(S_p - S_n)(T_1 - T_2)}{R_p + R_n + R_L}\right]^2 R_L \tag{2.16}$$

As the thermoelectric effect is a competitive process, the temperature gradient needs maintaining to sustain generation of the potential difference. The Peltier effect, is the opposite of the Seebeck effect and therefore will reduce the temperature gradient. Some of the heat from the source will then take part in balancing the Peltier effect, therefore total heat flow q can be described if the Peltier rate $Q_{peltier} = (S_p - S_n)/T_H$ and heat flow $Q_h = (\kappa_p + \kappa n)(T_H - T_C)$ is taken into account

$$q = \frac{(S_p - S_n)}{T_1} + (K_p + K_n)(T_1 - T_2) \tag{2.17}$$

Here, $K_{p,n}$ is the thermal conductance of the corresponding branch.

The efficiency of the system is then equal to the power divided by the total heat flow w/q. The maximum value is achieved when maximising w with respect to q, and so the ratio can be expressed as[33]

$$\frac{R_L}{R_p + R_n} = \sqrt{1 + ZT_m} \tag{2.18}$$

where Z is defined as

$$Z = \frac{(S_p - S_n)^2}{(K_p + K_n)(R_p + R_n)} = \frac{\sigma S^2}{\kappa} \tag{2.19}$$

This leads to the well known figure of merit, ZT

$$ZT = \frac{S^2 \sigma T}{\kappa} = \frac{G S^2 T}{\kappa_e + \kappa_{ph}} \tag{2.20}$$

where G is the electrical conductance. Here, it is important to note that κ can be split into two terms: κ_e and κ_{ph} arising from the thermal conductivity of the carriers and phonons, respectively.[20].

Therefore ZT is heavily dependent on the Seebeck coefficient if the material satis-

fies the Wiedemann-Franz law, in which the electrical conductance is proportional to temperature $L_0T = \kappa_e/G$, and so in molecular junctions ZT can be shown to be

$$ZT = \frac{GS^2T}{\kappa_e + \kappa_{ph}} = \frac{GS^2T}{K_e\left(1 + \frac{\kappa_{ph}}{\kappa_e}\right)} = \frac{S^2}{L_0\left(1 + \frac{\kappa_{ph}}{\kappa_e}\right)} \tag{2.21}$$

In the most ideal situation, κ_{ph} will be negligible and effects of thermal conductivity will mostly be from electrons as in the case with metals.[20]

One option is to minimise the value of the thermal conductivity of the lattice. Another option is to make the thermal conductivity of the carriers so large that the κ_l becomes insignificant.

The efficiency, η, is traditionally written as a function of ZT of the material[34]:

$$\eta = \left(\frac{T_{hot} - T_{cold}}{T_{hot}}\right)\left[\frac{\sqrt{1 + ZT_m} - 1}{\sqrt{1 + ZT_m} + \left(\frac{T_{cold}}{T_{hot}}\right)}\right] \tag{2.22}$$

The term $\dfrac{(T_h - T_c)}{T_h}$ can be expressed as the Carnot efficiency, and if thermoelectric effects were reversible η would be at the Carnot limit $\eta = T_c/\Delta T$. As a result to generate significant energy conversion a large temperature difference is necessary (Figure 1). However in thin films this would be hard to achieve unlike many of the industrial TE generators today which temperature differences can be 1000°C (for example, in Figure 1).[35]

Figure 4 shows a general trend between the efficiency of a TE device against the difference in temperature. Comparing current TE with a ZT of 3, working with 1000°C difference in temperature, the graph shows that the efficiency predicted is around ∼27%. To get the similar values of efficiency in ambient temperatures, the ZT achieved would need to reach ∼30.

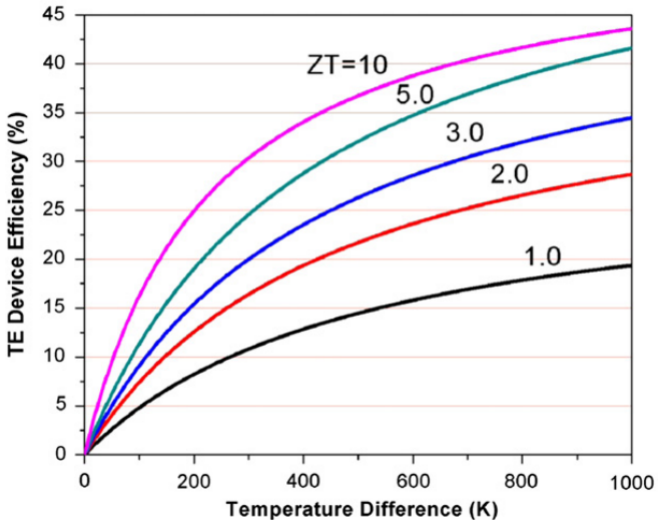

Figure 4: Efficiency of TE as a percentage with respect to the temperature difference, where $T_C = 300$ K. Shown here are examples of materials with ZT values of 1, 2, 3, 5 and 10. As the ZT of the material increases, the efficiency calculated also increases. Graph from [35].

2.3 Thermoelectricity at Different Scale Lengths

2.3.1 Bulk

The discovery of thermoelectricity has not been fully used to its advantage, as obtaining a high ZT proved challenging and slowed the rate of progress in the field. Almost 70 years after the discovery of the Seebeck effect, thermoelectrics composed of PbTe and Bi_2TE_3 were fabricated.[36]. Bi_2Te_3 is commercially available and bears a Seebeck coefficient of $\sim$230 μV/K.[37] The ZT values of bismuth and tellurium at room temperatures are both below 1.0, by alloying the two together carrier concentrations can be modified causing a decline in lattice thermal conduction. Adjusting the concentrations of the two different metals can also tune the Seebeck coefficient as desired. For example in Bi_2Te_3, Bi as the n-type and Ti as the p-type, increasing the amount of Te causes the Seebeck to drop and fall below zero becoming negative (n-type).[38]. Another benefit of alloys is that the defects between materials dramatically decreased the lattice thermal conductivity *via* phonon scattering without impairing electrical transport significantly.

Generally, bismuth-based alloys are regarded as low temperature thermoelectrics, operating at temperatures around 450 K. The intermediate range is around 850 K

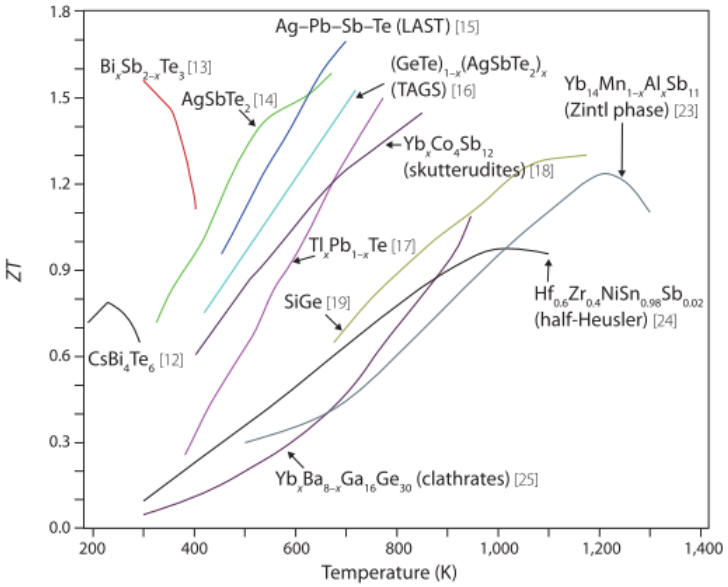

Figure 5: Figure of merit (ZT) of common bulk materials against temperature. Most of the materials shown with high performance fabricated from nanostructured engineering. Graph from [39].

and based on PbTe where the Z value is significantly lower. In high temperature working materials are fabricated from SiGe alloys are employed at temperatures up to 1300 K.

In addition to alloying, it is possible to increase ZT by purposely introducing defects into the crystal lattice. For example, doping a semiconductor brings the carrier concentration to an optimum also causing phonons to scatter - lowering the κ_l.

Typically, the average maximum ZT of TE materials made from Bi_2Te_3 or PbTe-SrTe alloys are between 1 and 2.5. In terms of efficiency, the minimum ZT value to aim for is $\sim$3 to even be compared to other similar types of technology.[1] By looking at the equation it is clear that to obtain a large ZT value is it desirable to have a low thermal conductivity whilst on the contrary, achieve large electrical conductivity.

Inorganic materials are commonly found in TE devices, however, to achieve sufficient values of energy conversion in ambient conditions, materials such as Bi_2Te_3 or PbTe-SrTe alloys do not possess a high enough ZT value. Hence, the focus in TE is now towards organic materials and they are showing promising results. As the miniaturisation of silicon-based devices reaches its limit via 'top-down' methods

(lithography), various techniques have been explored in order to continue the trend from the 'bottom-up'. By studying single molecules and manipulating the chemical structure, the properties can be tuned by exploiting the quantum interference and in turn utilising them for the fabrication of thin films. In addition to their applications to TE, the methods and results can provide the fundamental science to reconstruct devices in a different way.[40]

2.3.2 Nanoscale

It has been observed and theorised that by reducing thermoelectrics down to the nanoscale, the lattice thermal conductivity k_l decreases due to phonon scattering at each interface and surface, all whilst avoiding a high loss of electron mobility μ.[29] Therefore, nanostructured materials are highly favoured to optimise the figure of merit of thermoelectrics. One of the main challenges of nanoscale applications is that it does not always work well when applied to macro devices and the technology to do so is expensive.[41]

Another reason we expect low-dimensional devices to provide higher values of ZT is due to size-quantisation effects increasing the Seebeck coefficient.[42] This can be explained using Mott's formula. The Seebeck coefficient can be defined as

$$S = \frac{k_B}{e}\frac{1}{\sigma}\int_0^\infty \sigma(E)\left(\frac{E-E_F}{k_BT}\right)\left(\frac{\delta f(E)}{\delta E}\right)dE \tag{2.23}$$

which can be combined with a Lorentzian transmission function in equation, $T(E)$, at its most simplified form gives:

$$S = \frac{\pi^2}{3}\frac{k_B^2T}{e}\left(\frac{d(lnT(E))}{dE}\right)\Bigg|_{E=E_F} \tag{2.24}$$

Equation 2.24[29] is very similar to its counterpart for bulk materials, equation 2.23, the Landauer formula (derived in Section 2.2.2). Equation 2.24 is used to determine seebeck coefficients between molecular junctions where the transmission function is known. However, it is important to note that this approximation proves useful only when the system is at low temperatures and when the differences in $T(E)$ is minute,

away from its transition resonances.[43] This highlights the desire for steeper slopes of $lnT(E)$ close to $E = E_F$ which in turn enhances the Seebeck coefficient.

Typically, organic semiconductors have a relatively low power factor $S^2\sigma$ in comparison to their inorganic counterparts and so, the potential for organic semiconductors has not been fully explored.[44] Although this is the case, conducting polymers can have interestingly low thermal conductivities similar to inorganic and organic amorphous materials.[45] Poly(3,4-ethylenedioxythiophene) derivates (PEDOT) are a popular choice of polymer for investigation due to their environmental stability and their range in conductivities.

An example of the wide range of PEDOTs, PEDOT doped with polystyrene sulfonate (PEDOT:PSS) produces a ZT value of 1.75×10^{-3}, which lies approximately a factor of a thousand times smaller than Bi_2Te_3 alloys.[46] Bubnova et al. replaced PSS with small tosylate (TOS) anions and found an increase of the ZT value to be 0.25 at room temperature.[44] The power factor was optimised by manipulating the oxidation levels giving a Seebeck coefficient reaching 40 μVK^{-1} with an oxidation level of 36%. As the oxidation level reaches its lowest value ~15%, the Seebeck coefficient peaks at 780 μVK^{-1}.

2.3.3 Molecular Junctions

As more and more research is being done with organic thin films, understanding these devices at a molecular level is important. To do this theoretical simulations can be performed on molecular junctions to theorise the Seebeck and conductivities of films. These junctions are at the maximum level of miniaturisation where a molecule is trapped in between two bulk electrodes. To tailor molecular devices for desired properties, quantum interference (QI) effects can be exploited and therefore improve electrical and thermoelectrical abilities.

To obtain more information on electronic transport in molecular junctions, the measurement of thermopower can be used to estimate the position of the Fermi energy relative to the HOMO and LUMO. For example in Figure 6.

The transmission function of a simple two-level model where the transmission function contains two peaks[31, 47]

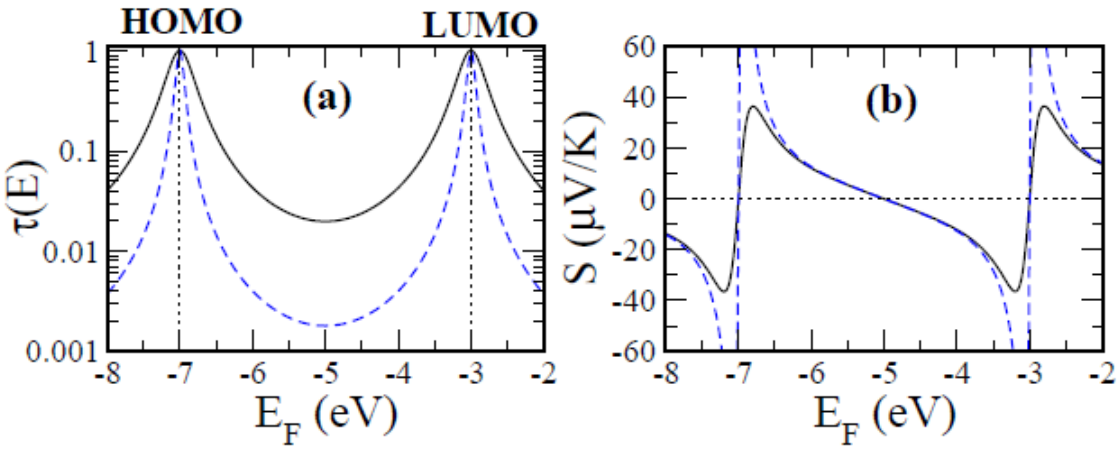

Figure 6: Transmission function computed from equation 2.25. The parameters used were υ_1 = 7 eV and υ_2 = -3 eV (black dashed lines). The Blue dashed line shows the transmission function when Γ_L and Γ_R = 100 meV. When Γ_L and Γ_R = 30 meV the $T(E)$ is represented by the solid black line. (b) The corresponding thermopower, calculated with equations 2.25 and 2.24. Graph from [31]

$$T(E) = \sum_{i=1}^{2} \frac{4\Gamma_L\Gamma_R}{(E-\upsilon_i)^2 + (\Gamma_L+\Gamma_R)^2} \tag{2.25}$$

where E_i is the energy of the two levels, $\Gamma_{L,R}$ are the broadenings of the left and the right contacts. To simplify things, the broadenings are the same for both, usually corresponding to the HOMO and LUMO of organic molecules. In situations like this, it is typical to find the Fermi energy, E_F, between the two peaks. In molecular junctions, the thermopower can either be negative or positive by whether the E_F is closer in energy to the HOMO or LUMO. If it is closer to the HOMO, thermopower is positive and related to p-type/hole-dominated transport. On the other hand, if E_F is closer to the LUMO, then thermopower will be negative and transport is dominated by electrons and considered an n-type. If the Fermi energy lies close to the middle, the thermopower can be plotted as in Figure 6. Therefore by selecting the positions of Γ and the energy levels E_i, the thermopower can be maximised.[48]

Molecules are attached to electrodes either *via* covalent bonds or intermolecular interactions and one of the most attractive properties of molecules is their low thermal conductivity. To attach molecules to a surface or an electrode, they are typically terminated with 'anchor groups' such as thiols, pyridines, amines and carbon groups

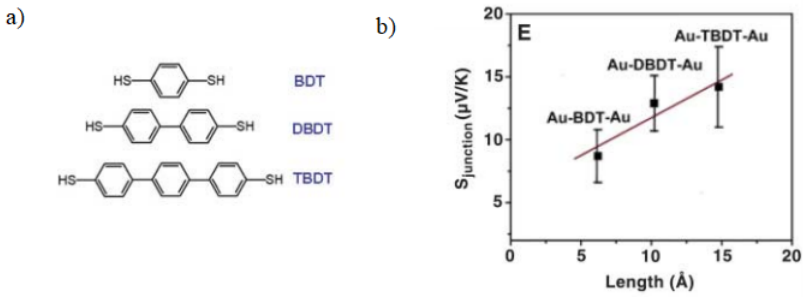

Figure 7: (a) Chemical structure of BDT, DBDT and TBDT (b) Plot of measured Seebeck coefficients

that can bind to the source and drain electrodes.[49]

The first reporting of thermopower in single molecular junctions was performed by Reddy et al in 2007[50]. By using a variation of scanning tunnel microscopy (STM) they were able to create a break junction and determined the Seebeck coefficients of 1,4-benzenedithiol (BDT) and 4,4'-dibenzenedithiol (DBDT) and 4,4"-tribenzenedithiol (TBDT) to be +8.7 $\pm$ 2.1 μ V/K, +12.9 $\pm$ 2.2 μ V/K and +14.2 $\pm$ 3.2 μ V/K. The results are shown in Figure 7.

Although the results showed a slight trend in Seebeck as a function of length in which the Seebeck coefficient increases as the length increases, this is not true for all cases. Extensive research has been done on the dependence on the length of various anchor groups. Malen et al.[51] showed that the thermopower containing phenyl rings had a linear trend with respect to length whereas molecules with an alkane backbone had the opposite effect (Figure 8).

Despite theory showing high expectations of molecular junctions, the main challenge is to experimentally show large values of ZT. Further explorations into developing different fabrication methods and potentially even advancement of measurement techniques are needed to successfully observe the thermoelectric limits of molecular junctions.

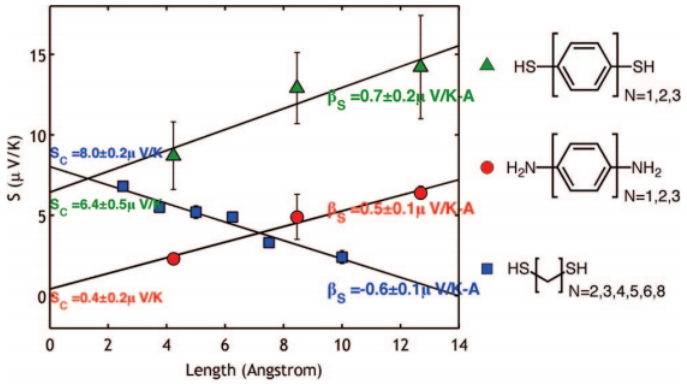

Figure 8: Plot of Seebeck coefficient as a function of molecular length. Chemical structure of the corresponding phenylenedithiols, phenylenediamines and alkanedithiols. Figure from [51]

2.4 Electronic Transport

2.4.1 Classical Transport

Electrical conduction in the macroscopic scale follows Ohm's law.[52] This shows that the current I is proportional to the voltage V and inversely proportional to its resistance R. The inverse of R can be replaced with G which describes conductance of a material. As the cross-sectional area A increases and its length L decreases the value of its conductance will also increase taking into account the conductivity, σ, which is a material property.

$$V = IR \tag{2.26}$$

$$G = \sigma \frac{A}{L} \tag{2.27}$$

Whilst Ohm's law satisfies transport in the macroscopic regime, it cannot be used to describe devices in the nanoscale. Thus, when the dimensions of a system is larger than the Fermi wavelength i.e. the de Broglie wavelength of electrons close to the Fermi level, a new approach is needed to derive the conductance for such scales.

It is important to note that junctions the size of a few nanometers or less will be in the ballistic region where the free mean path is smaller than the length of

sample.

2.4.2 Quantum Transport

As classical theory no longer correctly describes transport at the nanoscale, another theory has to be implemented. The Landauer formula is currently the most popularised approach used in nanoelectronics to describe conductance.[53] This theory assumes that if there is an insignificant effect inelastic interactions then the transport can be treated as a scattering problem.

In an experiment of a nanoscale device, the typical set up includes the sample linked to two macroscopic electrodes. The electrodes become reservoirs of electrons with specific temperature and chemical potential, μ. The scattering here would be elastic until the electrons reach the electrodes and the phase coherence is preserved throughout the sample. This approach can then be used to show the relationship of a sample between its electronic transport properties and its transmission as well as its probability of reflection as it travels from one electrode to the other.

Firstly, let us consider a one-dimensional set-up, for example in Figure 9(a) where the sample is contacted by macroscopic electrodes on either side. The potential barrier of this system is depicted in Figure 9(b). If we then take an electron as a plane wave, e^{ikx}, (where k is a continuous variable of the wave number or wave vector), travelling from the left side, I, of the barrier, the probability of the partially reflected wave will have an amplitude of r, and the probability of the partially transmitted wave at III will have an amplitude of t, the probability that an electron will be transmitted will be $T(k) = |t|^2$.[31] From this, the electrical current density of this electron J_k can be described by the expression

$$J_k = \frac{\hbar}{2mi}\left[\psi^*(x)\frac{d\psi}{dx} - \psi(x)\frac{d\psi^*}{dx}\right] = \frac{e}{L}\upsilon(k)T(k) \tag{2.28}$$

where L is the length of material, e is the electronic charge and $\upsilon(k) = \frac{\hbar k}{m}$ represents the group velocity of electrons. $\hbar$ is the reduced Plancks constant, and mi is the effective mass of the electron in the linear chain. $\psi(x)$ denotes the wave function $\psi^*(x)$ is the complex conjugation of the wave function. Full derivation of this equa-

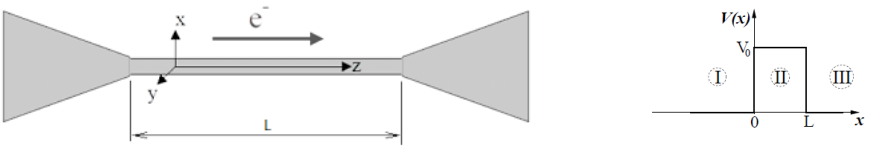

(a) (b)

Figure 9: (a) Visual representation of quantum transport in the one-dimensional set-up and (b) rectangular potential barrier. [31]

tion can be found in Kittel, Solid State Physics, however for the purpose of this work, full derivation has not been noted.[**Kittel1976**]

As the system doesn't take into account effects from inelastic scattering, the current is preserved no matter where it is evaluated.

In any sort of solid state device, the current produced is from a sum of more than one electron, k, and therefore needs to be taken into account. Furthermore, due to the Pauli exclusion principle another factor has to be considered: $f_L(k)[1 - f_R(k)]$, where f_L and f_R are the Fermi-Dirac distributions of the left and right electrodes. This term effectively includes only the filled states from the left L electrode and empty states in the right R electrode in the current calculation.

$$J_{L\to R} = \frac{e}{L}\sum_k \upsilon(k)T(k)f_L(k)[1 - f_R(k)] \tag{2.29}$$

With equation 2.29, the summation can be converted into an integral if $\frac{1}{L}\sum_k \upsilon(k) = \frac{1}{2\pi}\int \upsilon(k)dk$ resulting in

$$J_{L\to R} = \frac{e}{2\pi}\int \upsilon(k)T(k)f_L(k)[1 - f_R(k)] \tag{2.30}$$

By introducing the density of states and converting variable k into energy E, the current can now be determined as

$$J_{L\to R} = \frac{e}{h}\int dET(E)f_L(E)[1 - f_R(E)] \tag{2.31}$$

and *vice versa* from right reservoir to left

$$J_{R\to L} = \frac{e}{h}\int dET(E)f_R(E)[1 - f_L(E)] \tag{2.32}$$

where h is Planck's constant $T(E)$ represents the transmission function of electrons passing through the molecule from one electrode to the other. The total net current can therefore be expressed as what is known as the Landauer formula[40]:

$$I = \left(\frac{2e}{h}\right)\int_{\infty}^{-\infty} dET(E)[f_L - f_R] \tag{2.33}$$

The factor of 2 has been added to due to spin degeneration.

$$f_{\text{left/right}} = \left[e^{(E-E_{\text{F}}{}^{\text{left/right}})/k_BT} + 1\right]^{-1} \tag{2.34}$$

where E_F in the Fermi energy or can also be denoted as μ which represents the chemical potential.

From equation 2.33, it is apparent that the net current depends on the difference between the two distributions. At zero temperature $E_F{}^{\text{left}}$ and $E_F{}^{\text{right}}$ can be defined as $E_F{}^{\text{left}} = E_F + \frac{eV}{2}$ and $E_F{}^{\text{right}} = E_F - \frac{eV}{2}$. By averaging T(E) around the Fermi energy with a width equal to eV, the Landauer formula can be simplified to give the electrical conductance when the bias voltage is low[54]

$$G = \frac{I}{V} = G_0T(E_F) = \left(\frac{2e^2}{h}\right)T(E_F) \tag{2.35}$$

The term $\frac{2e^2}{h}$ is also known as the quantum of conductance and can be denoted as G_0.

$$G_0 = \frac{2e^2}{h} = 77.48\mu S \tag{2.36}$$

This is a fundamental value in quantum nanostructures as the conductance becomes independent from the length and quantised, characterising the ballistic regime.

Despite the scattering approach being widely accepted and used, it comes with some

limitations. The formalism does not calculate actual transmission of an atomic contact or molecular junction, however predictions can be made using various other combined techniques such as random matrix theory. The second disadvantage to the Landauer formula is that it is assumed that inelastic scattering can be ignored. A method of overcoming this involves more advanced theories, for example, Green's function. [31]

Quantum transport in molecular junctions

The energy levels of a molecule come from its molecular orbitals and are discrete, unlike bulk materials where the energy bands are continuous. The HOMO of a molecular junction is analogous to a semiconductor's valence band whereas the lowest unoccupied molecular orbital (LUMO) is representative of the lower level of a conduction band.[54] Electrons begin to fill the band with the lowest energy up and to the HOMO. The HOMO or the LUMO govern the charge transport of a molecule depending on which orbital lies closer to the fermi energy of the electrode. These discrete energy levels become a continuous band similar to bulk materials when the molecule is connected to two leads on either end.

Quantum interference (QI) in closed systems i.e. isolated molecules, is not the same as QI in open systems whereby the molecules are connected to electrodes. In a closed system, only constructive QI creates molecular orbitals and a finite energy spectrum whereas in an open system, the electrons form an infinite energy spectrum as they flow through the molecule, in other words, the energy states become similar to those of bulk materials. Here, it is significant to know what the transmission coefficient $T(E)$ of the molecule is.[40] The transmission coefficient can be both constructive and destructive, representing the probability of the de Broglie waves of energy entering the molecule. If a molecule has atomic orbitals which emit de Broglie waves at a certain position i the amplitude of the wave at a different atomic orbital in the molecule, j will either be at an antinode or a node. If at position j it coincides with an antinode of the de Broglie wave, then it is said to be constructive interference. If, however, position j is where a node is found then destructive interference occurs. If destructive interference happens in a molecule then the transmission coefficient $T(E)$ will disappear. If at position j it coincides with an antinode of the de Broglie wave,

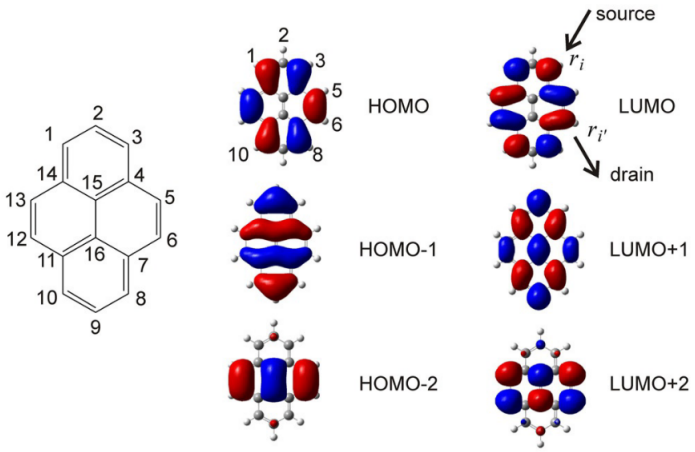

Figure 10: A diagram representing the HOMO (left) and LUMO (right) of pyrene. Regions with positive amplitude and shown in red and regions with negative amplitude is in blue. Both HOMO and LUMO show areas of high amplitudes on, for example, atoms r_5 and r_8 and low amplitude on atoms r_2. HOMO-1 represents the energy level 1 below the HOMO and LUMO+1 is the energy band corresponding to the energy level 1 above the LUMO (2 corresponds to the 2 levels).[49]

then it is said to be constructive interference. If, however, position j is where a node is found then destructive interference occurs. If destructive interference happens in a molecule then the transmission coefficient $T(E)$ will disappear.

When working with single molecules it is important to understand some basics of quantum interference. When an aromatic molecule is weakly coupled to its electrodes, for example, a pyrene molecule containing acetylene anchor groups, the QI properties of the molecule remain present. On the other hand, if the molecule is strongly coupled to the electrodes without the presence of anchor groups, the characteristics are lost and calculating the transmission coefficient becomes much more complex.[49] By preserving the identity of the molecule, it is possible to use its molecular orbitals to predict its electrical conductance and transport properties.

As an example, in a closed system (Figure 10), we imagine a weakly coupled pyrene molecule to only contain one MO denoted as $\psi^H(r)$, then the electrical conductance $\sigma_{ii\prime}$ will be proportional to these orbitals multiplied together, $\psi^H(r_i)\psi^H(r_{i\prime\prime})$ if the current enters at position r_i and leaves at $r_{i\prime\prime}$. Thus, the connectivity of anchor groups should be attached to the atoms with amplitudes of significant sizes to generate a large conductance. In the case of pyrene, to obtain high electrical conductance, the anchor groups could potentially be attached to atoms r_5 and r_8. If the

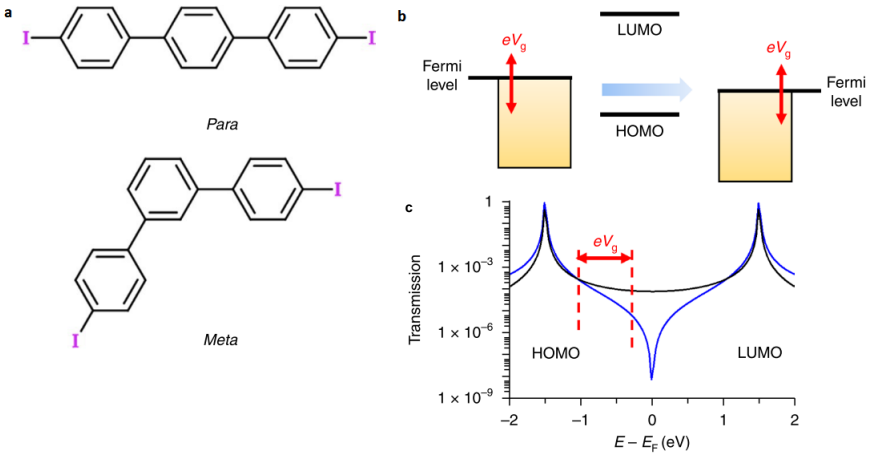

Figure 11: (a) Chemical structure of para and meta-oriented diphenyl benzene, where I represents the points connected to external leads. (b) Fermi energy levels moving relative to HOMO/LUMO before and after applying a gate voltage eV_g and c) transmission function of molecular energy levels and Fermi level, where constructive interference in shown in black and destructive interference is in blue. Image from [58].

current enters through r_2 via the anchor group and exits at r_9 then the conductance produced will be fairly low.

Breit-Wigner[55], Fano[56] and Mach-Zehnder[57] are three types of resonances that are significant in single molecules arising from QI.[40] In short, Breit-Wigner resonance occurs when the backbone of a molecule resonates with the energy of an electron passing from one end of the molecule to the other and can be destructive or constructive; Fano resonance is an example of destructive interference where the energy of an electron traversing the molecule interferes with the energy on a pendant; and Mach-Zehnder resonance occurs when partial de Broglie Waves of energy travel different paths along the backbone of a molecule and interfere constructively.[40]

QI can alter the conductance of a molecule by affecting the transmission function. As an example, if diphenyl benzene is being studied using STM as a single molecule, when applying a bias voltage, the Fermi levels of the tip and the electrode move in proportion to the HOMO and the LUMO of the molecule (Figure 11).[58] Figure 11(c) shows the position of the molecular energy level after the shift, where the blue represents meta-orientated diphenyl benzene and black corresponds to para-orientated diphenyl benzene. Meta shows a clear anti-resonance between the

HOMO-LUMO gap where the transmission drops as $E - E_F$ becomes zero. The para-orientated molecule displays no anti-resonance; therefore, the transmission is less dependent on energy. By determining the type of QI occurring within the molecule, insights into the transmission function can be obtained.

2.5 Principles of Molecular Design

As mentioned in the previous section, the objective of thermoelectric materials is to produce highly electrically conductive molecules, enough to limit the thermal consequences of phonic transport. As such, extensive research has been done to discover the theory behind which designs are most suitable for this.

Length

Molecular wires (molecular chains which are capable of conducting electric current) fall into two distinctions: saturated and conjugated. With large HOMO-LUMO gaps, saturated compounds tend to be fairly poor at conduction.[59] Experiments have shown as the length of the wire increases the conductance G decreases exponentially (Figure 12) and can be expressed as:

$$G = Aexp(-\beta L) \tag{2.37}$$

where A is a constant, β is the factor of decay, representing the efficiency of electron transport and L is the length.[60] This has also been the case for peptide chains.[61]

Although this is the general trend of saturated wires, it can be difficult to compare results due to the complexity of the measurements. Experimentation is done either with a singular molecular junction or typically with a molecular layer, however even with single molecular experiments, molecule-electrode contact is not always the same producing two or more conductances per molecule.[62]

Much research has been carried out on the impact on conductance by varying molecular lengths showing the conductance decreasing as length increases.[63, 64, 65, 59, 66] As briefly mentioned in the previous section, the effect on thermoelectricity

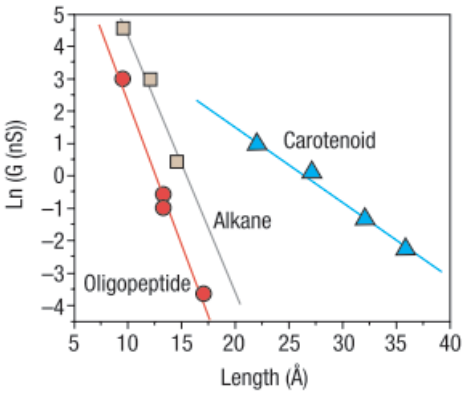

Figure 12: Conductance G of saturated (oligopeptide and alkane) and conjugated (carotenoid) molecules with varying lengths between 10-40 . Each system shows the conductance decreasing exponentially as the length increases with a change in the gradient.[59]

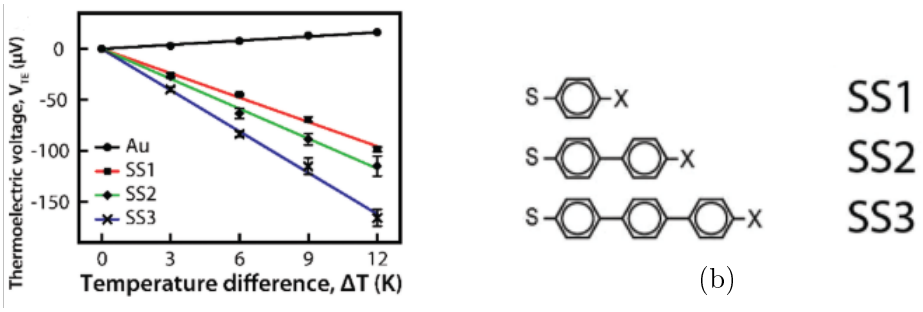

(a) (b)

Figure 13: (a) Measured thermoelectric voltages for corresponding molecules and (b) chemical structures of examined molecules where X represents sulphur. Measurements and graphs carried out by Tan et al. shows that as additional phenyl rings are added to the molecular structure the thermopower increases.[67]

changes depending on the delocalisation within the chain. Tan et al. have experimentally and theoretically shown with increasing π-systems within the chain, the Seebeck coefficient increases.[67] Where some of their key results are shown in Figure 13. However, alkane chains display a decrease in the Seebeck coefficient as chain length increases, much like its conductance. π-systems appear to have no effect on the trend of conductance. They will show a decreasing trend.[68, 69]

Quantum Interference

This section will now focus on the importance of quantum interference on conductance and thermopower in single molecular junctions. Compared to saturated hydrocarbons, conjugated molecules have delocalised π-systems with a smaller HOMO-

LUMO gap and theoretically should be more efficient at charge transport. Where the main transport mechanism in saturated molecules is thought to be tunnelling, in conjugated molecules charge is transported via hopping.[59] Hopping mechanism offers an advantage over tunnelling as it is less dependent on the molecular length and also occurs when molecule length exceeds ∼4 nm.[70]

Another common method of manipulating charge transport asides from varying molecular lengths is to manipulate QI within molecules containing multiple pathways. In the simplest term, ring structures contain two branches and therefore if electron waves propagate through either side, they can interfere constructively resulting in enhanced conductance or destructively, minimising its conductance. Because of the ability to modify molecular orbitals by manipulating chemical structure, it should be possible to adjust conductance. Theoretically, a molecule with two conduction pathways should show higher conductance when compared with a similar molecule with only one pathway - similar to having parallel resistors. Unlike two resistors in parallel, the constructive interference could increase four times as much or even more.[71] This occurs for molecules in an open system where either side of the molecule is connected to macroscopic leads. In situations where the system is closed and the molecule is isolated, constructive QI forms molecular orbitals and a discrete energy spectrum can be found by solving the Schrodinger equation. Colin Lambert's review in 2015 goes into more depth about this derivation.[40]

Now considering open systems, it is important to note that there are two different types of conjugation, linear conjugation and cross conjugation. Cross conjugation can be defined as a molecule containing three π-bonds and only two are able to interact with each other, as opposed to linear conjugation where all double bonds can interact, these two types are illustrated in Figure 14.

By looking at the type of conjugation, the type of interference can then be determined which will affect its electrical properties. Guedon et al. showed this experimentally with molecules from Figure 14.[72] They discovered the conductance difference between AQ-DT and AC-DT were almost two orders of magnitude apart, AC-DT being of higher conductance. This can be explained through density functional theory (DFT), the calculations on the transmission functions in the molecular

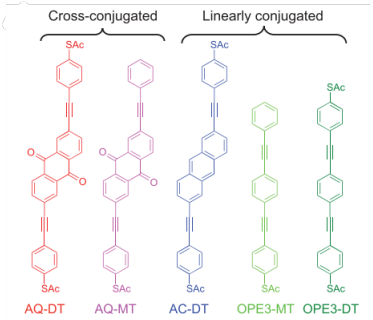

Figure 14: Chemical structures of cross conjugated and linearly conjugated molecules studied by Guedon et al.[72]

junctions leading to expectations of its conductance through the Landauer formula. Three molecules were run: AQ-DT, AQ-MT and AC-DT. AQ-DT and AQ-MT (cross conjugated) exhibited a large trough between the HOMO and LUMO levels as seen in Figure 15. This dip is known as 'anti-resonance' or the result of 'destructive' interference and the peaks, a typical feature of molecular junctions is the orbital energies where resonance tunnelling occurs.[73] This has been supported by Solomon et al.'s research from 2008.[74, 75]

By altering the type of connections on a ring, for instance, putting chains in the ortho, para or meta position, we can now predict the QI.

Phonon-suppressing

Although manipulating chemical structures of open systems can contribute to high conductances, when considering thermoelectricity and figure of merits, suppressing a molecule's phonon transport becomes very important. Bürkle et al. presented a theoretical study on [2,2]paracyclophane derivates to show that high phononic contribution severely suppresses ZT.[76, 77] Supporting this, Sadeghi et al. studied transport properties of oligoyne and alkanes and found as the length of oligoynes increase, the thermal conductance decreases whereas the opposite is observed when increasing alkane length.[78] Phononic transport calculations are shown in Figure 16.

Losego et al. investigated interfacial thermal conductances using molecules with varying covalent characteristics which showed that as the covalent character increases the thermal conductance also increases compared to structures with more

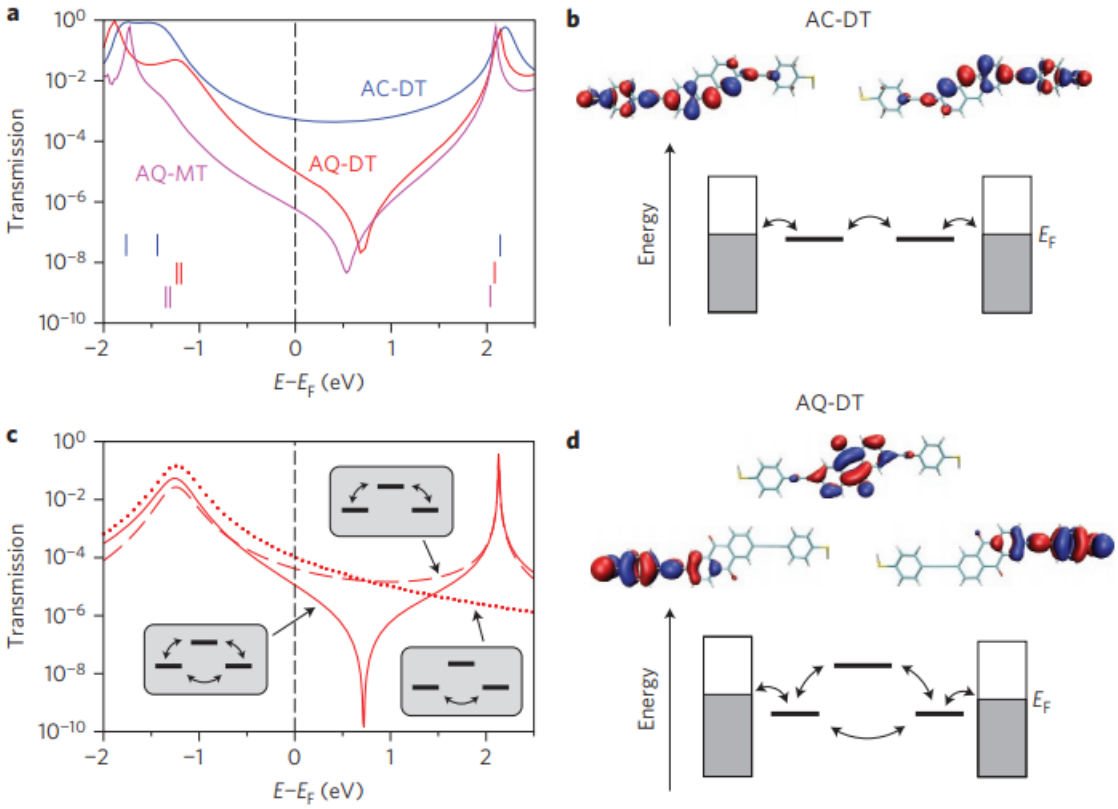

Figure 15: (a) Transmission function of AC-DT, AQ-DT and AQ-MT, where molecule AC-DT is linearly conjugated, and AQ-DT and AQ-MT are cross-conjugated. Vertical bars represent HOMO and LUMO. (b), (d) Molecular orbitals of AC-DT and AQ-DT respectively. (c) Transmission function showing the two pathways possible for AQ-DT and its added transmission probability.[72]

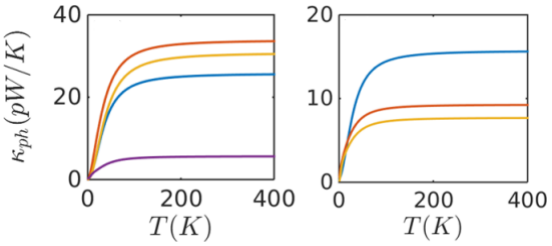

Figure 16: Phononic transport of alkanes (left) and oligoynes (right) where the different colour lines represent the length. Blue - N=1, orange - N=2, yellow - N=4, purple - N=8. Figure from [78].

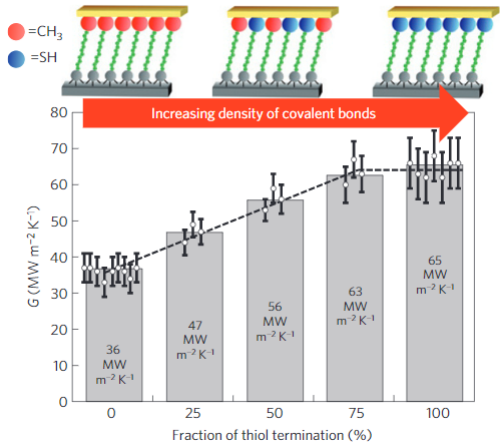

Figure 17: Thermal conductance of increasing covalent bonds in self-assembled structures. Covalent character was increased in these systems by increasing the methyl:thiol anchor group ratios, which in turn increased the conductance.[79]

van der Waals (vdW) features, represented by Figure 17.[79]

These findings combined allowed further experimentation by Li et al. into optimising methods in suppressing phonon transport.[80] They found by stacking π-systems, the thermal conductance drops around 95% compared to a covalently bonded molecular junction.[81] Their findings are presented in Figure 18. With a single molecule, it can be seen that the phonon conductance from longitudinal mode (x) and out-of-plane (z) direction contribute much more than in the y plane (in-plane longitudinal mode). When introducing π-stacks the thermal transport becomes dominated by the z channel and for the PA system, contributions from x and y are almost zero. However when comparing the junctions with each other, the thermal conductances for C1 drop from $\sim$150 pW/K to $\sim$6 pW/K for CC11 and CC13.

Anchor Groups

One method of trying to achieve the correct and consistent contacts when performing measurements is the use of anchor groups. Switching out anchor groups in preference for others can alter the energy positions of the HOMO and LUMO of the molecule with respect to the E_F of the electrode due to its donor or acceptor characteristics.[82]

Contact points between the molecule and electrode affect the charge transport properties of the junction largely attributed to their different coupling strengths. Most

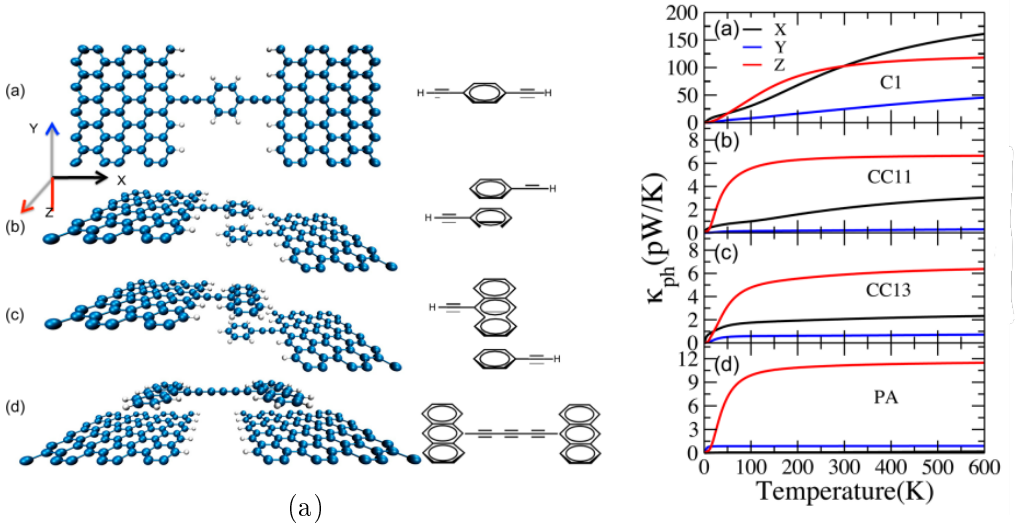

(a) (b)

Figure 18: (a) Chemical structures of the molecular junctions studied. (b) Corresponding phononic thermal conductance of each junction in the same order. Findings from Li et al.[80]

commonly found anchor groups include amino (-NH_2), pyridyl (-PY) and thiol (-SH), just to name a few. The first and most extensively researched anchor group to Au is thiol as it binds to gold extremely well forming strong covalent Au-S bonds.[83, 84, 85, 86, 67, 50] Although nitrogen-terminated groups bind to gold weakly in comparison there is also a number of experimentation and research on it.[84, 87, 88, 12]

Chen et al. investigated aliphatic molecular wires with three different terminal groups -COOH, -SH and -NH_2, the results showed that the thiol terminated group exhibited the largest conductance, followed by amine then carboxylic acid (shown in Figure 19).[88] They also determined that the prefactor constant A, a representation of contact resistance, relies upon the anchoring group whereas the decay constant is less dependent on anchoring groups.[88] These findings are also in line with experimentation carried out by Hong et al. who studied the molecular conductance of Tolanes.[84] The contact resistance appears to be related to the binding energy of gold and contact atom, for example, Au-S (-SH) has a bond strength of ∼1.73 eV, Au-N (NH_2) ∼0.35 eV and for Au-O (-COOH) ∼0.087 eV. Au-O ranks lowest as the binding nature of Au-O is thought to be from ionic and coordination interactions.[89, 85] Therefore, molecules with COOH anchor groups shows the lowest conductance values.

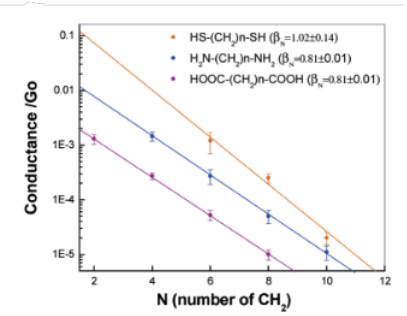

Figure 19: Logarithmic plots of singular molecule conductance decreasing as the length increases. Orange dataset shows molecules with sulphur anchor groups with the highest G_0 value, following this pyridyl anchors (blue) and COOH anchors at the lowest.[35]

Deciding on the anchor groups for desired conductance is important as we have seen, therefore it makes sense the anchor group will also affect its thermoelectric properties. Widawsky et al. experimented with pyridyl- and amine-terminated molecules.[90] Through their experimental findings, they deduced that amine anchors show a positive Seebeck whereas, pyridine anchors show a negative Seebeck coefficient. Using DFT modelling, the reason for the opposing Seebeck signs comes from where the transmission functions lie in relation to the fermi level E_F. Additionally, found that when the Seebeck was negative (pyridyl groups) the transmission function originates from a LUMO-derived peak (Figure 20).

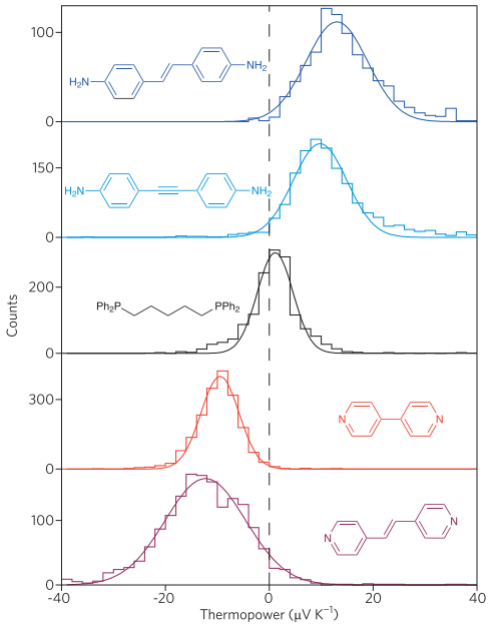

Figure 20: Histograms of Seebeck coefficients of all molecules experimented with by Widawsky et al. with Gaussian fit. The molecules with amine anchor groups show a positive thermopower (hole-dominated transport) whilst molecules with pyridyl anchor groups display a negative thermopower (electron-dominated transport).[91, 90]

Chapter 3

Molecular Assembly

3.1 Molecular Forces

The interaction between anchor groups and surfaces is very important as they control the attraction of the molecules to the substrate. Although not all molecules will contain specific functional groups the main forces which hold them together are described below.

3.1.1 Intramolecular Forces

Covalent bonding

Covalent bonding occurs when one or more valence electrons of atoms are shared between the positively charged nuclei. Figure 21 shows the formation of a covalent bond in a hydrogen molecule. The electrons would be equally shared between the two hydrogen atoms, where the majority of their time is spent between the two. Depending on the electronegativity of the atoms, the sharing does not have to be equal (electrons will orbit the more electronegative counterpart). The result of this bond formation is a molecule. Covalent bonds formed will complete an atom's subshell and combined, the potential energy will see a decrease as the formation of a bond is more stable and in turn, energetically favourable.

Atoms are able to form covalent bonds depending on the number of valence electrons they have and are typically short-range forces ~0.1-0.2 nm.[92] One of the important

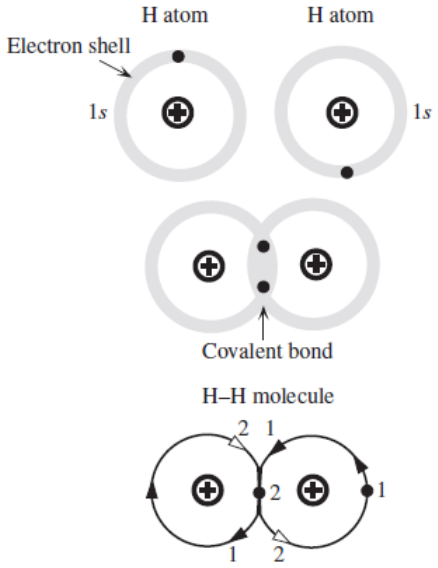

Figure 21: Visual representation of how valence electrons would orbit a H_2 molecule. Diagram from [93]

characteristics of a covalent bond is its rotational freedom around a single bond. Double bonds have less rotation and flexibility whereas triple bonds are even more restrictive.

Covalent bonds are directional and have defined orientations in space relative to each other. This is because in order to create a covalent bond, there must be an overlap of atomic orbitals and this can only happen in certain arrangements. Therefore in multivalent structures, the bonds will arrange themselves into a 3D lattice/structure.

This is fundamental for forming self-assembled monolayers with anchor groups that are capable of chemisorbing to a substrate. Attaching monomers onto the surface could in turn lead to selective polymerisation with 3D directionality.

3.1.2 Intermolecular Forces

Van der Waals

Van der Waals (VdW) forces are unlike intramolecular bonds (covalent, ionic and metallic), they are the attractive and repulsive effects between molecules and atoms including neutral atoms and are relatively weak compared to intramolecular forces. These forces can range from 10 nm to 0.2 nm.[92] The attractive force is more

commonly referred to as dispersion forces or London dispersion forces. Dispersion forces are the major contributor to VdW forces.

Evidently, with polarised atoms the dipole generated is clear. However, in the case of neutral atoms, dispersion forces arise when an instantaneous dipole moment is established due to the constant movement of electrons around the nucleus, creating an electric field. This in turn polarises neighbouring non-polar atoms causing an attractive force between the two.

The overall potential energy of two neutral atoms and their attractive and repulsion forces can be illustrated in Figure 22. This approximation is widely known as the Lennard-Jones potential or 6-12 potential and can be expressed mathematically as:

$$E(r) = 4\epsilon \left[\left(\frac{\sigma}{r}\right)^{12} - \left(\frac{\sigma}{r}\right)^{6} \right] = \frac{A}{r^{12}} - \frac{B}{r^{6}} \tag{3.1}$$

where r is the distance between the centre of two atoms, σ is the distance where $E(r) = 0$ and ϵ is the potential well depth and also indicates the strength of the attraction. A and B are $4\epsilon\sigma^{12}$ and $4\epsilon\sigma^{6}$, respectively.

At large distances, the particles are not close enough to feel the effect. As the distance between them decreases the attractive force r^6, draws them together, increasing the potential well. Due to the Pauli exclusion principle, at point r_0 the particles will experience repulsive forces r^{12}.

Van der Waal forces are important for UHV assembly where the main interaction between the surface and the molecule will typically be physisorbed.

Metal coordination

A coordination bond is a similar concept to covalent bonds however rather than sharing electrons to satisfy their subshell, the covalent bond is formed through a donation of a lone pair of electrons from one atom to an empty orbital of another.[94] The centre of a coordination compound is typically a metal atom and can accept between two to six electron pairs. The electron-donors are atoms or molecules called ligands.

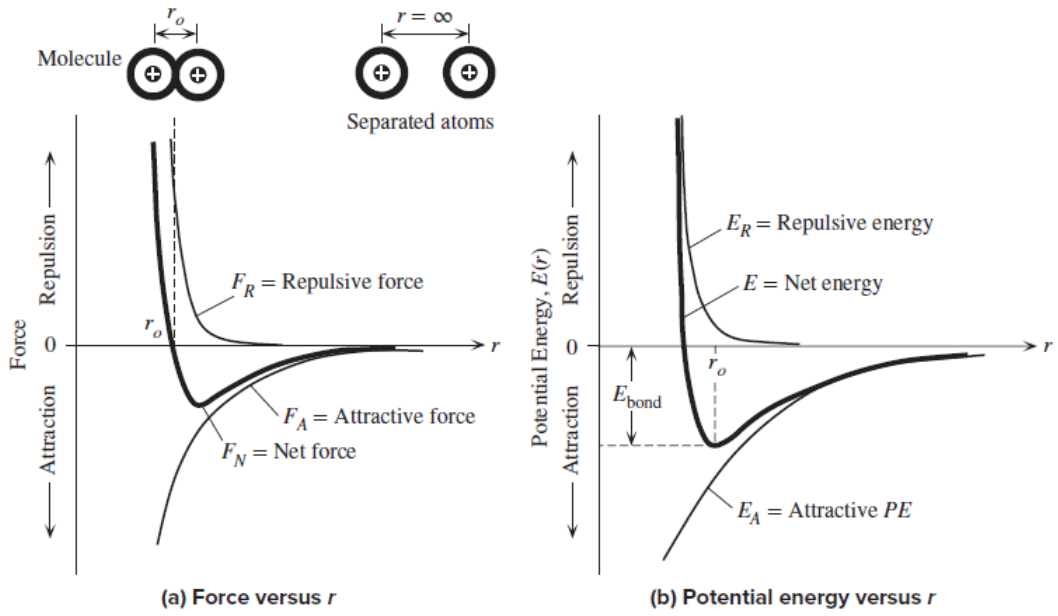

Figure 22: (a) Force vs internuclear distance. (b) Potential energy vs internuclear distance. r_0 is the equilibrium separation also known is the bond length. When both atoms are far apart, the attractive force dominates and as the distance decreases, the atoms experience stronger repulsive forces. Image from [93].

First proposed by Alfred Werner, metal ions are thought to have two valencies: primary and secondary. Primary valency refers to the oxidation state of the metal ion and secondary corresponds to the coordination number.[95] According to his theory, secondary valencies occupy certain positions around the metal atom where repulsion between each ligand is at its lowest. Simple models of the geometry of two to six ligand coordination complexes are shown in Figure 23. Although depending on the size and species of the ligand the predicted shapes may not be accurate, for example, four-coordination complexes are predicted to hold a tetrahedral shape. However, it is also possible to form a square planar complex where all ligands are found in the same plane. The most commonly found coordination numbers are four and six.

Coordination networks formed from coordination complexes have been extensively studied and are capable of creating pores with tuned size and shape as well as altering chemical properties. Also known as metal-organic frameworks (MOFs).

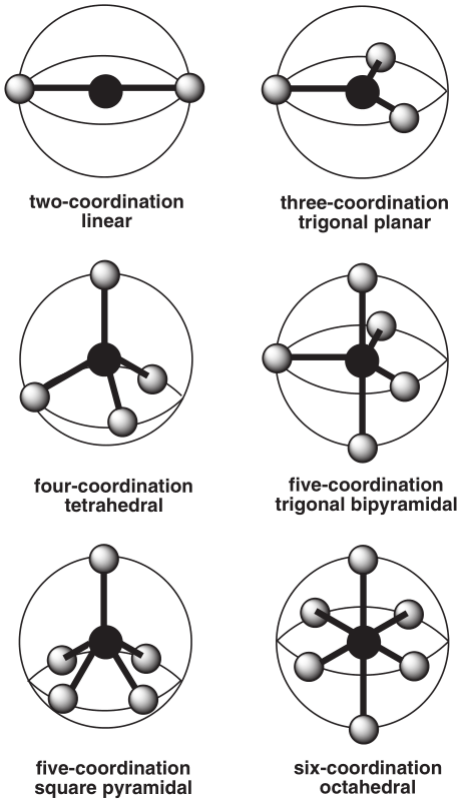

Figure 23: Shapes of complexes with increasing number of ligands.[94]

3.2 Self-Assembly

The process of solution self-assembly typically involves adsorbing molecules onto the surfaces of metals as this will lower the free energy of the interface.[96] The interaction between molecules and the surface can alter the interfacial properties of the metal or metal oxide. For example, it may decrease the reactivity of the surface atoms.[97]

As mentioned in previous chapters, molecules are an attractive alternative to bulk materials with regard to their unique functional properties. The technology industry faces challenges due to Moore's law, as previously mentioned. The limitations of continuing this trend can be due to both physical constraints from conventional miniaturisation methods such as lithography and the need for more research into the transport mechanisms which govern these processes. Typical methods for reproducing devices with specific surface topology can be grouped into two main approaches: 'bottom-up' or 'top-down' (Figure 24)[98].

As the name suggests 'top-down' methods involve patterning a particular substrate

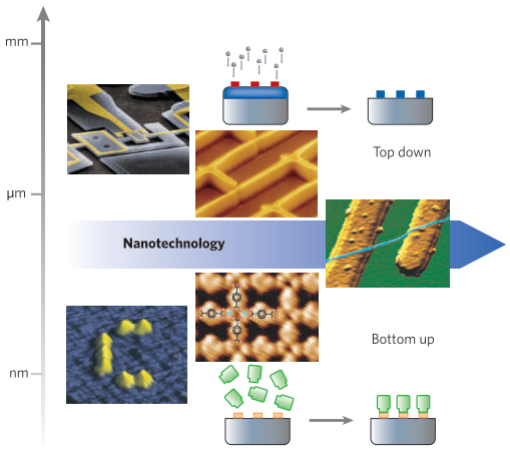

Figure 24: The larger the scale the more 'top-down' methods are used e.g. electron-beam lithography, microcontact printing (from left to right). At the smaller scale, 'bottom-up' approaches are possible, shown are two electrodes connected by a carbon nanotube, metal-organic nanoporous network of iron atoms and carbon monoxide molecules arranged using a scanning tunnelling microscope (middle right to bottom left). Image from [98].

or creating a structure on a substrate. Such methods include lithography, writing or stamping. Alternatively, the intention of forming nanostructures from the 'bottom-up' allows for guidance and ordering of the assembly of the structures straight from the atoms and molecules at the nm scale.

Molecular electronics relies upon a 'bottom-up' approach where molecules assemble in their most natural way to form the foundations for building more complex structures. Despite research into molecular electronics being around for many decades, it is unlikely to replace its silicon-based counterparts in the near future. Part of the challenge is finding a way of stabilising the molecules on the substrate without interfering with the electrical functionalities.[99] Although this is the case, the research done can provide novel functionalities to further the advancement of such devices. By observing molecular junctions, the knowledge can then be transferred and scaled up into devices for easier application.[31]

3.2.1 Solution Self-Assembled Monolayers (SAMs)

Self-assembly is a simple way to form thin film molecular systems where the properties can be investigated and altered to suit one's desires. Self-assembled monolayers (SAMs) can be prepared with ease, typically not requiring any specialist equipment.

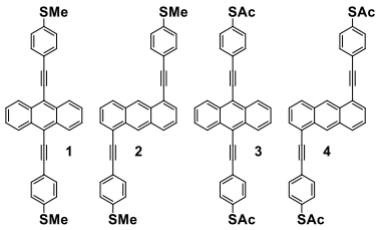

Figure 25: Chemical structures of anthracenes investigated by Wang et al. for quantum interference.[104]

By submersing a substrate into a solution of an adsorbate, a uniform layer can be chemisorbed onto the surface.

The molecules or ligands used in SAMs formation typically have an anchor group or any chemical functional group, with an affinity for a surface. In some cases, the head group can have a high affinity for the surface and will in turn replace adsorbed molecules on the surface. There are many organic materials with different binding energies to different metal surfaces. The first and the most widely studied class of SAMs is the adsorption of thiols to gold because of its highly stable Au-S bond.[100, 101, 102, 103]

A recent study done by Wang et al. presented theoretical predictions of conductance on four single anthracene junctions each with different connections to the electrodes (Figure 25).[104] The authors showed that by scaling the molecular junctions into SAMs, the conductance, experimentally, was in agreement with its calculations.

When considering the kinetics of self-assembly, the coverage can be compared to the Langmuir or Avrami kinetic model.[105] Peterlinz and Georgiadis used surface plasmon resonance (SPR) to investigate the kinetics of a series of alkanethiol molecules on a gold surface in ethanol.[106] They found that the SAMs formation could be described by a sequence of distinct kinetic steps. Assuming that the rate of deposition is proportional to the amount of space available on the substrate, the initial adsorption step (within the first 25 minutes) can be described by two different models: a diffusion-limited first-order Langmuir model and a second-order non-diffusion limited model – which both show that as the mass of the molecule increases the rate constants decrease.[107, 108, 109] As deposition time increases to 30-60 mins, the deposition rate follows a zeroth-order model opposite to the first step; as the mass

increases, the thickness of the SAMs is found to increase monotonically.

Solution self-assembly as established in this section is a suitable method to form monolayers and although these layers are well-ordered they are not pristine. In the formation of these SAMs, different types of defects can be introduced whether from the solvent or from oxidation.[110, 97, 111]

3.2.2 Ultra-high Vacuum (UHV) Self-Assembly

SAMs can also be formed in the gas phase. This is usually carried out in an UHV environment, which allows for the surface of the substrate to be cleaner than with solution SA.[112]

The deposition of molecules in UHV is highly ordered and formed by surface diffusion. For molecules with anchor groups that attach to gold, for example, thiol end groups, initially, there is a physisorption step through van der Waals forces. Once the molecules interact with the surface a strong covalent bond forms between the sulphur headgroup and the gold surface. In addition to adsorbates forming covalent bonds with the surface, they can also form covalent bonds with each other.[110] Figure 26 shows the interactions that can occur between molecules on a surface. They can interact with the surface directly (Figure 26(a, b)) with a charged adsorbate (blue circle) or if the adsorbate creates a dipole moment to the surface, contributing to its surface distribution.[113] A similar situation will happen with organic materials, particularly with polar groups, which interact with other organic materials to form a pattern. In addition to covalent bonds forming, hydrogen bonds can also form between molecules (Figure 26(d)). The last interaction to mention is represented by Figure 26(e) where organic adsorbates can form coordination bonds with metal atoms lying out of the plane of the surface.

These interactions can lead to nanoporous networks, given the molecules have sufficient thermal mobility to rearrange themselves whilst maintaining attraction to the substrate. Grill et al. reported the first network formed by covalent bonding using brominated tetraphenylporphyrin (Br_4TPP) (Figure 27).[114] They demonstrated that by heating Br_4TPP, the bromine would dissociate off of TTP leaving what was assumed to be radicals as 'building blocks' which would covalently link together

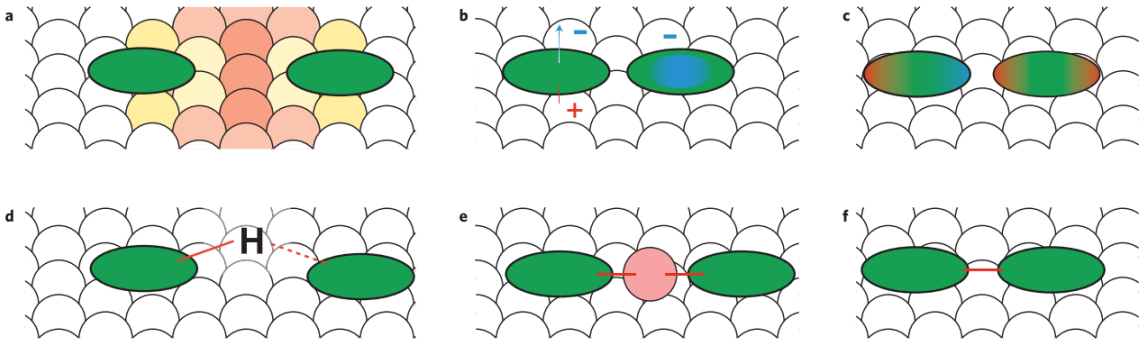

Figure 26: Scheme of six different intermolecular interactions possible on a surface. Adsorbates are shown by a green oval. (a) Interactions between the two molecules are governed by the substrate, (b) an absorbate is charged (shown by the blue circle) and is able to interact with the surface, creating a dipole moment that arranges the molecules on the surface, (c) when organic molecules contain polar groups, it is possible for a molecule to possess a dipole (left molecule) or quadrupole (right molecule) which allows them to arrange on the surface in specific forms, (d) hydrogen bonding between the molecules, (e) organic molecules can coordinate with metal adatoms on the substrate (pink circle) and (f) covalent bond formation on the surface between two organic molecules. Image from [113].

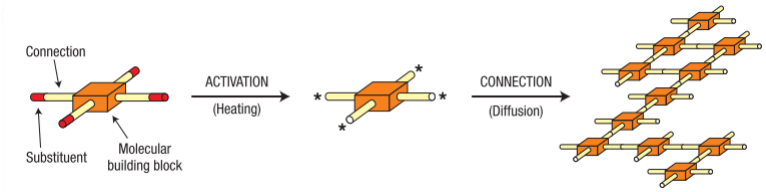

Figure 27: Schematic representation of the process studied by Grill et al. Heating the Br_4TPP monolayers (bromine represented in red) activates the molecule (removal of bromine) in order for a bond to be established between the remaining TPP molecules resulting in a molecular network. Image from [114]

on the surface through thermal diffusion. By varying the amount of bromine on tetraphenylporphyrin the topology of the nanostructures can also be controlled as shown in Figure 28.

Porphyrins are well researched for many reasons including their ability to distort their shape to conform to their environment. They are highly stable and their nitrogen atoms within the macrocycle is ideal for the addition of metal centres e.g. iron, cobalt or magnesium (commonly found in biological systems).[115, 116, 117, 118, 119, 120, 121]

Even without the need for covalent linking porphyrins are able to keep a highly-ordered network through a combination of dipole-dipole interactions as well as

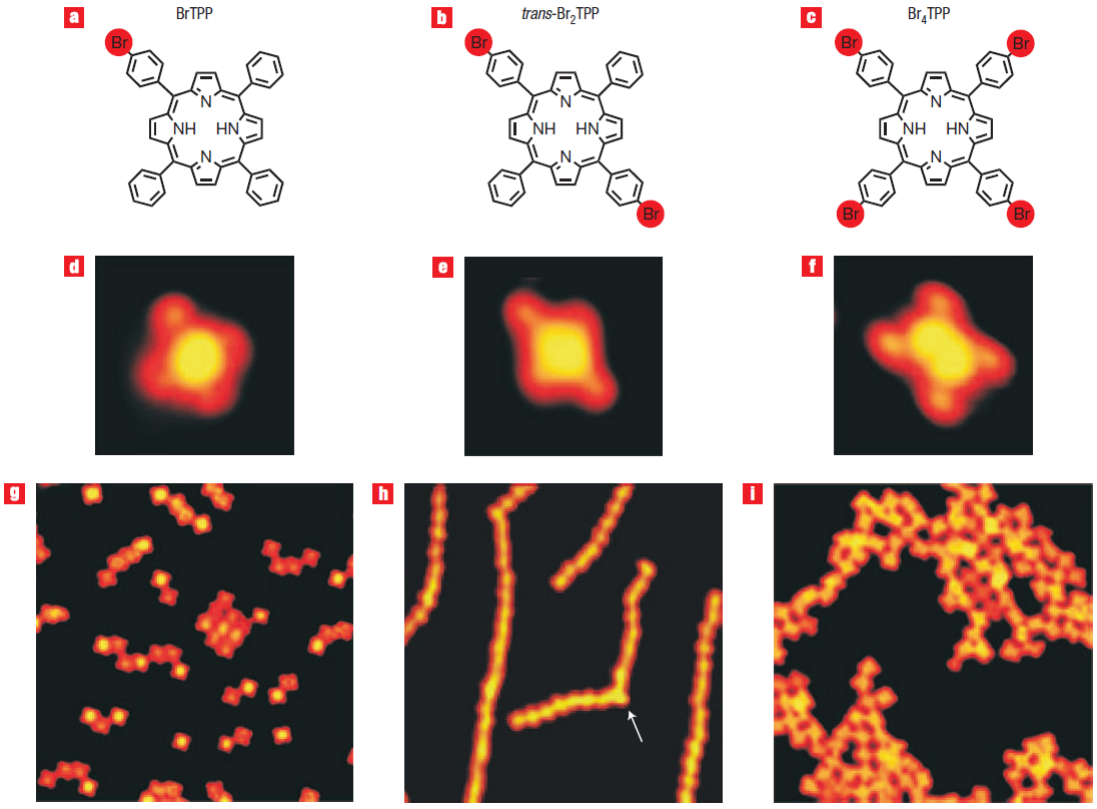

Figure 28: (a-c): Chemical structures of various brominated tetraphenylporphyrin examined by Grill et al. (d-f): Corresponding STM images taken of the single molecule (3.5 nm scans) below. (g-i): STM images of the connected nanostructures after activation (30 nm scans). Image reproduced from [114].

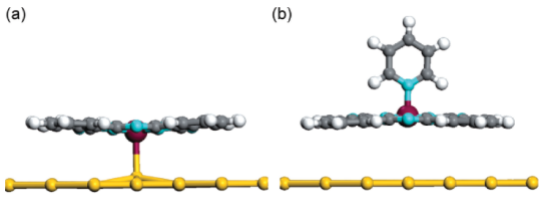

Figure 29: (a) FePc deposited on Au(111), initially the iron centre in the deposited FePc molecule forms a bond with the gold substrate and (b) a pyridine molecule adsorbed onto a FePc molecule where the iron core is now bonded to the nitrogen atom on the pyridine molecule. Image from [128].

through van der Waals interactions.[122, 123]

3.3 3D Assembly

To assemble a three-dimensional structure, the intermolecular interactions between the layers need to be favourable. For this reason, many groups have studied multi-layer components with metal-centred macrocyclic molecules such as porphyrins and phthalocyanines as the high coordination number of the metals means they are able to form multiple bonds in and out of plane. Thus, they are commonly studied in catalysis.[124, 125, 126, 127]

This is shown in a study by Isvoranu's group where pyridine was adsorbed onto a single layer of iron phthalocyanine (FePc) through thermal deposition.[128] Using X-ray photoelectron spectroscopy they confirmed the coordination between the iron centre and the nitrogen on the pyridine altering the spin states and therefore, the magnetic properties.

The commonality between both methods of forming SAMs is that the growth of these layers is dependent on the competition between its kinetics and thermodynamics, with great importance on its surface chemistry.[98] Hence, the uniformity lies heavily on the cleanliness of the surfaces which results in greater challenges when fabricating SAMs in solution. Dust and chemical residues can hinder the quality and ability to achieve full coverage.[129] This could result in changes to the properties studied, mechanical[130], electrical[131] etc.

Ideally, we would now combine the two methods of forming SAMs. With UHV we can obtain a highly-ordered bottom layer to form the foundation while combining

the ease and the benefits of using solution self-assembly.

Chapter 4

Materials and Methods

The first half of this chapter will discuss the preparation methods used throughout this thesis, the two main methodologies mentioned in detail below will be solution self-assembly and self-assembly in ultra-high vacuum (UHV), previously discussed in Sections 3.2.1 and 3.2.2.

Following this, the important aspects of characterising thin-film molecular layers will be described. Characterisation of this work will mainly be based on atomic force microscopy, conductive probe AFM (C-AFM), Seebeck measurements adapting the C-AFM set up and X-ray photoelectron spectroscopy.

4.0.1 Gold Preparation

There are many reasons why gold is a widely used substrate in SAM formation. It is easy to obtain and the preparation methods are simple. Another important advantage of gold is that is fairly inert and does not react with most chemicals, therefore, making SAMs in atmospheric conditions is convenient without the need for a clean room.[97] Other metals have been considered and can offer different advantages such as silver and copper however each has its drawbacks. Silver has a smaller tilt angle than gold and can produce high-quality SAMs as a result of a smoother surface however as it is highly oxidative and toxic to cells making this substrate unsuitable for many applications. Copper, on the other hand, can also produce SAMs of similar quality but its main disadvantage is its reactivity with

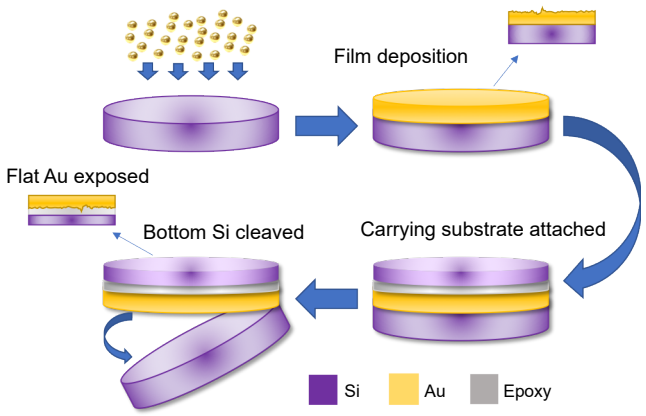

Figure 30: The procedure for preparing template-stripped gold for solution self-assembly. Gold pellets are thermally evaporated onto a silicon wafer creating a 200 nm film of gold. A clean piece of silicon is then glued onto the gold surface using epoxy which is then removed, revealing a flat gold surface ready for molecular deposition. Image from [135].

oxygen and from a practical perspective makes it more difficult to work with.[132, 133, 134]

The type of gold we used for solution prepared self-assembly is template stripped gold, following a modified procedure outlined by Wagner and Weiss (shown in Figure 30).[136, 137] Silicon wafers (5" x 5") were ultra-sonicated in acetone, methanol and isopropanol in series and then cleaned by oxygen plasma for 5 minutes. Immediately after cleaning, Au (99.8%) was thermally evaporated onto the surface with a thickness of 200 nm. A second wafer was cut into smaller rectangular pieces (0.5 × 1 cm) and cleaned as the previous sheet of silicon. After cleaning, they were glued onto the gold using Epotek 353nd epoxy adhesive and cured at 150°C for 40 minutes. When preparing new samples, a fresh piece of gold is cleaved with a scalpel revealing an atomically flat gold surface which is immediately immersed in a molecular solution.

When preparing samples *via* thermal sublimation, the sample was made typically be made in ultra-high vacuum environments, where the surface was cleaned by sputtering and annealing.[138, 139] In this research Au on mica was purchased from Georg-Albert-PVD and underwent sputtering and annealing before molecular deposition. Rectangular pieces of gold were placed on top of a small silicon piece and clamped into a heater stage that can be slotted into the manipulation arm. A steel

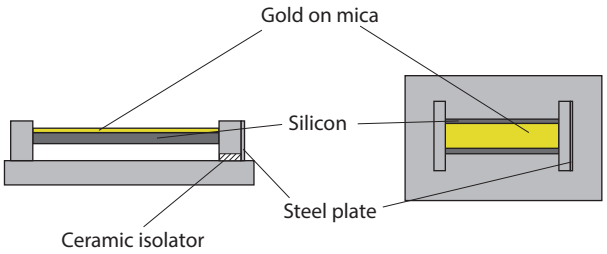

Figure 31: A simple diagram showing the heater stage used for UHV. A piece of gold on mica is placed on top of silicon for annealing and clamped together. The steel plate on the end is then in contact with the transfer arm for heating.

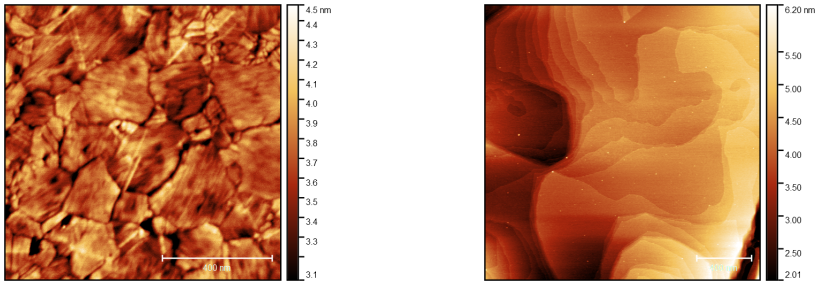

(a) (b)

Figure 32: Topography of (a) template stripped gold (1 µm scale) and (b) sputtered and annealed gold on mica (1.5 µm scale).

plate at the end of the heater allows resistive heating to occur across the silicon, in turn heating the Au on mica. The gold underwent ion bombardment with 1.0 keV Ar^+ ions for 30 minutes and was annealed at ~400 K for 30 minutes. This process was repeated twice to ensure an atomically flat surface.

In both cases, the roughness of the gold was previously checked by AFM on 3-5 random areas to ensure surface quality and was found to be consistently less than 0.1 nm. A comparison of these two methods is shown in Figure 32. The roughness found on sputtered and annealed gold (Figure 32(a)) was typically found below 30 pm whereas template stripped gold (Figure 32(b)) showed a higher roughness average of 80 pm. The difference in roughness is not likely to affect the uniformity of the SAM as this is mostly dependent on the deposition method.

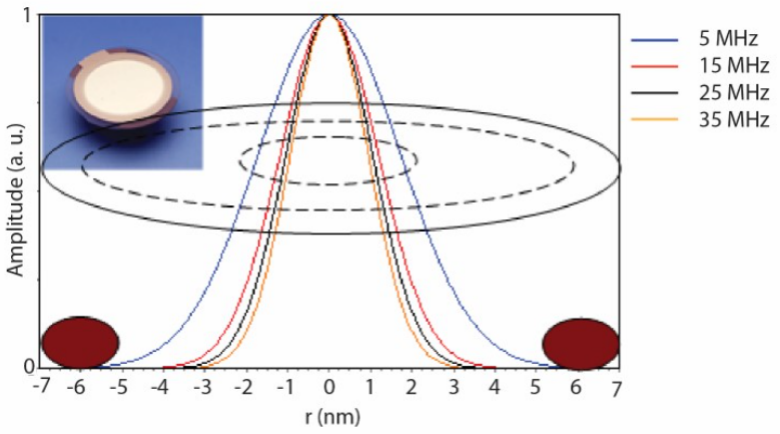

Figure 33: Gaussian distribution of the crystal oscillation at frequencies: 5, 15, 25, and 35 MHz. The dashed lines representing the top and bottom of the electrodes. (Smaller - bottom, larger - top.) [141]

4.0.2 Quartz Crystal Microbalance (QCM) in Vacuum and in Liquid

To begin the formation of SAM preparation, it can be useful to estimate growth parameters before making a sample. Quartz crystal microbalance (QCM) is a highly sensitive technique that can detect nanogram to microgram changes in mass per unit area.[140] Because quartz is a piezoelectric material, after inducing a voltage through metal electrodes, the quartz can oscillate at certain frequencies (typically between 5 – 10 MHz, although higher frequencies can be found).

The amplitude of the oscillation will vary across the crystal and this is figuratively shown in Figure 33. With standard circular QCMs, the point where the electrode experiences the maximum amplitude is where r equals 0, i.e. the centre of the disk. This oscillation frequency will change when adding or removing substances on its surface and can be monitored in real-time. However, the frequency will depend on the location of the particle on the amplitude at that point so this must be considered. The Sauerbrey equation takes this into account and assumes an evenly distributed layer on the surface which in turn can be used to determine the change in mass using the Sauerbrey equation[142]:

$$\Delta f = -\frac{2f_0^2}{A\sqrt{\mu_q \rho_q}} \Delta m \tag{4.1}$$

where Δf is the difference in frequency (Hz), f_0 is the initial resonance frequency (Hz), Δm is the change in mass (g), μ_q is the shear modulus of quartz for AT -cut crystal (typically found $2.947 \times 10^1 1$ g.cm^{-1}.s^{-2}) ρ_q is the density of the quartz (2.648 g.cm^{-3}) and A is the piezoelectric area (cm^2).

QCM measurements for SAMs growth in solution throughout this work were measured using a gold electrode with a 5 mm diameter and a resonance frequency of 5 MHz monitored by an OpenQCM Q-1. To determine growth in solution, the frequency of the crystal was measured after cleaning (rinsing with acetone, methanol and iso-propanol in series and then cleaned by oxygen plasma). The clean crystal was then immediately placed into a solution of molecules for a set period of time, repeatedly. The growth rate on the QCM was recorded after each submersion and comparing them with the initial frequency the Sauerbrey equation (eq. 4.1 can be adapted to give the amount of molecules present on the surface:

$$n = \frac{-\Delta * A * k * N_A}{M_w} \tag{4.2}$$

where k represents:

$$k = \frac{\sqrt{\mu * \rho}}{2 * f_0^2} \tag{4.3}$$

At full monolayer coverage the area per molecule can be calculated as such:

$$A_{molecule} = \frac{A_{electrode}}{n} \tag{4.4}$$

Initially, QCM had been a technique utilised only in the vacuum/gas phase and around 20 years after this, the technique was implemented in the liquid phase too.[143, 144, 145]

In contrast to liquid QCM, QCM used in UHV was used to monitor deposition rather than growth. The frequency change under vacuum was detected by an INFICON STM-2XM rate/thickness monitor with a gold quartz crystal of 5 mm diameter and 5 MHz frequency. Data was obtained by heating the molecular cell containing the

desired molecule at 5-10 K intervals until the rate of thickness dropped or stopped. The rate of thickness was noted after keeping the molecular cell at a constant temperature for 20 minutes. Plotting these results then allowed for an estimate of the sublimation temperature of the molecule to begin thermally depositing material. Typically, the molecules will require degassing to remove impurities within the cell.

4.0.3 SAMs preparation

Liquid Phase

The general procedure for preparing SAMs involves immersion of a clean substrate in a diluted solution of the molecule (Figure 34). As thiols have already been extensively researched, the concentration, choice of solvent and submersion time have already been optimised for reproducibility and convenience.[100, 110, 112, 97] Typically for thiols ∼1-10 mM ethanolic solutions are used with a deposition time between 12 and 18 hours at room temperature. In fact, ethanol has advantages which allow for it to be used in many other SAMs preparation. It is relatively cheap, can have high purity $\geq$ 99.8% and its toxicity is relatively low.[97] The kinetics of formation are largely dependent on solvent and so the choice of solvent needs careful consideration. The mechanisms of assembly are complicated and adding further parameters such as solvent-substrate and solvent-absorbate interactions to an already complex matter makes the thermodynamic and kinetics of assembly hard to predict. Solvating molecules must have greater attraction to the substrate over solvent molecules as the solvent molecules are in abundance they will need to be displaced from the surface before adsorption of the molecules can happen.

Although the process of adsorption of molecules onto the substrate can happen within a few seconds, longer immersion times are required to optimise the reorganisation process and maximise the order whilst minimising the number of defects in the film.[147]

Kafer's group in 2006 showed through reflection adsorption infrared spectroscopy (RAIRS) the importance of solvent on the chemical composition of adsorbates (Figure 35). They had tested a range of solvents: toluene, THF, DMF, DCM, acetone,

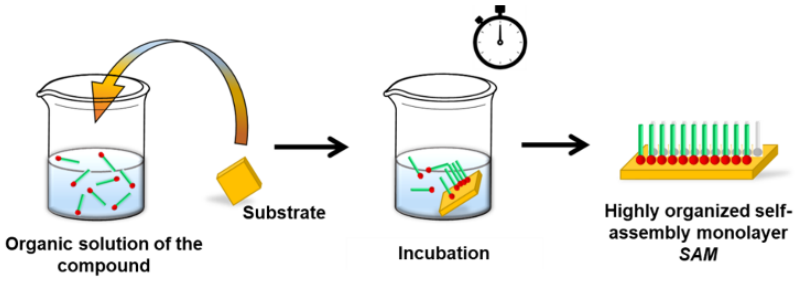

Figure 34: Schematic showing the preparation method of SAMs in solution. The substrate Image from [146].

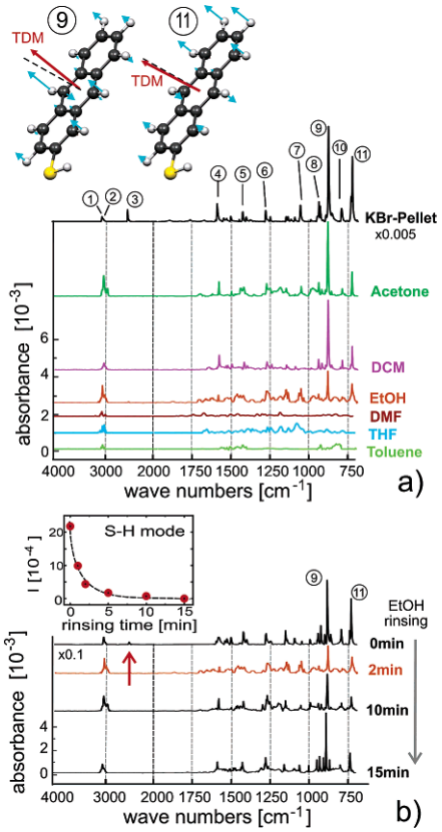

Figure 35: RAIR spectra of anthracene-2-thiol from Kafer et al.[148]. (a) Different solvents with rinsing time of 2 minutes. (b) Different rinsing times, highlighting the absorbance of S-H mode after each interval of rinsing time.

and ethanol on anthracene-2-thiol on Au(111).[148] Looking at the spectra of the various solvents, it is evident that toluene, THF and DMF solutions show extremely weak absorbances compared to acetone, DCM and ethanol. Continuing with the use of ethanol for further studies, they proceeded to compare RAIR spectra for different rinsing times and an unrinsed sample. The unrinsed sample shows much larger absorbance than the initial AnT sample prepared from ethanol or DCM indicating the presence of multilayers (Figure 35(b)). As the time of rinsing progressively increased, the peak arising from the stretch mode of S-H decreases until it disappears at around the 5 minutes mark. Additionally, the width of the peak and spectra lines becomes narrower as the physisorbed multilayers are removed.

For the work in this study, we used an incubation and rinsing method. The exact process was optimised for each molecule study. Full descriptions are therefore available in the experimental chapters.

Vacuum Phase

An alternative method to prepare thin and monolayer molecular films is by thermal evaporation under UHV conditions. Thermal evaporation involves heating a pure molecular powder to its sublimation point, creating a directed beam of single molecules that can be positioned over the sample substrate. Thermal evaporation is exceptionally clean, it can be used with most molecules, and it can grow films with excellent precision from just a few molecules per 100 nm^2, to micron thick films. It also allows us to avoid complications arising from solvents during preparation, however, whilst this can be a major benefit, thermal deposition has its own limitations as discussed below.[149] Although the principle is just as simple as growth in solution, there is a need for more specialist equipment and the substrate will need to be prepared and cleaned.

The UHV system that has been used for this research is displayed in Figure 36. To ensure high pressures (10^{-10} mbar) are maintained, an ion pump and turbo molecular pump are connected to the chamber directly. The system is primarily split into two main parts: the main chamber and the load lock. The load lock is regularly vented and pumped so that the heater stage can be inserted and removed using a linear translator with rotary motion. This can then be moved in and out of the

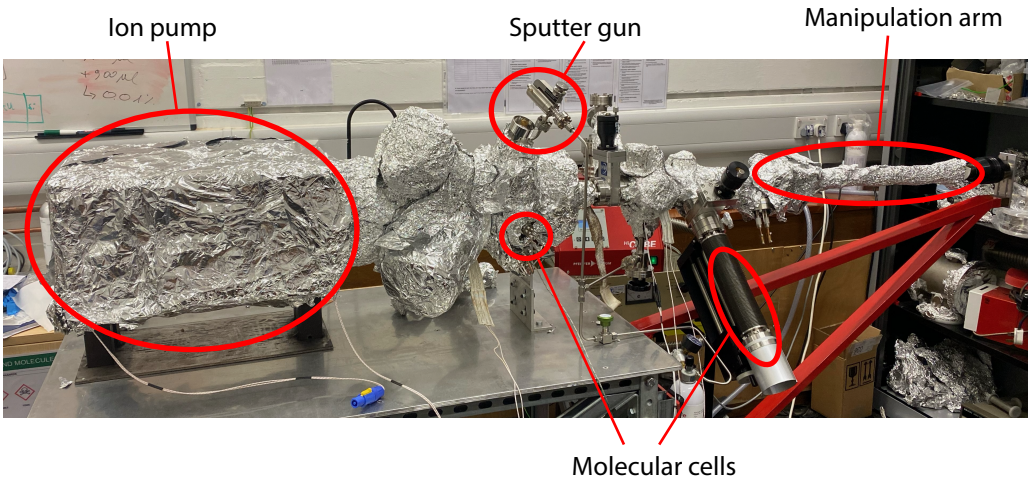

Figure 36: A photograph of the UHV system used in this thesis. The ion pump is connected to the main chamber where the sputtering and annealing of the gold occurs. The sputter gun is highlighted in the figure and the manipulation arm is where the piece of gold is held. There are two points within the chamber where molecular cells can be positioned where molecular deposition occurs.

main chamber for sample preparation, where sputtering from Ar ions and molecular deposition takes place. To perform thermal sublimation, crucibles of ∼2.5 cm are cut from borosilicate glass into a test tube shape for containing the molecules. Chromel and alumel wires are sealed within the lower part of the crucible to produce a K-type thermocouple for direct measurement of crucible temperature. The molecules were then heated by resistively heating a tantalum wire wrapped around the crucible. An image of the molecular cell is shown in Figure 37a. After warming the cell for 20 minutes at the desired deposition temperature (allowing for stabilisation of the temperature and sublimation rate), the gold substrate was then brought in front of the cell for deposition.

There are three main routes for epitaxially grown thin films on a crystal surface: layer-by-layer (Frank-van der Merwe); layer-plus-island (Stranski-Krastonov); and island (Volmer-Weber) growth, represented in Figure 38.[150]

Frank-van der Merwe growth happens when the attraction of the atoms of the adsorbate to the surface is stronger than to themselves. On the other end of the spectrum, when deposit atoms are more likely to bind with themselves than the surface, they can form large islands. In between these two extremities, commonly observed is the Stranski-Krastonov (SK) mode. This is a mixture of the two previous modes,

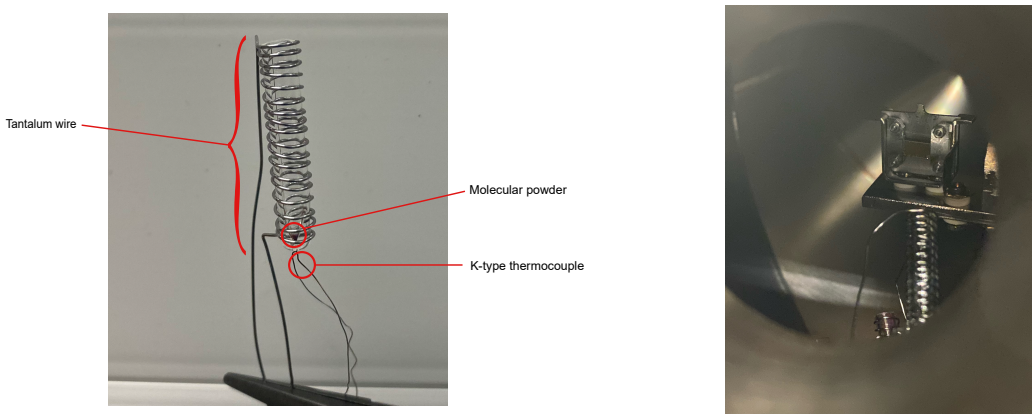

(a) (b)

Figure 37: (a) Photo of a crucible wrapped in tantalum wire. (b) Picture of how the gold is aligned with the molecular cell.

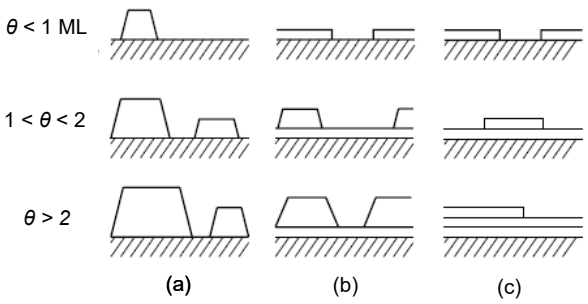

Figure 38: Three primary mechanisms for epitaxially grown thin films. (a) Volmer-Weber (island growth), (b) Stranski-Krastonov (layer-plus-island growth) and (c) Frank-van der Merwe (layer-by-layer growth). Image taken from [151].

layers will form when there is a monolayer or less coverage on the surface. Any more than this, islands begin to form on top of this monolayer. Layer growth arises when atoms A are deposited on B, $\gamma_A < \gamma_B + \gamma*$, $\gamma*$ being the interface energy or island growth. So in the context of SK growth, as layer thickness increases, the energy of the interface also increases.

It has been previously reported that thermal annealing after deposition can greatly improve the quality of film growth. Providing the surface atoms with enough energy to diffuse and reconstruct means that the following layers will contain fewer defects improving the crystallinity.[152]

4.1 Scanning Probe Microscopy

A widely used analysis tool in nanoscience is the use of scanning probe microscopes (SPM). SPM encompasses many techniques for imaging surfaces at the atomic level. The first breakthrough came from Binning and Rohrer in 1982, they invented the scanning tunnelling microscope (STM), an extremely popular technique to date that exploits the quantum tunnelling phenomenon.[153] A major limitation of this is that as the imaging signal relies on the tunnelling current between the tip and the sample, the studies can only be useful to conductive samples. They are also commonly used *in situ* UHV systems to maintain clean surfaces. In response to this problem, in 1986, Binning and Gerber developed an alternative method – the atomic force microscope (AFM).[154] The principle for an AFM came from combining the STM and the profilometer together. A tip is mounted onto a cantilever, usually referred to as a probe, bends under certain forces from the sample. The cantilevers made today usually consist of silicon and can be coated with other materials to alter the properties, for example, coating with diamond to produce conductive probes. The advantage AFMs have over STMs is due to their versatility and adaptability. By modifying the cantilever, properties other than the topography can be investigated such as electric and magnetic properties and chemical potentials. It offers advantages over STM, it can image in 3D as opposed to the STM which shows in 2D. With AFMs, the contact area of the cantilever is known and so, the contact area of the junctions can be calculated which is important in order to obtain conductivity values.

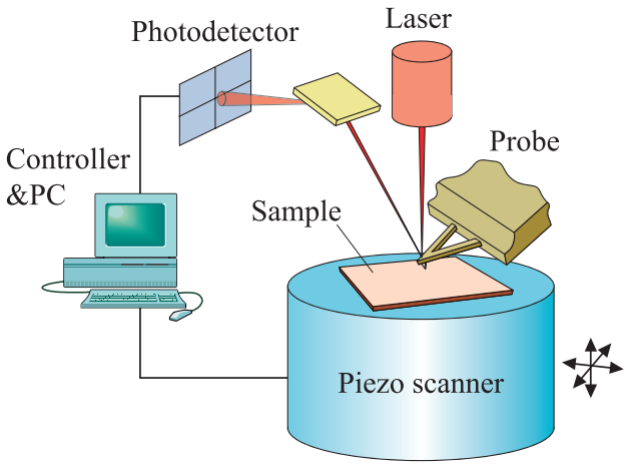

Figure 39: Illustration of an AFM taken from [155]. The sample is brought closer to the tip by a piezoelectric scanner which allows nanometric distances. A laser beam is reflected off the back of the cantilever and into the photodetector.

We can additionally have more precise control over the force, avoiding damage to the sample surface.

4.1.1 Principle of AFM

The working principle of AFMs is based on the probe scanning across the surface either in contact or 'tapping' along the surface of the sample. These measurements rely on many interacting forces such as vdW, electrostatic, capillary, chemical and repulsion forces. Three possible vdW interactions could be present: dipole-dipole, dipole-induced dipole, induced dipole-induced dipole. By summing up all the dipole interactions, we get the overall vdW forces that become the Lennard-Jones potential described in Section 3.1.2. A laser beam is then reflected off the back of the cantilever into a photodetector split into four sections. The deflection of the laser shifts within the four segments when there is movement on the cantilever generating different voltages which can then be converted into a topography of the surface sample. A schematic of an AFM is shown in Figure 39, the sample is attached to a piezoelectric scanner which can control the very small sample-tip distances (nm range). The movement of the piezo will be determined by the mode of AFM used, where different modes will utilise different feedback methods to map the topography.

4.1.2 AFM Modes

The versatility of AFM makes the instrument very successful in this field and different modes have been developed for use in mediums such as air, UHV and liquid.

Contact Mode

Contact mode, also known as static mode, is the first mode created and the simplest way of operating an AFM. In its simplest terms, this is the mode where the feedback system relies on the force between the sample and tip to remain constant. The first few AFM images were carried out in contact mode where the groups presented what were thought to be atomically resolved images on graphite and NaCl in ambient and UHV conditions, respectively.[156, 157] While these results showed the lattice spacing of the samples, atomic defects such as vacancies and step edges were not observed. The forces interacting between the sample and tip are much greater compared to the force of a single atom on the tip to the sample and the assumption is that not just a single atom on the tip interacts with the surface but many of the tip atoms are involved. Figure 40 shows the forces present during an AFM scan and its corresponding force-distance curve. The difficulty here lies in the feedback system of keeping a constant force for imaging.[158] The short-range forces are dominating (dark blue atoms/curve), creating a non-monotonic curve of its overall force. As contact mode operated in the repulsive regime, another major challenge for contact-mode AFM is the need for softer cantilevers in the repulsive range to prevent surface deformation (around 10 N/m).[159] The soft cantilevers then become an issue when approaching the sample as the distance closes the attractive forces 'snaps' the cantilever towards the sample uncontrollably, also known as the 'jump-to-contact' phenomenon.

Achieving true atomic resolution with contact mode is challenging however can be done with chemically inert samples where attractive forces are not overpowering (a negative loading force is applied to counteract the VdW forces or it is carried out in liquid).[160, 161]

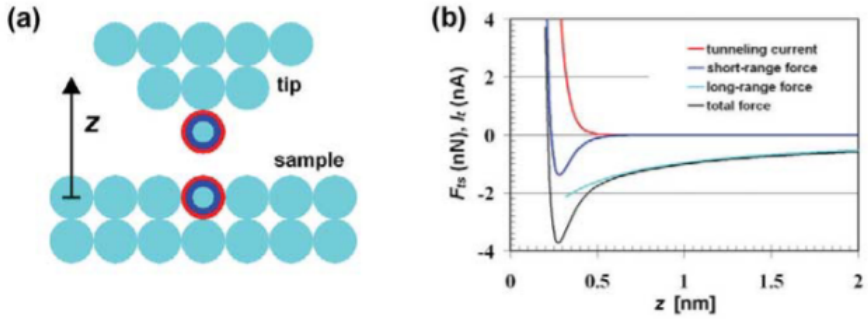

Figure 40: (a) Diagram representing the forces between a tip and a sample surface. (b) Force-distance curves of the dominating interactions with varying distances.[158]

Non-contact AFM

The optimal region for molecular resolution imaging is within the attractive range and around a decade after the invention of the AFM, another method was created: non-contact, dynamic mode AFM. Non-contact AFM overcomes some of the major challenges brought about by contact AFM. Jump-to-contact can be avoided by exciting the cantilever to oscillate at an amplitude large enough such that the withdrawing amplitude is bigger than the attractive forces. The two well-known and widely used modes that follow this principle are known as frequency modulation (FM) and amplitude modulation (AM) AFM, shown in Figure 41. In frequency modulation, the cantilever oscillates with a certain amplitude at its resonance frequency. This frequency will change depending on the forces of the sample compared to its forces when far from the sample. The shift in frequency is then kept constant used to profile the sample topography and produce an image.[162] The resulting image is then formed of the surface topography by keeping the frequency shift at a constant value.[163] Originally, FM AFM has been used for experiments in UHV however in recent years it has expanded for use in liquids.[164, 165] Despite having some success in liquid environments, due to the fact that two feedback loops must be maintained the operation is slow and therefore not as suited in air and less commonly used for liquids.

Amplitude modulation AFM is also commonly known as 'tapping mode' uses a feedback mechanism where the amplitude oscillation is monitored to provide the surface topography. Similar to FM, the cantilever is excited either at or close to its resonance frequency however this frequency will be kept constant throughout.[166]

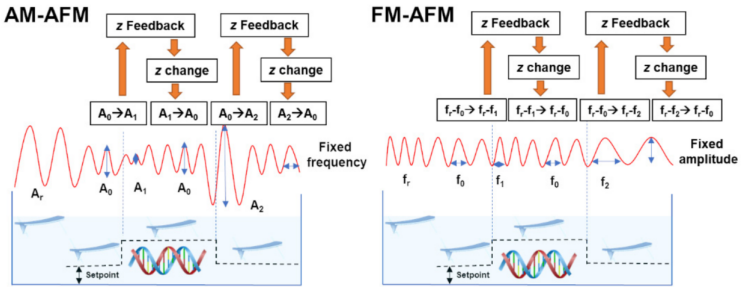

Figure 41: Working principle of AM AFM (left) of scanning DNA structure where the frequency is kept constant and FM AFM showing how constant amplitude would change the frequency (right).[167]

More specifically, the system will compare the amplitude close to the surface (A_i) and its reference value also called its amplitude set point (A_{sp}), keeping the root mean square value of the difference in oscillation amplitude constant. The error signal between A_i and A_{sp} is kept to a minimum and this is achieved through voltage signals sent to the piezo z scanner to adjust the spatial difference between tip and sample. Both these methods are viable to achieve atomic resolution images and are also advantageous to preserve tip sharpness.

Some of the forces present in an AFM have already been mentioned throughout this section, however, one of the main forces to note is the capillary force under ambient conditions. This is inevitable and observed in both static and dynamic modes.[168, 169] The vapour in the air will spontaneously condense onto hydrophilic surfaces creating a meniscus between the sample and the tip during measurements. Figure 42 shows the hysteresis effect of the capillary effect on the force curve of approaching and retracing a probe during a scan. The effects of the capillary force can be seen when retracting the probe, more force will need to be exerted on withdrawing the tip from the sample which then causes further deflection of the laser. This could disrupt the surface-tip interactions and become overpowering, limiting the atomic resolution of the image. Another major limitation is the noise, mostly arising from the thermal noise in the cantilever. This causes 'thermal drift' where features in the images become elongated and slightly distorted.[170]

PeakForce Tapping is an imaging technique developed by Bruker similar to the dynamic modes described above. Instead, the probe oscillates far below its resonance frequency, the peak force is constant at around 10 pN compared to the usual 1

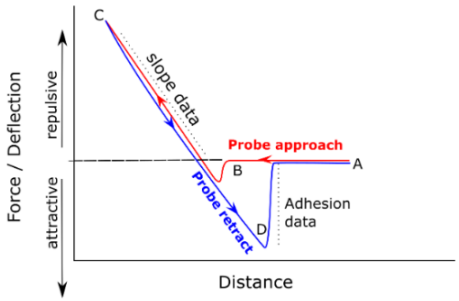

Figure 42: Force-distance curve from approaching and retracting a probe from the surface.[171]

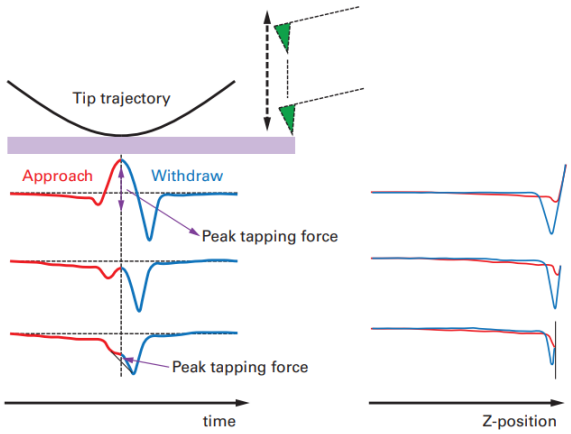

Figure 43: Force-time curve of the cantilever operated in PeakForce Tapping with force-distance counterpart.

nN. It is a mode that is optimised for imaging soft samples and minimises the lateral damages because the tip now withdraws following a sine wave rather than a triangular one as seen before (Figure 43). The plots represent a silicon probe approaching a silicon surface, on the left shows a force curve vs time and the right shows a force curve against the z-position. The last force curve on the left shows the effect of imaging at low forces with PeakForce mode. Therefore, when withdrawing the tip the pulling force from the capillary force is reduced. By operating at a force considerably lower than Bruker's conventional TappingMode, the chances of obtaining high-resolution images on soft samples improve greatly. For this reason, the AFM experiments carried out in this project are performed in PeakForce mode with the exception of scratch tests which are done in contact mode. This is to ensure that the molecules will be swept aside to create a square where the height difference can be estimated.

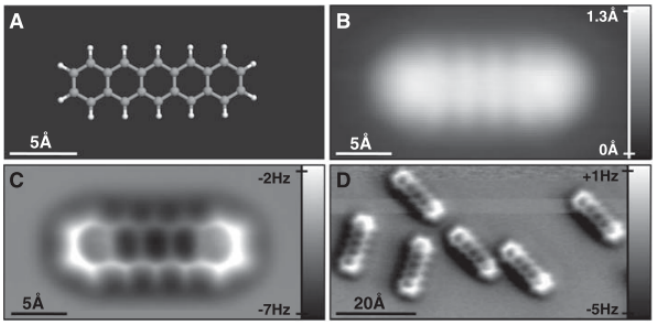

Figure 44: Images taken from [173]. (A) Ball-and-stick model of pentacene. (B) STM image taken with CO-functionalised tip. (C, D) AFM images taken in constant height mode.

Potentially because of these issues the community has provided few reports on atomically resolved images with AM AFM. One of the first submolecular AFM images was taken in FM mode using a qPlus set-up.[172] Asides from this study, another key finding came from Gross et al. in 2009 successfully showed that by functionalising a tip, they were able to achieve resolution of the internal bond structure of pentacene.[173] Images of pentacene in STM and AFM were taken, shown in Figure 44. The conditions for success are impacted by the choice of the molecule for tip functionalisation. It must weakly react with the surface adsorbate and the radius must be smaller than that of the molecule to display atomic features. In this case, CO was purposely picked up and attached to the tip, exposing the oxygen atom. The oxygen atom is attracted to the pentacene molecule, closing the distance between them so much so that there will be a slight repulsion from the Pauli exclusion principle.

4.1.3 Electrical AFM

Conductive AFM

Conductive AFM (C-AFM) measurements are used in contact mode to measure the sample's current at the point of connection to the tip. This mode can simultaneously map the topography and produce a current map using the same principle with a laser and photodiode as described above. A bias voltage needs to be applied between the sample and the tip and can only be used for conducting materials, like an STM. However, compared to an STM, C-AFM overcomes the disadvantage of the inability of STMs to distinguish whether the features of the image generated originate from

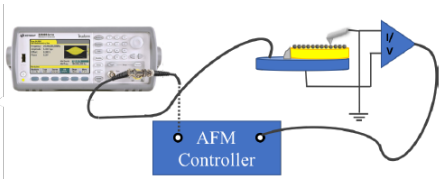

Figure 45: Schematic of C-AFM set-up employed throughout this thesis. Image from [135].

changes in topography or sample conductivity. As established, with C-AFM there are two feedback loops, the profile and the current, therefore silicon cantilevers typically used in AFM are coated with a thin film of conductive material – Pt, Au, Cr, diamond or even graphene.

Throughout this thesis, point measurements will be performed on the samples to gain information about the electronic transport and to determine their conductance. Figure 45 shows the C-AFM set-up implemented in this work. An Agilent 33500B waveform generator was used to apply a triangular wave voltage to the sample and a probe holder was modified to receive the current flowing from the sample. The current was then converted into a voltage by a FEMTO DLPCA-200 low noise I/V convertor.

Typically, the data collected is first processed into an I-V curve which will have similar characteristics to the plot shown in Figure 46. Osorio et al. carried out electrical characterisation of single oligo(phenylene-ethynylene) (OPE) molecules vs in a SAMs (via Langmuir-Blodgett) using STM.[174] From this curve, histograms could be plotted to determine the molecular conductance and they found that the conductance value of OPE in a SAMs and as a single molecule are at 5.17×10^{-5} G_0 and $5.39/3.16 \times 10^{-5}$ G_0 (the different values are due to the different adsorption sites).

By following the method stated above (via C-AFM) for obtaining conductance values, after the plotting of I vs V, heat maps can be generated. Presented by Wang et al., are electrical conductances for zinc tetraphenyl porphyrin samples prepared in three alternative deposition methods: 1) Langmuir-Blodgett, 2) thermal sublimation, and 3) self-assembly (Figure 47). The key results show that as the film thickness increases the conductance decreases in line with what was reported previously.[77]

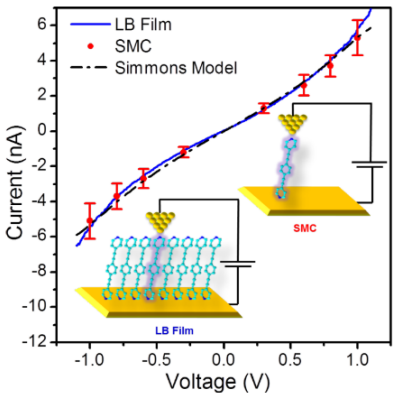

Figure 46: I-V curve of an OPE monolayer, the error bars show the deviation taken from the conductance histograms.[174]

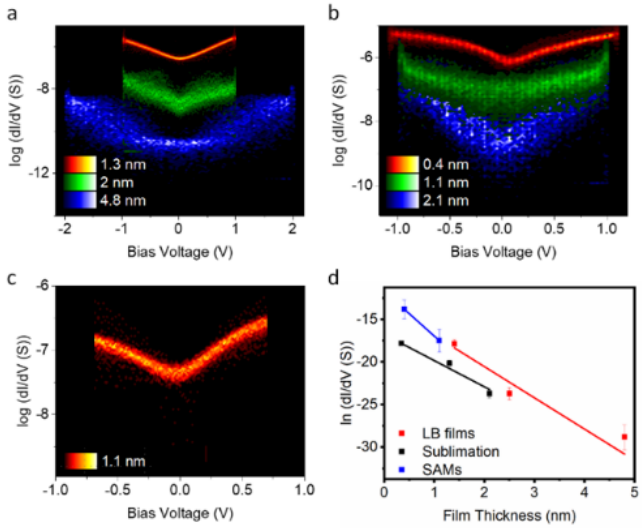

Figure 47: Electrical conductance heat maps of ZnTPP films via (a) LB, (b) thermal sublimation, and (c) self-assembly growth methods and their corresponding thicknesses. (d) Conductance (log scale) vs film thickness.[77]

Thermoelectric Measurements with AFM

To observe the Seebeck effect, the thermal voltage of the samples is needed to be known. Therefore, a technique was developed based on the principles of C-AFM as one of the benefits is its nanometric resolution. (Shown in Figure 48). An additional advantage is the precise control C-AFM provides. The key difference between the set-up of a C-AFM measurement to a thermoelectric measurement is the inclusion of a heater and a voltage pre-amplifier to measure the thermal voltage as opposed to the current between the Au substrate (source) and the conductive probe (drain).

To do this, a copper plate was initially glued to a Peltier heater (9 x 9 mm, purchased from RS Components Ltd) with an epoxy thermal adhesive. The copper plate attached to the heater connected the ground of the Peltier heater to the same ground as the microscope. A thin layer of mica was then sandwiched in between two pieces of copper foil and thermally glued atop the Peltier device surface. The purpose of the mica was to act as an insulating layer to the sample. The sample would then be attached to the copper plate via electrodag. The molecular thin film would also be electrically connected to the copper plate by electrodag.

The Peltier heater was heated to four different temperatures by DC voltage with the use of an Agilent Technologies 33400B waveform generator, amplified by 10. Calibration was performed with a freshly cleaved template stripped Au sample. Four key voltage set points were determined at -20, 0, 6 and 16 volts. These voltages correspond to four temperatures: 18, 22, 25 and 30 °C on the surface. Previous work performed by Lamantia et al. [135], calibrated the temperature of the Au substrate and the temperature of the probe. An SR 550 Stanford Research System high impedance differential pre-amplifier was used to monitor the voltage difference between the sample and the tip at zero bias. This signal was then passed through a low pass filter to filter out the 50 Hz electrical noise. The final signal was then processed by the Nanoscope controller.

The thermal voltage was then calculated using the '0 current mode', $S_j = S_{Au} - \frac{\Delta V_{th}}{\Delta T}$, where V_{th} is the direct voltage measurement and S_j is the Seebeck coefficient of the junction. S_{Au} is the Seebeck coefficient of the gold substrate. During measurements, a Pt-coated probe (thermally and electrically conductive, with a 50 nm curvature

(a) (b)

Figure 48: (a) Side profile of the sample plate used for thermoelectric measurements. (b) Set-up used for thermoelectric measurements.[135]

radius) was used as both the top electrode and thermal sink. All electrical and thermoelectrical measurements were done in single-point spectroscopy, where all data was taken in a single point with a force set point of 2 nN. Multiple measurements were then performed on different points of the same sample. XYZ data was extracted from the AFM images, with the Z values converted into a matrix and used for analysis.

4.2 X-ray Photoelectron Spectroscopy (XPS)

Self-assembled monolayers make up a very small amount of the sample if we take into account the thickness of the gold substrate. In the example of template stripped gold, we have a thickness of 200 nm, whereas the thickness of molecules will have an average height of 2-3 nm. The XPS measurements carried out in this thesis were performed on a Kratos AXIS Supra. Considering the ratio of the bulk and surface, analysing the SAM would require an instrument that would be highly sensitive and successful at filtering out the effects from the bulk atoms.[175] X-ray photoelectron spectroscopy (XPS) is a suitable technique to study chemical compositions on or within a material. There are two types of electronic orbitals – the ones that partake in bonding with other atoms are known as the valence orbitals and those closely bound to the nucleus are the core orbitals. The fundamentals are based on the photoelectric phenomenon, where electrons are emitted after absorbing electromagnetic radiation. In this case, X-ray photons with the energy $h\nu$ are used to induce electron emission. The energy is measured from the emitted electron and converted into kinetic energy E_K by the spectrometer (a schematic of this is shown in Figure 49). The E_K can be related to the binding energy E_B by adapting the photoelectric

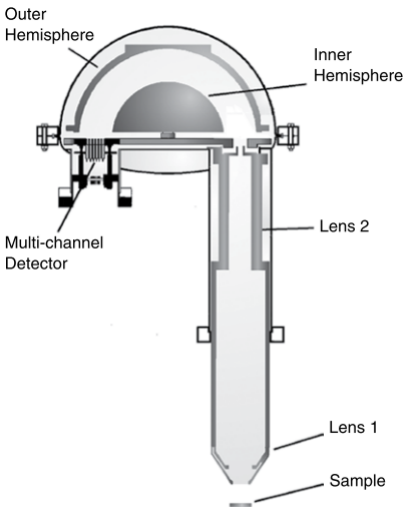

Figure 49: Schematic of a modern hemispherical sector of an XPS instrument. Image from [175].

effect equation (where Φ is the work function of the spectrometer):

$$E_B = h\nu - E_K - \Phi \tag{4.5}$$

The data is then presented as a graph of counts per second (intensity) against the electron energy. The binding energy of the electron is what defines the element specifically, the kinetic energy is determined by the energy of the X-ray source of the system and therefore, is not an intrinsic property of the atom. The calculation of the binding energy will be typically performed within the software of the instrumentation. Although the X-ray beams penetrate microns below the surface, the kinetic energy necessary needed to remove photoelectrons produced from the sample is only sufficient enough at the surface.[176] These electrons escape with no energy lost and this kinetic energy is measured, shown as significant peaks seen in an XPS spectrum. These spectra will then look similar to Figure 52. The photoelectrons produced within the bulk will also undergo inelastic scattering however will not have the kinetic energy to leave the sample. The photoelectrons closer to the surface will be emitted from the surface with very low kinetic energy which in turn will contribute to the background of the spectrum also known as Bremsstrahlung radiation.[177] The electrons which are emitted into the vacuum then enter the analyser via the entrance slit of the spectrometer. The angle at which photoelectrons

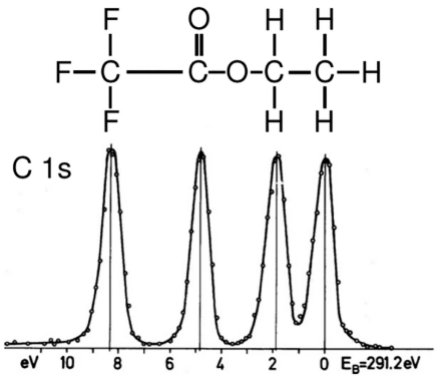

Figure 50: Chemical structure of an ethyl trifluoroacetate molecule highlighted are the carbon atoms and its chemical environments. The corresponding binding energy is represented below and scaled to a C——C / C——H carbon 1s reference peak. Image from [177].

are able to enter the analyser can then be selected is called the acceptance angle, which is beneficial for analyses such as angle-resolved XPS. Lower angles tend to have better angle resolving power. Electrons will then travel through the hemispherical analyser with various energies which are collected with a multichannel detector. This determines the intensity profile of the peaks produced.

4.2.1 Chemical Shifts

XPS is highly sensitive to changes in the valence orbitals from the formation of bonds affecting the position of the core-level peaks of that specific atom. Figure 50 shows an ethyl trifluoroacetate molecule with four different clearly resolved peaks corresponding to the four different carbon environments visible: CH_3, C——O, O——C═══O, and CF_3. As the negative charge density on the atom increases, the kinetic energy of the emitted photoelectrons also increases, resulting in lower binding energy.[178, 179]

Considering this example, the carbon bonded to three fluorine atoms would have the highest negative charge density of the four carbon atoms due to the electronegativity of the fluorine. This gives an approximately 8 eV split from the carbon with the lowest negative charge density, CH_3. This phenomenon which causes a shift in the peaks is known as a chemical shift.

As we have already established thiol-terminated SAM formation is already very well

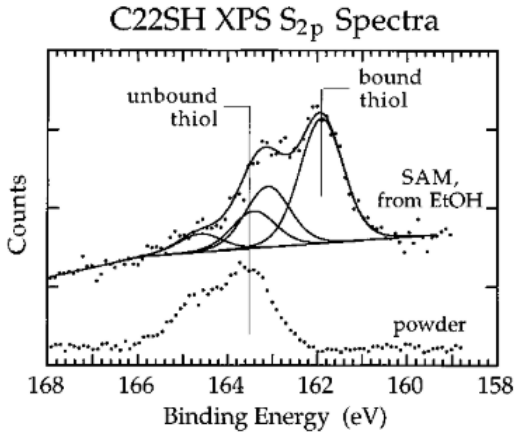

Figure 51: Above: XPS of $C_{22}SH$ SAM monolayer with EtOH solvent. Below: XPS of $C_{22}SH$ powder form.[182]

studied, this is also the case for XPS measurements performed.[180, 181, 182, 132, 183] It was found that the presence of sulphur produces a doublet peak because of the spins of the 2p orbital, $S_{2p3/2}$ and $S_{2p1/2}$.The splitting between the two peaks is widely accepted at 1.2 eV and the peaks are fitted with a 2:1 area ratio. The binding energy of the $S_{2p3/2}$ peak of an alkanethiol bound to gold, lies at 161.9 eV. This is can be confirmed by direct comparison to its powder counterpart shown in Figure 51. Unbound thiol is identified at energies between 163.5 and 164 eV and these assignments can, in turn, provide information on the assembly of the monolayers.

Whilst the photoemissions from the core orbitals of atoms stay largely the same when atoms form bonds with other elements the binding energy can experience changes and so, XPS offers an advantage where the chemical environment of the surface can be analysed.

Isvoranu et al. showed this in a study where pyridine was adsorbed onto a monolayer of iron phthalocyanine (FePc).[128] The N1s photoemission for a monolayer of FePc shows a single peak located at 398.25 eV however as the addition of pyridine increases, two additional peaks become present at higher binding energies, suggesting that there are multiple adsorption sites. The chemical nature of the peaks can be determined using least-squares fits and in this case, three different species were identified; the first peak was assigned to the nitrogen atoms within the FePc macrocycle, the second peak is due to multilayers of pyridine and pyridine absorbed on

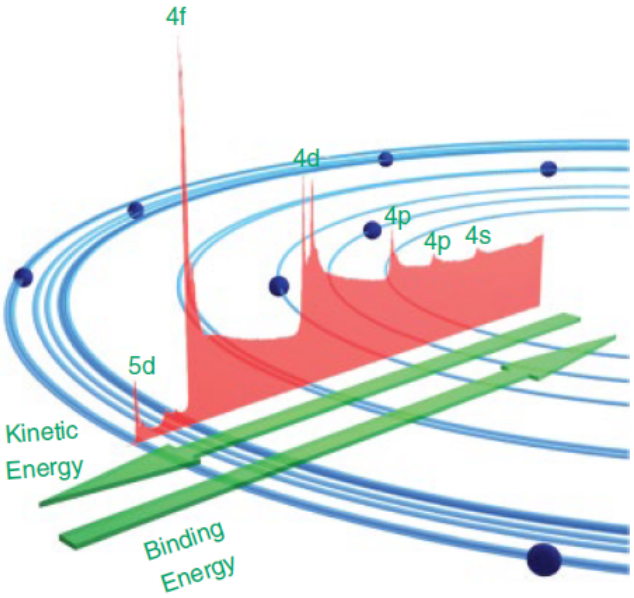

Figure 52: Photoelectron spectrum of lead overlayed with its electronic structure showing the photoelectron lines of each orbital.[175]

other sites (not Fe), and the third peak arises from the coordination bond between Fe and N (Figure 53a). Not only is there change in the N 1s region, the coupling to the iron ion will also affect the photoemission in the Fe 2p region. As we can see from their results (Figure 53b, the peak begins off broad with a full width at half-maximum of 3.7 eV and eventually narrows down to less than half of this. The authors state that this is the result of ligand field splitting and indicates partial decoupling of the iron from the gold.

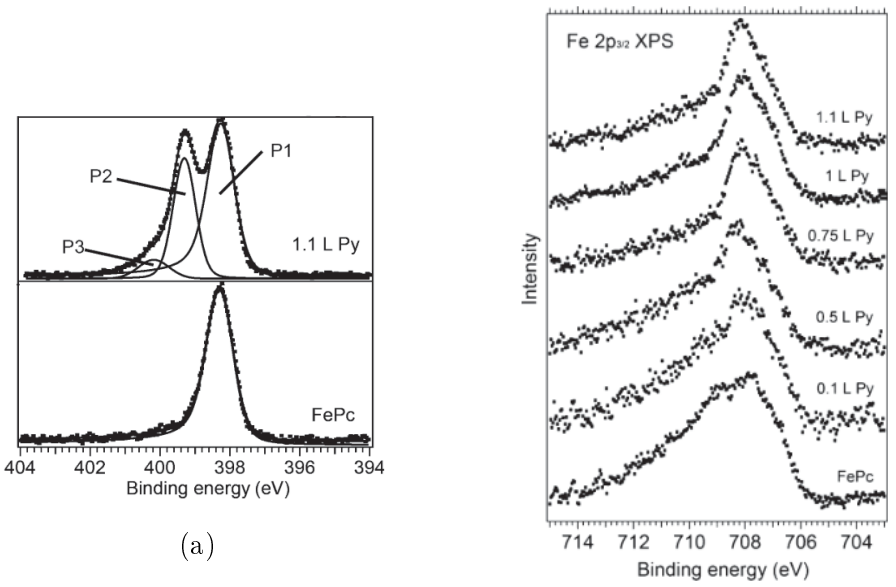

(a)

(b)

Figure 53: XPS results taken from [128] of pyridine adsorbed onto FePc in the (a) N 1s region and the (b) Fe 2p region.

Chapter 5

Assembly, Structure and Electrical Properties of 1,1'-Dialkynylferrocenes

This chapter investigates a variety of ferrocene molecules using nitrogen and sulphur based anchor groups with varying binding strength. In the first section, the assembly, structure and thermoelectric properties of 1,1'-dialkynylferrocene where we identify and characterise an unusual hairpin structure. The second part of this chapter will investigate the transport properties of ferrocene-(ethynyl-phenyl)thioacetates.

5.1 Introduction

Ferrocene exhibits several interesting properties, such as high stability, well-defined redox chemistry, and can be functionalised using a wide variety of techniques.[184, 185, 186] For these reasons, ferrocenes have made their way as a building block into works involving single molecules and electronic devices.[187, 188, 189, 190] In the design of molecular wires, ferrocene insertion (and more widely, the insertion of metal centres) have been shown to increase molecular conductance.[191, 192, 193] In addition, recent studies of the 1,1'-dialkynylferrocene motif have demonstrated that by controlling the rotation around the iron-cyclopentadienyl axis, through the use of a mechanical modulation, the conductance of a ferrocene can be switched be-

tween multiple states, as a function of the angle that separates the two alkynyl substituents.[188] This indicates that the inclusion of ferrocene into highly-conjugated architecture offers an attractive route toward optimising and increasing the functionality of organic molecular wires.[194]

With a view to translating these properties to the macroscale, here we study the electronic properties of self-assembled monolayers (SAMs) of ferrocene-based molecules, which could be translated to a device architecture in a relatively facile manner.[97, 195] To date, the majority of highly-conjugated ferrocenyl SAMs have utilised ferrocene as a terminal group, ignoring the potential benefits of incorporating ferrocene into the backbone of molecular wire.[196, 197, 198, 199] In contrast, the present study focuses on 1,1'-dialkynyl ferrocenes, which possess a relatively rigid 'hinge-like' structure, where the two substituents can independently rotate around a central ferrocenyl node. This offers the possibility of exploring a variety of distinct conformations which could be used to control the electronic properties of their assembled materials. All molecules studied in this section were synthesised by Luke A. Wilkinson and Troy L. R. Bennett. Please refer to the paper cited for detailed synthesis.[200] The modelling and simulation was carried out by Iain M. Grace.

5.2 Part 1: Pyridyl Dialkynylferrocenes 'Hinges'

In the following study, we selected a range of 1,1'-dialkynylferrocene molecules, 1-5 (Figure 54) containing a variety of pyridyl based anchor groups. Where previous single-molecule studies have shown that an 'open' conformation (where the alkynes point in different directions) is achievable, here we have shown that the 'hairpin' conformation (where the alkynes point in the same direction) is generally favoured.[188, 16] Further to this we examined the thermoelectric features of this 'hairpin' structure and identified an interesting feature whereby only one, of a possible two, anchor groups binds to a surface, while the alignment of the second, unbound anchor group, also subtly controls the electronic properties of the materials.

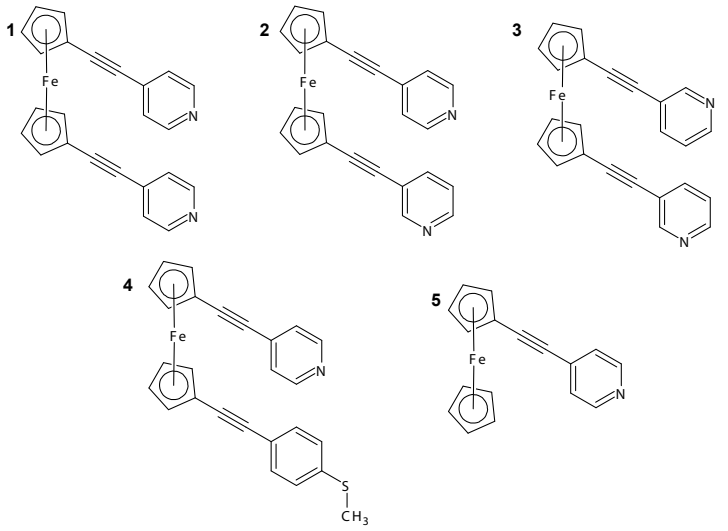

Figure 54: Chemical structures of the ferrocene molecules investigated in this study. Notation will be as follows: 1 - FcNN, 2 - FcN3N, 3 - Fc3N3N, 4 - FcNS, 5 - FcN.

5.2.1 Ferrocene SAM Growth and Formation

Self-assembled monolayers (SAMs) of molecules 1-5 were grown on freshly prepared, template stripped Au surfaces by the method described above, in Section 4.0.3. All molecules were dissolved in toluene with 1 mM concentration, followed by 15 minutes of ultrasonication. The solutions were bubbled with nitrogen for 15 minutes for deoxygenation. The Au^{TS} was then immersed into each solution, without any further treatment, for SAMs growth. The SAMs growing process was conducted under a nitrogen atmosphere for 48 hours. The substrate, after SAMs growth, was rinsed ten times with toluene, ethanol and isopropanol, in sequence, to wash off physisorbed molecules. Finally, the SAMs were then incubated in a vacuum chamber for 2 hours, to allow for solvent evaporation. The following samples were then characterised by atomic force microscopy (AFM).

Unlike the other analytes, FcN3N did not form good-quality SAMs, exhibiting pin-holes in the film that affected the conductance measured with AFM. This is likely attributed to the competitive binding of the different anchor groups contained within this molecule. The other systems all formed high-quality SAMs however.

The thickness of these SAMs was determined by a nano-scratching technique (where the height distributions are shown in Figure 56). Molecules 1 (FcNN), 4 (FcNS) and 5 (FcN) all appear to have similar thicknesses with molecule 3 (Fc3N3N) forming

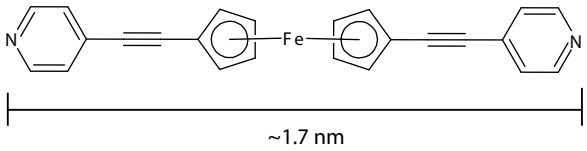

Figure 55: Length of an outstretched FcNN molecule.

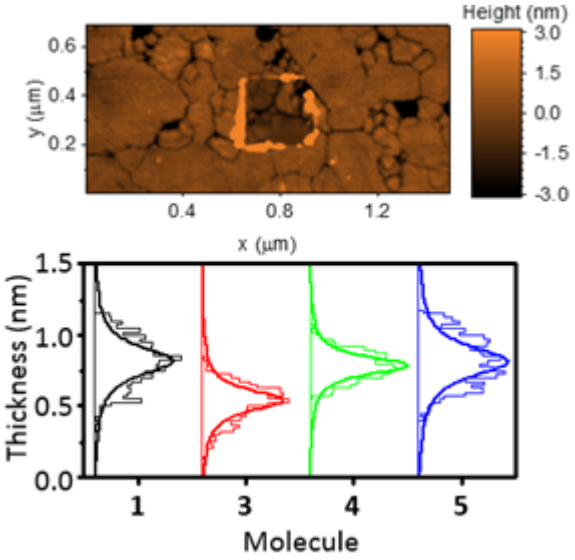

Figure 56: Courtesy of Xintai Wang. Topography of a SAM of FcNN after nano-scratching (top), and thickness distributions of SAMs of FcNN, Fc3N3N, FcNS and FcN obtained from nano-scratching (bottom).

the thinnest monolayer. SAM of FcNN and FcNS possess similar heights at 0.81 and 0.79 nm, respectively. This highly indicates the molecule forms a packed layer in a folded 'hairpin' conformation as Lindner et al. calculated a fully stretched out FcNN molecule to be approximately 1.7 nm (Figure 55).[201, 202] To further support this conformation, the thickness of FcN lies around half of the length of a fully stretched-out FcNN molecule at 0.82 nm. The thickness of FcNN and FcNS would reach over the thickness of FcN if they were in an outstretched 'open' conformation. Fc3N3N formed a thinner SAM, with a thickness of 0.52 nm. This indicates another 'hairpin' geometry, however, with this large decrease, we can assume the binding orientation differs from FcNN, FcNS and FcN. This is likely due to FcNN, FcNS and FcN being able to adopt a largely perpendicular orientation, whereas Fc3N3N would present a tilted geometry, resulting from the meta-positioning of the nitrogen atoms contained within its terminal pyridyl rings.

This is in line with the DFT calculations (Figure 57), where the optimum geometry of

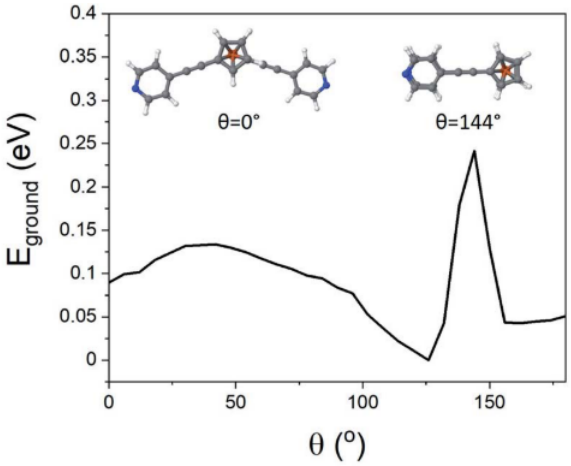

Figure 57: DFT calculations of FcNN showing the angle of internal rotation (θ) *vs* the ground state energy of the molecule. Courtesy of Iain M. Grace.

each of the molecules was calculated. The ground state energy of the molecules was then calculated as a function of angle θ, for FcNN and it was found that the minimum energy occurred at $\theta = 126°$, with the molecule held in a 'hairpin' configuration with the arms slightly displaced, consistent with π-π type interactions between the two alkynyl substituents.

AFM imaging was employed to determine the average roughness of SAMs FcNN, Fc3N3N, FcNS and FcN (across several spots of the sample). The roughness was in the range of 0.15-0.30 nm, and this value was similar to the underlying TS gold substrates (0.10 - 0.20 nm), which confirms the SAMs uniformity. To better elucidate these results, Figure 56 shows topography of FcNN, after nano-scratching, as well as thickness distributions of SAMs FcNN, Fc3N3N, FcNS and FcN, garnered from the nano-scratching analysis.

5.2.2 X-ray Photoelectron Spectroscopy

To better understand the results above, I then carried out a detailed study of the chemical binding of the ferrocenyl SAMs using X-ray photoelectron spectroscopy (XPS). Although the poor uniformity of FcN3N prevented thermoelectric and conductance measurements with the AFM, the sample could still be studied with XPS by measuring over a large spot size (350 µm), enabling us to average over the poor nanoscale ordering of FcN3N.

Figure 58(a) and (b) show spectra of the N 1s region for SAMs of FcNN and FcN3N,

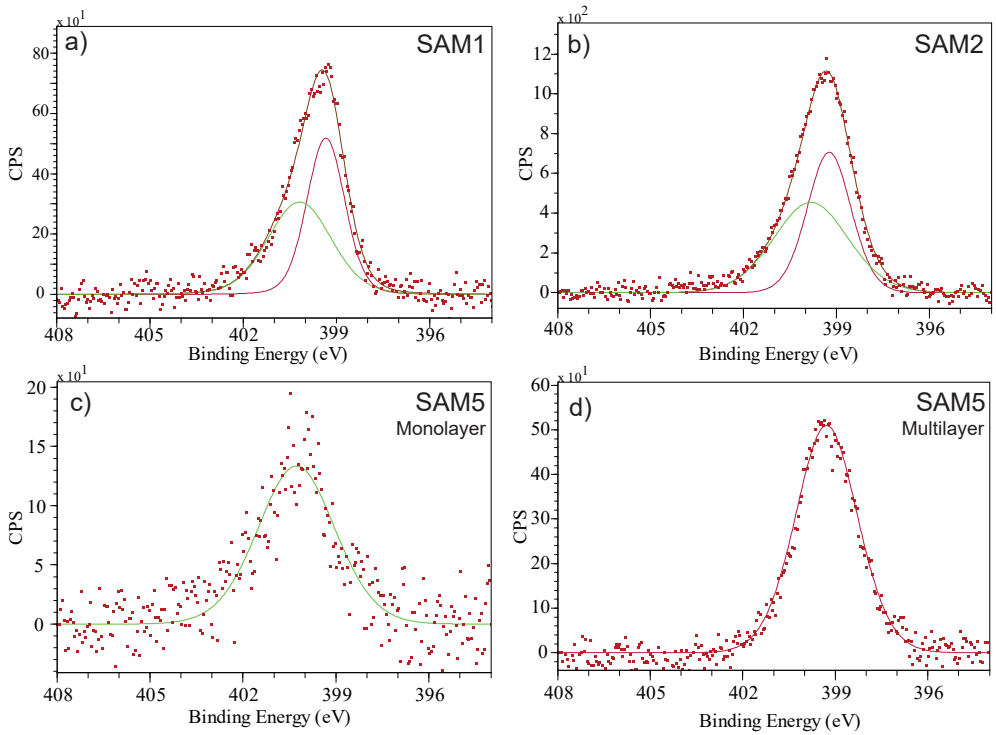

Figure 58: XPS data of the N1s region for (a) FcNN, (b) FcN3N, (c) Monolayer of FcN and (d) Multilayer of FcN to show the corresponding bound and unbound nitrogen peaks.

respectively. In each case, clear features are observed that arise from the nitrogen atoms present in the pyridine anchor groups. For the SAM of FcNN, a fitting analysis revealed two distinct peaks located at 400.2 eV and 399.3 eV respectively, with a ratio of peak areas close to 1:1. The 399.3 eV peak can be attributed to an unbound pyridine with a deprotonated nitrogen.[83, 203] The peak at 400.2 eV has been previously attributed to the pyridine group binding to the gold surface.[204] To confirm this assignment we carried out XPS on monolayer and multilayer SAMs of FcN, in which the pyridine groups should be either fully bound or unbound, respectively. The results, shown in Figure 58(c) and (d), confirm the assignments above, with the monolayer of SAM5 exhibiting a single bound peak at 400.2 eV, and the multilayer SAM of FcN a dominant unbound peak at 399.3 eV.

The fitting analysis for FcN3N (Figure 58(b)), results in the same near 1:1 ratio of bound at 400.1 eV and unbound nitrogen at 399.4 eV. The near 1:1 ratio and consistency between SAMs FcNN and FcN3N strongly suggested that only one of a possible two anchor groups chemically binds to the surface in each case. It is observed

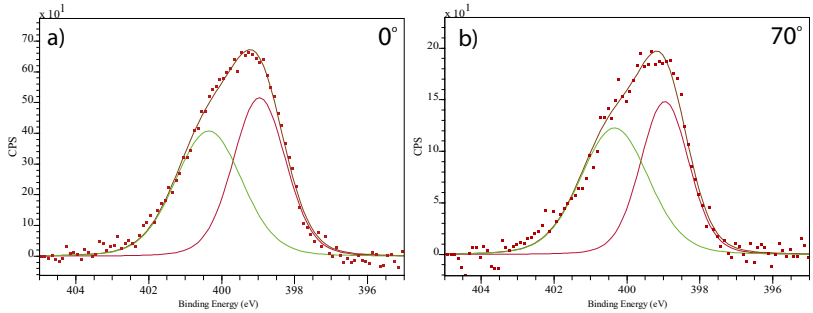

Figure 59: ARXPS spectra in the N 1s region for FcNN at (a) 0°and (b) 70°. The green curve represents bound nitrogen atoms and red represents the unbound.

that the bound peaks are broader than the unbound peaks which we attribute to the nitrogen binding to multiple adsorption sites of the gold surface. In both cases, the full-width half maximum of the bound peak is approximately 1 eV wider than the unbound peak.

To gain greater insight into the location of the pyridine groups within the molecular film, we performed angle resolved XPS (ARXPS) on FcNN. In order to reduce any possibility of water contamination, which would introduce additional peaks in the N 1s region, the film was annealed under UHV conditions at 160°C for 12 hours prior to the ARXPS measurements, resulting in a slight shift of the bound and unbound peaks to 400.4 eV and 399.0 eV, respectively.[205] The subsequent ARXPS data collected at angles of emission of 0°and 70°are shown in Figure 59. We found that the N 1s peak at both angles could be fitted with near identical peak components, with no evidence to suggest any reduction in peak area upon rotating the sample. The similarity in peak area therefore suggested that the two nitrogen species were located at similar heights (within surface roughness of ∼0.3 nm), supporting the formation of a 'hairpin' geometry. In contrast, if the upright configuration were present instead, a Beer-Lambert approximation estimates that the attenuation of the bound nitrogen signal would be >5, resulting in substantial reduction in the bound N 1s peak. This estimate assumes an inelastic mean free path of ∼1.5 nm and a nitrogen depth of ∼2.0 nm.

5.2.3 Conductance and Thermoelectric Properties

To further examine the effects of our different anchor group configurations the thermoelectric properties of the SAMs were probed. First, their electron transport properties were determined by conductive AFM (cAFM) (method described in detail in Section 4.1.3). The probe was fixed at a single point using a constant force of 2 nN. This is high enough to penetrate through the water layer and low enough to preserve the molecular layer. A triangular AC bias voltage is then applied between the probe and the sample to record the current signal. Standard Pt Budget Sensor Multi75-G probes with a radius of 25 nm were used for investigation. The number of molecules under the probe was estimated from the contact area between the probe and sample surface using the RKJ model[206, 207]:

$$r = (F \times R \times \frac{1}{Y})^{\frac{1}{3}} \tag{5.1}$$

$$\frac{1}{Y} = \frac{3}{4} \times \left(\frac{1 - v_1^2}{E_1} + \frac{1 - v_2^2}{E_2} \right) \tag{5.2}$$

Here r represents the contact radius, F is the loading force, R is the radius of the probe, which was estimated to be 25 nm by SEM imaging v_1 and v_2 is the Poisson ratio of the material and E_1 and E_2 are the Young's Modulus of the probe and sample monolayer, respectively. The Young's Modulus was determined by PeakForce AFM and it resulted around 2 GPa for the SAMs. Additional parameters were taken from studies working on similar systems.

The statistics of the I(V) curves and the conductance histograms of FcNN, Fc3N3N, FcNS and FcN were taken by Xintai Wang and are shown in Figure 60. The panels on the left show the I(V) curves of SAMs FcNN, Fc3N3N, FcNS and FcN scaled down to a single molecule. The white curve shows the average and displays typical semi-conductor type characteristics.

The conductance at zero-bias of Fc3N3N appears to be at approximately $\sim 10\times^{-8}$ and is considerably higher than the conductance measured of the others as the minimum of the curve can be seen to be lower than $\sim 10\times^{-8}$. To compare the

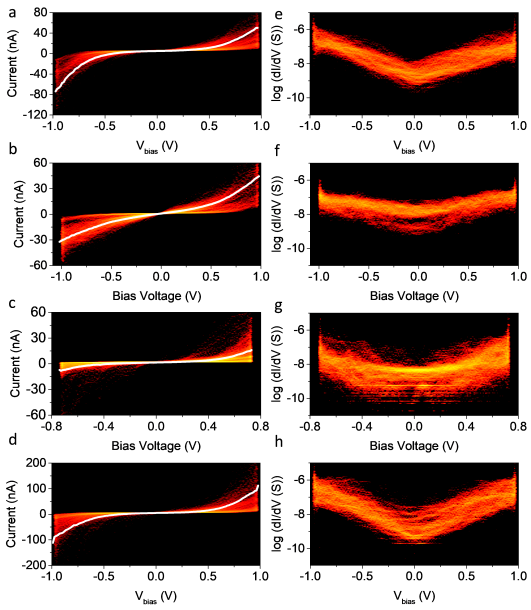

Figure 60: (a-d) Statistics of I(V) curves obtained from SAMs FcNN, Fc3N3N, FcNS and FcN (left panels). (e-h) Statistics of conductance obtained from SAMs FcNN, Fc3N3N, FcNS and FcN (right panels). Data taken by Xintai Wang.

conductance values, the $\log(G/G_0)$ was calculated and found to be -4.6 for FcNN, -3.9 for Fc3N3N, -4.5 for FcNS and -4.7 for FcN. As the conductance of FcNN, FcNS and FcN are very similar to one another, this suggests that the presence of an additional alkyne poses little influence on the conductive behaviour of these molecules. Although sulphur typically shows higher conductance, replacing a nitrogen group with a sulphur counterpart causes no significant changes. This could be due to the thickness of the SAMs layers which were ~ 0.8 nm. The conductance of Fc3N3N is much larger than those of the other analogues (an increase of 15%), which is presumably a result of the thinner SAM, and by extension, the shorter distance between the probe and the underlying metal substrate.

The thermopower of these SAMs was also investigated using a Peltier stage under the sample to create a temperature difference, ΔT, between the sample and the probe, further details were described in Chapter 4. The results are displayed in Figure 61.

FcN, with a singular arm (nitrogen in the para position), showed a thermopower of $-9.0 \pm 3.1\ \mu V\ K^{-1}$. Unlike the conductance, the effect of adding an extra alkyne group could enhance or hinder the thermopower generated depending on the anchor groups

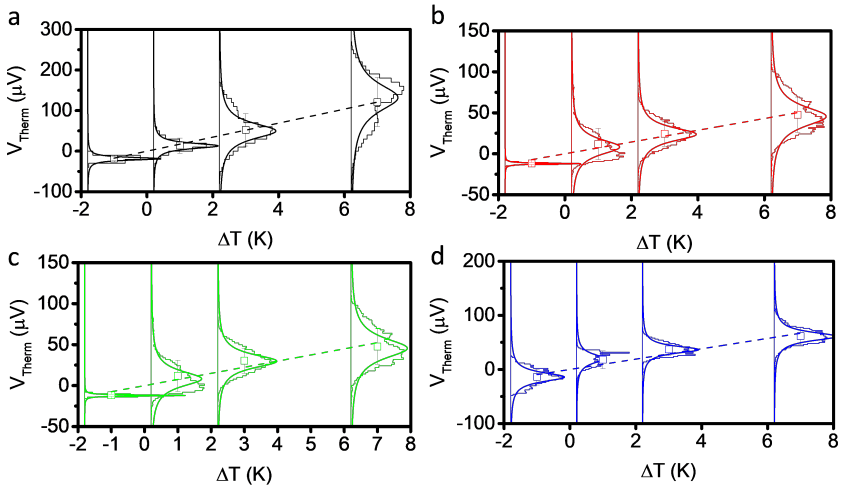

Figure 61: (a-d) Histogram plots of measured thermovoltage at a range of temperature differences for SAMs FcNN, Fc3N3N, FcNS and FcN. Data courtesy of Xintai Wang.

of the alkyne. Here, molecule 1 has the addition of an identical alkyne arm with a pyridyl anchor in the para position and the thermopower is greatly enhanced by ∼82%, giving a Seebeck coefficient of -16.4 ± 4.1 μV K^{-1}. On the other hand, if the additional alkyne group had a sulphur anchor group, molecule 4, the thermopower increases less drastically by ∼6%, giving a Seebeck coefficient of -9.6± 2.2 μV K^{-1} μV K^{-1}. However, switching the sulphur group to a pyridyl group is advantageous. This suggests that the unbound alkyne of this system is acting to tune the energy of the LUMO, with respect to the Fermi-energy of the electrode.

In contrast to the conductance results, Fc3N3N produced the smallest thermopower. With both nitrogen atoms in the meta position, the Seebeck coefficient obtained was -7.4 ± 3.5 μV K^{-1}. The large difference in Seebeck between Fc3N3N and FcNN can be accounted for by the destructive interference occurring at the meta positioning on the phenyl ring. By altering the positions of the nitrogen atoms, an enhancement of 121.6% can be achieved.

All of the SAMs possessed negative Seebeck coefficients, which suggests LUMO dominated electron transport through these molecules, as has often been reported for systems with pyridine anchors connecting to a metal surface.[208, 209, 90] However, this is not conclusive as thioethers have previously been shown to give both positive and negative Seebeck coefficients.[208, 48, 210, 104]

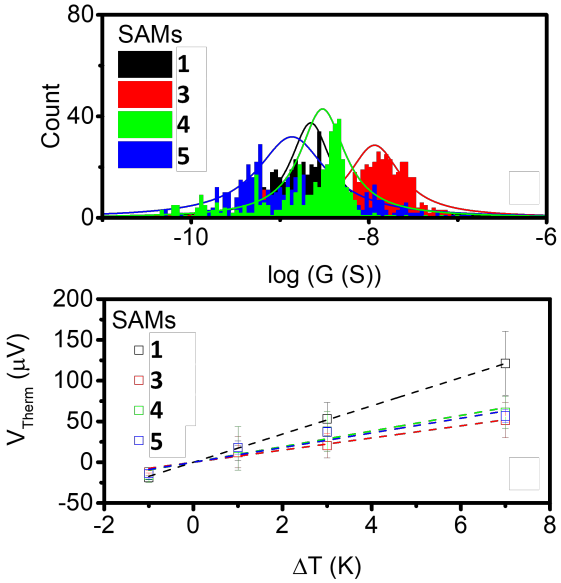

Figure 62: Conductance distribution (top) and plots of thermal voltage vs ΔT (bottom). Data courtesy of Xintai Wang.

Table 5.1: Structural and thermoelectrical properties of SAMs FcNN, Fc3N3N, FcNS and FcN, including the conductance ratios (G/G_0), Seebeck coefficients (S) and power factors (PF, which is equal to G $\times S^2$)

SAMs	**Roughness** (nm)	**Thickness** (nm)	**log(G/G_0)**	**S** (μV/K)	**Std** (μV/K)	**PF** (a(W/K^2))
FcNN	0.09	0.81	-4.6	-16.4	4.1	0.52
Fc3N3N	0.07	0.52	-3.9	-7.4	3.5	0.53
FcNS	0.10	0.79	-4.5	-9.6	2.2	0.22
FcN	0.14	0.82	-4.7	-9.0	3.1	0.12

Finally, the power-factors (PF, which is equal to $G \times S^2$) were considered. The large Seebeck coefficient of FcNN and the increase in conductance of Fc3N3N, granted the power factor of these two SAMs to be very similar at 0.52 and 0.53 a(W/K^2), respectively. The power factor observed in SAMs FcNS and FcN were less than half of that of FcNN and Fc3N3N, calculated to be 0.22 and 0.12 a(W/K^2). Table 5.1 summarises all the key findings in this part of the study.

The 'hairpin' conformations were found to display interesting structural and electronic features. XPS analysis revealed that although both anchor groups pointed towards the metal surface, only one of these was bound, with the second anchor group being held in close proximity. It is clear that the nature of the anchor groups that bind to the gold controls both the structure and electronic properties of these

systems (as seen in the comparison of FcNN and Fc3N3N). However, it appears that the 'unbound' anchors also influence their electronic properties. First, the inclusion of the peripheral alkyne substituent acted to shift the energy of the LUMO resonance with respect to the Fermi energy of the electrode, leading to increased Seebeck coefficients. Secondly, our calculations suggested that controlling the alignment of the unbound alkyne substituent may offer a route toward controlling the thermoelectric properties of these systems.

5.3 Part 2: Dialkynylferrocene Thioacetates

In the second part of this section, 1,1'-dialkynlferrocenes were investigated bearing mainly thioacetate groups as opposed to the pyridyl groups found in Part 1, are shown in Figure 63. We examined the surface of the SAMs with AFM and XPS and characterised the electronic properties with C-AFM.

As we discovered in Section 5.2, one anchor group binds to the surface, the other anchor group also has an effect on the electronic and thermoelectric properties of the SAMs. We can determine if this is also the case by switching out the anchor groups from pyridyl to thiol. Sulphur groups form stronger covalent bonding with metallic electrodes, the purpose of experimenting with these groups is to observe the effects of the stronger covalent effects on its electrical and thermoelectrical properties. In addition to this, it would be interesting to see the effects on the packing conformation we change the anchor groups. Molecule 2 has been investigated to observe the effects of an additional ferrocene unit on the electrical properties. Moving the nitrogen atom from the para position to the meta position should affect the electrical transport properties due to QI effects.

5.3.1 SAMs Growth and Formation

SAM formation followed the same procedure as Section 5.2.1. The results are shown in Figure 64. $Fc(SAc)_2$, Fc_2SAc_2 and FcNSAc formed uniform and well-ordered SAMs, however, Fc3NSAc had the tendency to agglomerate if left for long periods of times which would affect nano-scratching and conductance measurements. The topography of Fc3NSAc can be seen in Figure 65, the uniformity is lost with islands

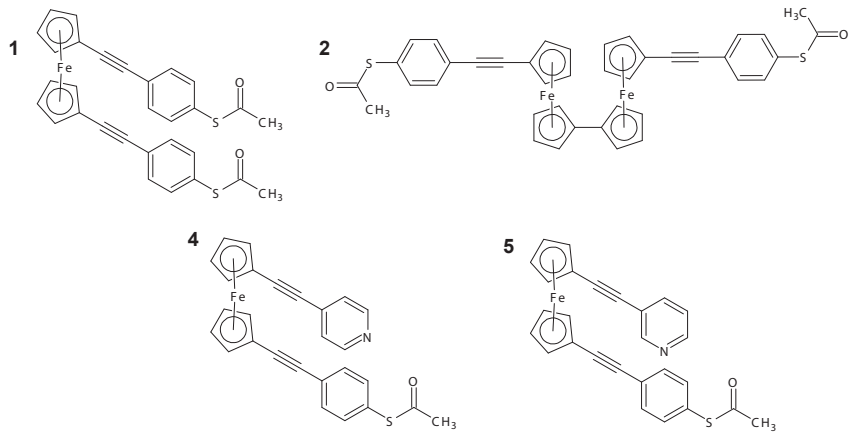

Figure 63: Chemical structure of the ferrocenes studied in Part 2. 1 - $Fc(SAc)_2$, 2 - Fc_2SAc_2, 4 - FcNSAc and 5 - Fc3NSAc.

of molecules reaching over 30 nm tall 24 hours after preparation.

Nano-scratching revealed the thickness of the thioacetate ferrocenes to be larger than that of the pyridyl ferrocenes. SAMs of $Fc(SAc)_2$ was found to be 1.58 nm, Fc_2SAc_2 had a height of 2.70 nm, FcNSAc was 2.38 nm thick and Fc3NSAc had a thickness of 2.31 nm. In contrast to the results we found in Part 1, the formation of SAMs appears to have an 'open' configuration which is in line with the literature on single molecular experiments.[188, 16] Fc_2SAc_2 is found to be the thickest which is to be expected due to the additional ferrocene unit. FcNSAc and Fc3NSAc show similar heights indicating similar tilt angles and similar degrees of rotation about the ferrocene unit, independent of the positioning from the nitrogen atom.

$Fc(SAc)_2$ formed thinner SAMs which could likely be due to the tilt of the sulphur-gold bond or perhaps due to a larger angle of internal rotation. To fully understand the conformational features of these systems, theoretical calculations need to be performed for support.

5.3.2 X-ray Photoelectron Spectroscopy

The powder form and SAMs of $Fc(SAc)_2$, FcNSAc and Fc3NSAc were examined by XPS and calibrated to the C-C component of the C 1s peak at 284.8 eV. Figure 67 shows the photoemissions for $Fc(SAc)_2$ in the powder form and deposited onto gold in the S 2p region. The sulphur peaks display doublets corresponding to the S $2p_{3/2}$ and $2p_{1/2}$ and are Gaussian-Lorentzian fitted with a splitting of 1.2 eV.

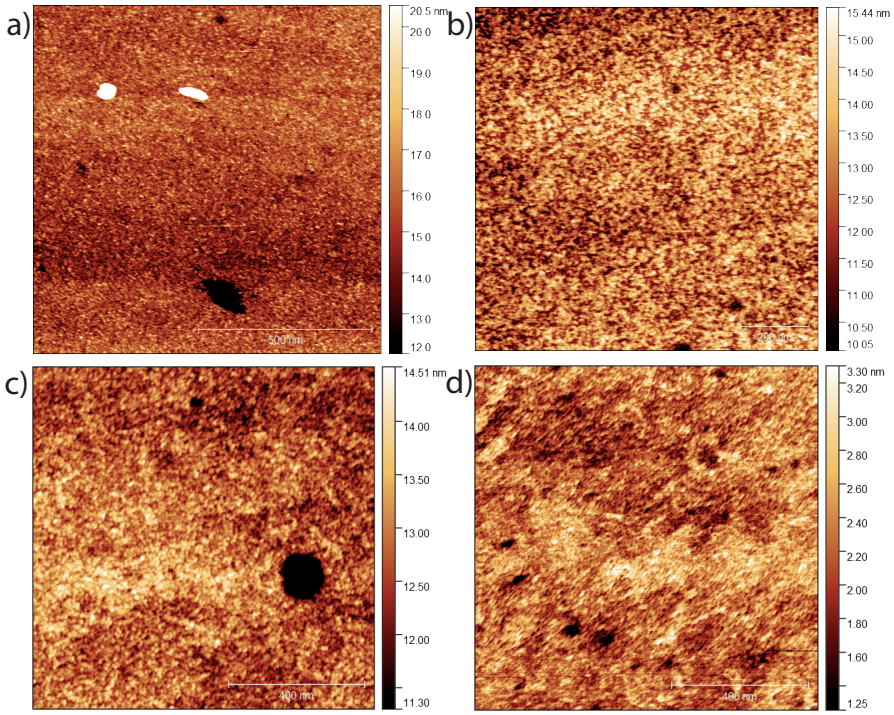

Figure 64: AFM topography scans of (a) SAM1 - $Fc(SAc)_2$ (b) SAM2 - Fc_2SAc_2 (c) SAM4 - FcNSAc and (d) SAM5 - Fc3NSAc.

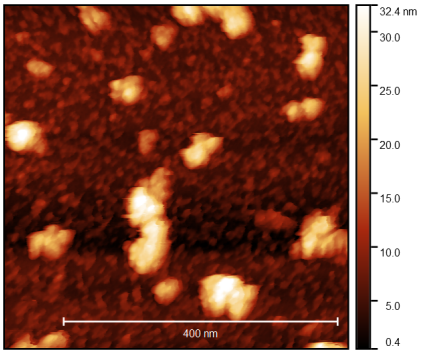

Figure 65: Topography of Fc3NSAc showing the tendency to cluster after long periods of time.

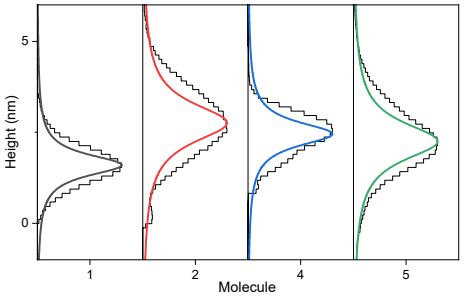

Figure 66: Thickness distributions of SAM1 - $Fc(SAc)_2$, SAM2 - Fc_2SAc_2, SAM4 - FcNSAc and SAM5 - Fc3NSAc.

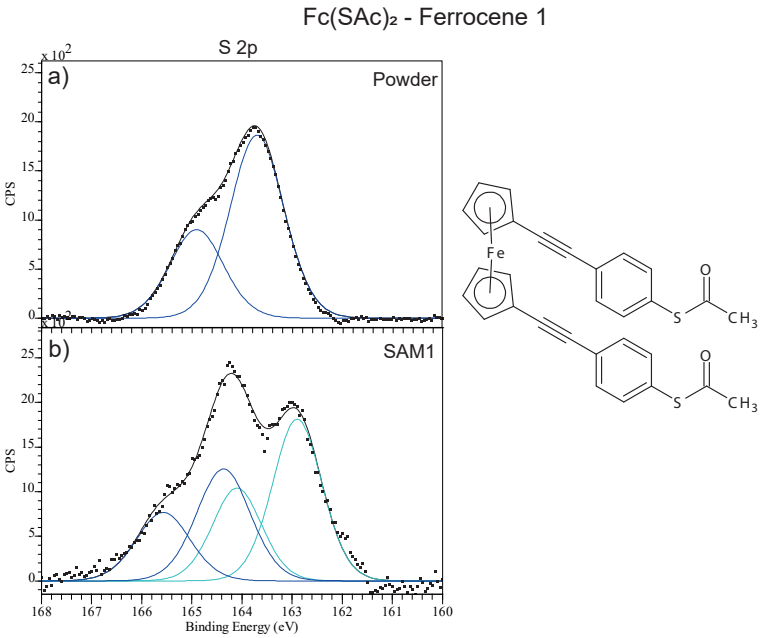

Figure 67: XPS spectra shown of $Fc(SAc)_2$ in the S 2p region as the (a) powder form and (b) as a SAMs. The navy curves show the unbound sulphur peak whereas the light blue indicates bound sulphur.

The area ratios are assigned a 2:1 ratio, indicating 4 electrons in the former and 2 in the latter. The first set of doublets of $Fc(SAc)_2$ in the powder form arises at 163.7 eV and 164.9 eV. This is due to unbound sulphur, as expected from the pure powder.[110, 103] Evidence of binding to the gold substrate can be seen in the SAM1 spectra where an additional doublet peak at 162.9 eV and 164.1 eV appears.[211, 212, 183] The original unbound sulphur peak shifts slightly to 164.4 eV and 165.5 eV and can be explained by the bonding of the atoms to the gold sites. The area ratio between the unbound and the bound sulphur is 1:1.1 which lies very close to a 1:1 ratio indicating monolayer formation on the gold surface whereby equal amounts of sulphur are attached to the surface compared to the amount not adsorbed onto the surface.

FcNSAc underwent the same characterisation and is shown in Figure 68. The powder produced peaks at 163.43 and 164.63 eV, which is similar to results from the powder of $Fc(SAc)_2$. The SAMs of FcNSAc produced an unbound doublet at similar values to the powder form and a bound doublet arises at 161.9 and 163.1 eV. The area ratio between unbound and bound sulphur again lies very close to 1:1.

Considering the N 1s region, the powder form gives a single peak at 398.83 eV show-

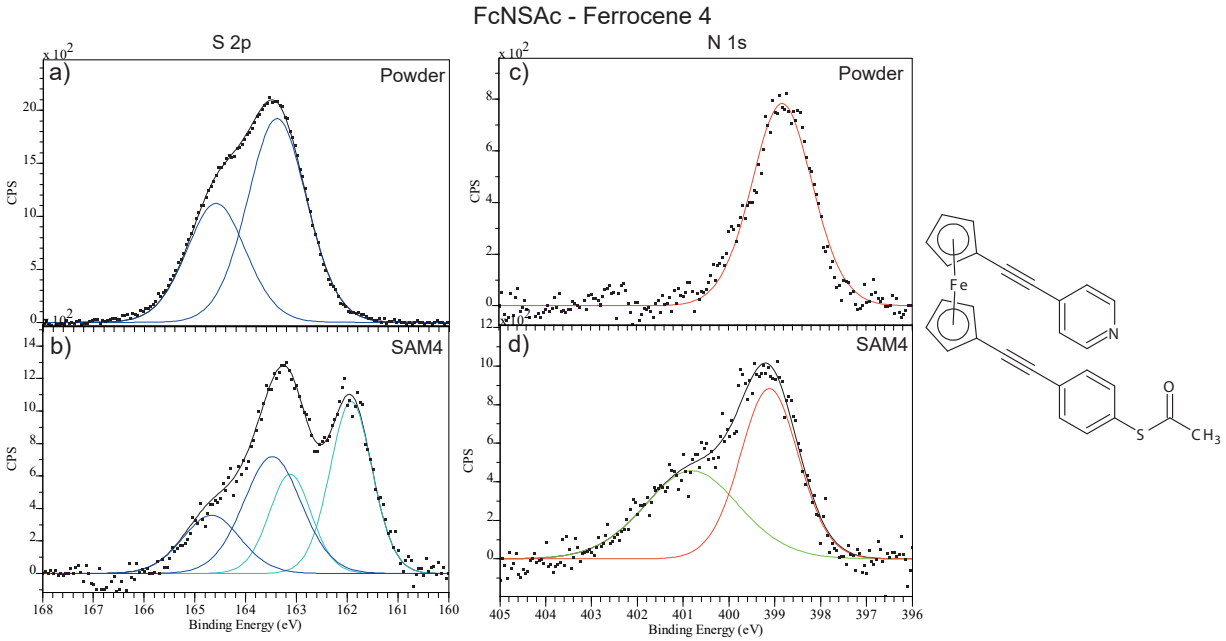

Figure 68: XPS spectra shown of the FcNSAc as a powder (a, c) and as a SAMs (b, d) in the S 2p and N 1s region, respectively.

ing a single chemical environment for the nitrogen as expected from the chemical structure of FcNSAc. This would be assigned as the unbound nitrogen peak. As we deposit the molecule onto the gold surface, the unbound peak is found at 399.1 eV and a shoulder arises in the spectra at 400.81 eV. The latter photoemission is due to the adsorption of nitrogen to the gold surface. The area ratio of bound and unbound nitrogen is also close to 1:1. The evidence of both nitrogen and sulphur producing signs of adsorbing onto the substrate shows the formation of a mixed layer.

Similarly, as found for Fc3NSAc (Figure 69), the powder showed sulphur doublets at 163.33 eV. After deposition, the bound sulphur doublet arose at 162.0 and 163.2 eV. The area ratio between these was 1:1.3 indicating a higher presence of S-Au bonds than 'free' sulphur atoms. The powder of the nitrogen emitted a single peak at 398.86 eV, again, representing the unbound nitrogen. As we deposit onto the surface, the bound nitrogen peak appears at 401.41 eV. The area ratio of this peak is ∼1:1.9 bound to unbound, showing that the amount of unbound nitrogen groups is approximately twice as much as the bound. Taking into consideration both area ratios of nitrogen and sulphur, it can be deduced that this mixed layer consists of a higher amount of sulphur attached to the gold substrate as opposed to FcNSAc. This is due to the nitrogen being in the meta-position of the phenyl ring which

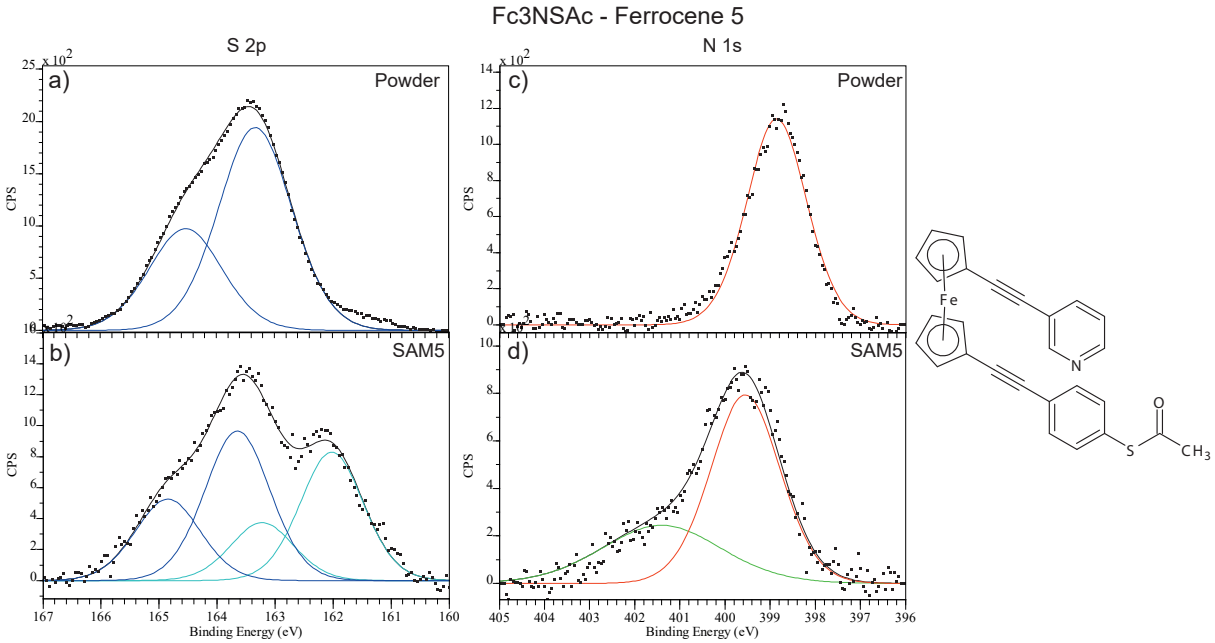

Figure 69: XPS spectra shown of the Fc3NSAc as a powder (a, c) and as a SAMs (b, d) in the S 2p and N 1s region, respectively.

cannot access the substrate as easily.

Fe2p region of $Fc(SAc)_2$, FcNSAc and Fc3NSAc

Repeat measurements were taken of the XPS spectra in the Fe 2p region for $Fc(SAc)_2$, FcNSAc and Fc3NSAc shown in Figure 70. The pure powder forms are shown in Figure 70(a) and display two distinct peaks at 707.98 eV and 720.69 eV arising from the two different spin states of iron, $2p_{3/2}$ and $2p_{1/2}$, respectively.[213] These are associated with diamagnetic Fe^{II}, showing the neutral state of ferrocenes.[214] These values are aligned with a monolayer deposition. As the films become thicker and more bulklike the Fe $2p_{3/2}$ appears at 708.1 eV (as evident from the binding energy of the powders).[215]

A small shoulder is visible to the left of the sharp peaks found for the powder of $Fc(SAc)_2$ and becomes more prominent in all ferrocenes after self-assembly to gold (Figure 70(b)). These peaks are found at ~711 and ~723 eV. These broader peaks are attributed to the higher oxidation state of Fe, Fe^{III} $2p_{3/2}$ and $2p_{1/2}$, respectively.[216] The full-width half-maximum of the Fe^{III} peaks were approximately four times as wide as those of Fe^{II}. In addition to the broadness, the peaks are also asymmetrical. Both these features indicate the presence of paramagnetic metal

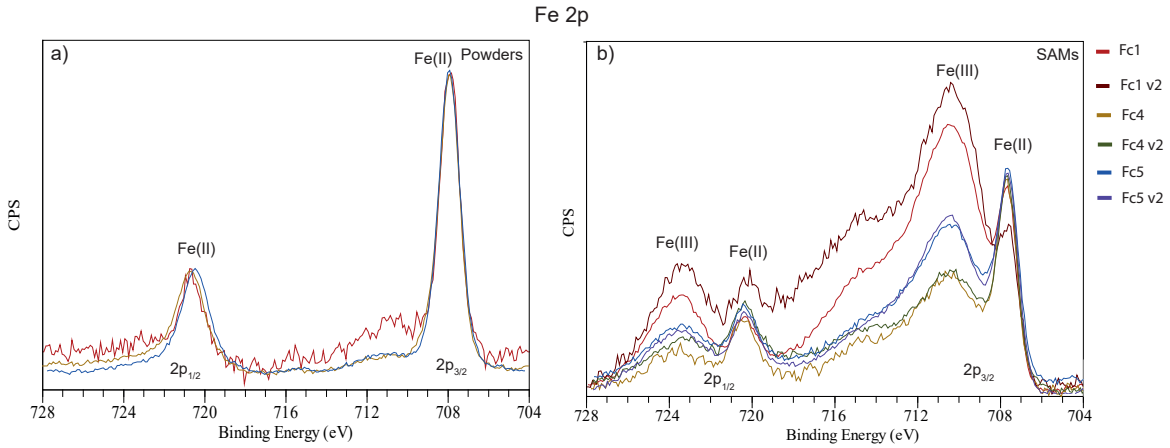

Figure 70: XPS spectra shown of the ferrocene molecules in the Fe 2p region. (a) Shows the powder forms of molecules 1, 4 and 5. (b) SAMs and the repeat measurements of molecules 1, 4 and 5. 1 - $Fc(SAc)_2$, 4 - FcNSAc and 5 - Fc3NSAc.

compounds.[217, 218] From the XPS results shown in this section, $Fc(SAc)_2$ shows the most Fe^{III} character, whereas FcNSAc has the least amount of Fe^{III}. Possible reasons for this could be due to the formation of the monolayers or possibly the binding between the surface and the anchor groups. However, in order to fully understand these results, further characterisation such as theoretical calculations needs to be carried out.

5.3.3 I-V Characteristics and Electrical Transport Characterisation

After identifying these differences with XPS, conductive AFM was used here to observe any changes in molecular conductance of SAMs $Fc(SAc)_2$, Fc_2SAc_2, FcNSAc and Fc3NSAc (Figure 71). Figure 71(a-d) shows statistical two-dimensional I(V) curves of the four molecules scaled down from approximately 416 molecules (using eq. 6.2) to a single molecule. All four graphs displayed typical semiconductor characteristics (the red line shows the curves' average). Fc_2SAc_2 appears to produce a fairly flat average which indicates low conductance, however, to observe this more clearly, differential conductance (dI/dV) histograms are plotted in Figure 71(e-h).

The total electrical conductance at zero bias for SAMs $Fc(SAc)_2$, Fc_2SAc_2, FcNSAc and Fc3NSAc4 was found to be 1.14×10^{-10} S, 1.52×10^{-12} S, 4.63×10^{-11} and $4.2 \times$

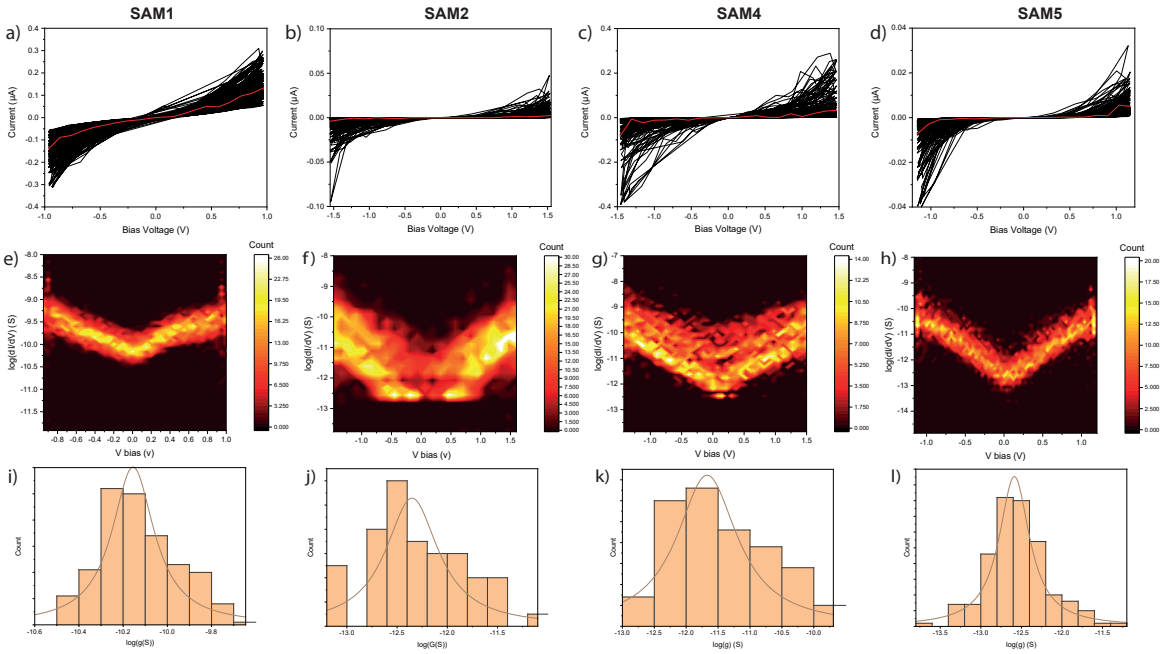

Figure 71: (a-d) Statistical I(V) curves of SAMs $Fc(SAc)_2$, Fc_2SAc_2, FcNSAc and Fc3NSAc, (e-h) electrical conductance counter maps corresponding to SAMs $Fc(SAc)_2$, Fc_2SAc_2, FcNSAc and Fc3NSAc, and (i-l) show the conductance distributions found for SAMs $Fc(SAc)_2$, Fc_2SAc_2, FcNSAc and Fc3NSAc.

10^{-13} S, respectively. From the differential conductance histograms, the conductance distributions at near zero voltage bias can be plotted. This is shown in Figure 71(i-l) and from this the $\log(G/G_0)$ of each SAM can be determined. As we have previously established molecules containing sulphur groups provide the highest conductance when compared with nitrogen and oxygen moieties. Therefore, it is expected that $Fc(SAc)_2$ gives the highest log conductance value at -6.3. Fc_2SAc_2 contains the same anchor groups but has a lower conductance of -8.19. This could be attributed to the increase in length due to the additional ferrocene unit in Fc_2SAc_2. This is reflected in the difference in thickness of the two samples, where $Fc(SAc)_2$ was found to be 1.58 nm and Fc_2SAc_2 was 2.70 nm. The trend in length is also true for FcNSAc. FcNSAc showed a thinner SAM of 2.38 nm with a higher log conductance of -7.33. Fc3NSAc had a thickness of 2.31 nm with the smallest log conductance of -8.44. As this thickness is similar to FcNSAc, the factor affecting the conductance could only be the positioning of the nitrogen atom on the phenyl ring. This confirms the findings from the previous section, showing that 'unbound' anchors (the nitrogen arm in this case as deduced from the XPS results) can influence the electronic properties.

Table 5.2: Table showing the structural and electrical properties of SAMs 1, 2, 4 and 5.

SAMs	**log(G/G_0)**	**Thickness (nm)**
$Fc(SAc)_2$	-6.30	1.58
Fc_2SAc_2	-8.19	2.70
FcNSAc	-7.33	2.38
Fc3NSAc	-8.44	2.31

As we add pyridyl anchor groups the conductance also drops. FcNSAc has a log conductance of -7.33, where the nitrogen sits in the para position which is a 16.35% decrease from $Fc(SAc)_2$. As we move the nitrogen to the meta position (molecule 5) the conductance continues to decrease to a $\log(G/G_0)$ of -8.44. This is a 33.97% decrease from having sulphur anchor groups and a 15.14% drop from FcNSAc. The results are summarised in table 5.2.

Pei et al. suggested that for the ferrocene-based molecules they experimented with, the conductance was lower when the dihedral angle between both the arms exceeded 60°(arms in an 'open' configuration).[16] This explains the difference in conductance between the molecules experimented with in Part 1 and Part 2. Although sulphur provides a stronger bond to the gold and typically shows higher conductance for alkyl-chained molecules, in this case, the conductance was found to be much lower than those with the pyridyl anchors due to the open configuration of these ferrocene molecules. As the length increases due to the open arms, it is expected the conductance decreases, as aforementioned.

5.4 Summary of Findings and Future Work

Within this chapter, we sought to explore the unique rotational features of 1,1'-dialkynyl ferrocenes with nitrogen and sulphur anchor groups. The first section experimented with the nitrogen positioning around the phenyl ring and the effect caused by removing an alkyne arm. The second part of this chapter investigates dialkynyl ferrocenes with sulphur anchor groups and studies the effect of the nitrogen positioning when a sulphur anchor group is present. We also investigated the impact on the electrical conductance of including an additional ferrocene into the

structure.

An examination of the thickness of the assembled thin films in Part 1 suggested that these molecules prefer to occupy a 'hairpin' geometry, a result which is consistent with the theoretical calculations of molecular geometries. Previous works have shown that an 'open' conformation is achievable for similar molecules, for example for molecules investigated in Part 2.[188, 16] The preferential conformation found for both these sets of molecules appears to be dependent on the chain group attached to the sulphur, considering FcNS is very close in structure to FcNSAc.

This is further supported by investigating the electrical properties of molecules with 'open' conformations. The thickness of each dialkynylferrocene thioacetate SAM highly indicates a fully stretched molecule. To confirm the binding of the anchor groups, a similar analysis could be performed on the surface using ARXPS to determine whether both anchor groups are pointing toward the surface. As we have witnessed, the alignment of the unbound arm greatly affects the conductance produced. By comparing FcNS and FcNSAc, the conductance can be enhanced by $\sim$38.6% when in a closed formation as opposed to an open one. To fully complete the characterisation of these molecules, it would be beneficial to determine the thermopower exhibited by each ferrocene in Part 2.

This represents an interesting augmentation to previous work in the field which has demonstrated that the inter-arm angle between the two substituents of a 1,1'-disubstituted ferrocene infers significant control over the molecules conductive properties.[188, 16]

Work in the first half of this chapter has been published in collaboration with Imperial College London (Wilkinson et al., Chemical Science, 13, 28 (2021).[219]

Chapter 6

Multi-Component Self-Assembled Molecular-Electronic Films

This chapter describes experiments designed to grow multilayer organic films with alternating molecular components. Specifically, we focus on the idea of 'slippery linkers' using rigid anthracene molecules and zinc porphyrin as the slippery linker. Parts of this work have been published in Chemical Science, which will be clearly stated in the results section.[220]

6.1 Introducing Slippery Linkers

It is well established that thiol strongly binds to gold, and the strong binding limits its tunability. The binding energy between the two is more than 1 eV, which enhances the mechanical robustness but at the same time induces mechanical stiffness which controls phonon transport across the interface and cannot be tuned. Rigid contacts also diminish the efficacy of these designs in thermoelectric applications, where the decoupling of electronic and thermal contributions presents an exciting avenue in the fabrication of systems with high values for the thermoelectric figure of merit (ZT).[221, 222, 223] Within this study, we aimed to overcome this limitation by investigating new strategies towards the formation of thermoelectrically efficient devices containing highly asymmetric electrode-anchoring groups, which realize, for the first time, QI enhancement of the thermoelectric properties of multi-layered

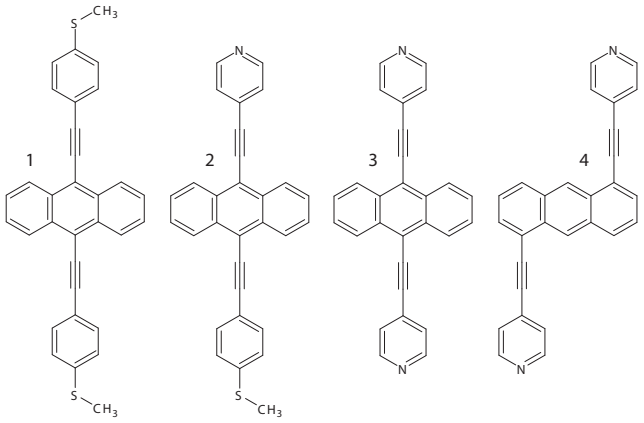

Figure 72: Chemical structures of anthracene 1: (9,10-Di(4-(ethynyl)thioanisole)anthracene), 2: (9-(4-(Ethynyl)pyridine)-10-(4-(ethynyl)thioanisole)anthracene), 3: (9,10-Di(4-(ethynyl)pyridine)anthracene) and 4: (1,5-Di(4-(ethynyl)pyridine)anthracene).

films. To achieve this, we aimed to assemble a system containing a highly conductive, and rigid 'sticky' linker, that displays strong features of constructive quantum interference (CQI) and bind this to a gold electrode at one end. The other end was then bound to either a platinum electrode or a graphene-coated platinum electrode, through the use of a 'slippery' linker with an extended π-system, whose propensity to π-stack with graphene should facilitate high-conductance, whilst limiting thermal propagation associated with phonon transport (due to its non-covalent interaction). The ability to create stacked multi-component assemblies, whilst preserving CQI, is highly desirable. It has previously been demonstrated that the Seebeck coefficient of two C60 molecules stacked on top of each other is significantly higher than that of a single C60 and we were keen to investigate whether a similar effect could be translated into asymmetric CQI-enhanced multi-component films.[24]

An asymmetric unimolecular system is synthetically challenging and would also be unlikely to form well-ordered molecular films. We overcome this challenge through the use of multi-component self-assembly. We fabricated multi-component systems composed of, first, rigid molecular wires based around a central anthracene-core (Figure 72) and secondly, a ZnTPP (zinc tetraphenylporphyrin) 'slippery' linker. The aim is to couple the metal centre of the ZnTPP to the exposed terminal group of the assembled wire (Fig. 1(b)). These wires differ in the nature of their terminal groups, which contain thiomethyl–thiomethyl (1), thiomethyl–pyridyl (2) and

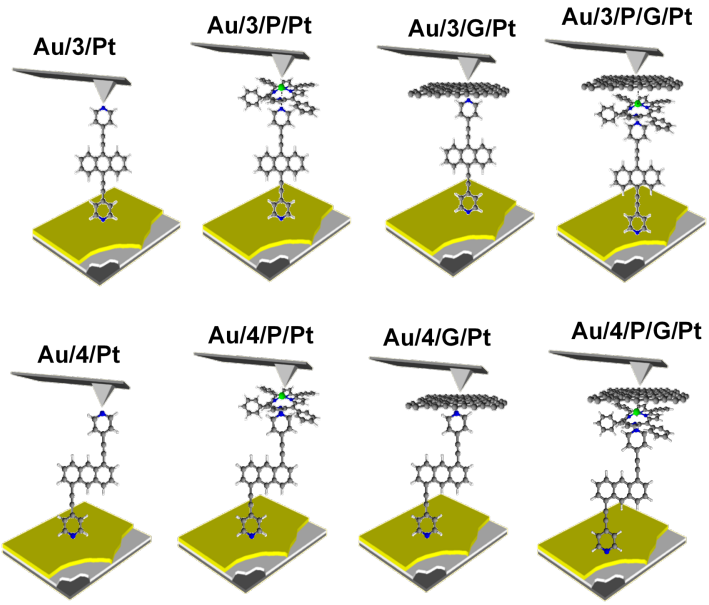

Figure 73: A schematic representation of the junctions fabricated. Here, the bottom contact is gold, either molecule 3 or 4 is the monolayer, P represents the porphyrin monolayer, G represents measurements taken with a graphene-coated probe and Pt represents a platinum-top contact.

pyridyl– pyridyl (3,4) termini, as well as in their connectivity around the anthracene molecular core i.e. a 9,10-substitution pattern around the anthracene core (in 1–3) vs. 1,5-substitution (in 4). These molecules were chosen because they can be assembled to form well-ordered molecular films that demonstrate strong features of CQI at room-temperature.[104, 224, 225, 226]

Solution-based NMR experiments were initially used to evaluate anthracenes' propensity (1–3) to bind to ZnTPP. After observing that the dipyridyl species (3) bound with the highest efficiency, we assembled 3 and 4 into thin film materials and subsequently deposited Zn-TPP on top. The thermoelectric properties of SAMs 3 and 4 were then evaluated, experimentally and theoretically, with and without the inclusion of a porphyrin cap, and utilizing different platinum top contacts. Figure 73 shows the junctions we focussed on throughout the study to evaluate the hypothesis of increased thermoelectric efficiency. Here, Au represents the bottom gold substrate and the number denotes a monolayer of the corresponding anthracene molecule in Figure 72. To note, in some cases, SAMX will be used interchangeably with Au/X, where X represents the numbered anthracene molecule.

6.2 ^{1}H-NMR Coordination Studies

To first examine the viability of complex formation, collaborators from Imperial College London, Troy Bennett and Nicholas Long, performed solution-based ^{1}H-NMR experiments on three of the different termination groups: thiolmethyl/thiomethyl, pyridyl/thiomethyl/ and pyridyl/pyridyl. For an in-depth analysis of these results, please refer to the paper cited.[220] Briefly mentioning the method, ZnTPP was dissolved in $CDCl_3$ and added to molecules 1-3 in both, a 1:1 ratio and 1:2 ZnTPP:2 ratio. These results were compared to ^{1}H-NMR of the pure anthracene molecules to detect any changes. Examining molecule 1, they found that there had been no change in peak sizes or positions after the addition of ZnTPP, suggesting thiolmethyl termini do not bind to ZnTPP. Molecule 2 with a mixture of the two functional groups showed some interesting changes in combination with ZnTPP. Their key findings are presented in Figure 74. For the ratio 1:1, the α and the β proton relative to the nitrogen atom peaks experience an upfield shift around 2.0 ppm from $\sim$8.6 ppm and $\sim$7.6 ppm (shown by the dashed line). In contrast to this, the α, β protons attached to the thiol and the ones on the methyl group shifted with an approximately 0.7 ppm shift. This signifies molecule 2 binds to the porphyrin through its nitrogen atom, with peaks attributable to thioanisole associated protons shifting only slightly, as a result of porphyrin coordination at the other end of the molecule. They found similar trends for molecule 3 where a large upfield shift was generated for all the anthracene associated protons. These results show clear evidence of binding between the two molecules, and therefore provides good evidence that binding should be possible within a multilayer SAM. This idea of multi-component SAMs is therefore explored in the remainder of this chapter.

6.3 SAMs Growth and Formation

Anthracene and zinc porphyrin molecules were synthesised at Imperial College London and were deposited onto Au(111) for SAM formation. Template stripped gold was prepared following the procedure in Section 4.0.1. 1 mM solution of each molecule 1 to 4 was dissolved in >99.5% toluene (purchased from Sigma Aldrich) and deoxygenated for 10 minutes with nitrogen. Freshly cleaved template-stripped

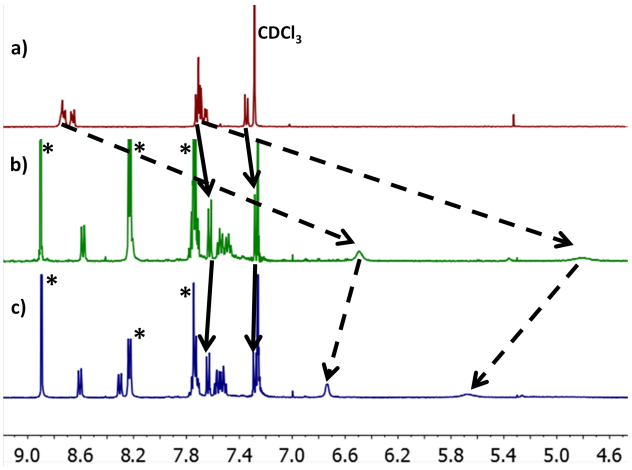

Figure 74: ^{1}H-NMR spectra of (a) anthracene 2; and two other spectra of anthracene 2 and ZnTPP mix with a (b) 1:1 ratio, and (c) 2:1 ratio, respectively. Dashed line represents the movement of pyridine-related protons and the solid line shows the movement of thioanisole protons. * indicates the protons associated with porphyrin. Results obtained from Bennett and Long.

gold was then immersed in the solution and incubated under a nitrogen atmosphere for 24 hours. The substrate was rinsed thoroughly with toluene and IPA to remove the physisorbed material. Following this, the sample was dried with, first, a nitrogen gun, and then placed in a vacuum oven at 35°C with a pressure of $\sim 10^{-2}$ mbar to evaporate any remaining solvent overnight. A solution of ZnTPP 100 µM in toluene was made and the anthracene-Au sample was immersed for 20 minutes to deposit the porphyrin layer.

The following topography images are of anthracene 1-4 after ZnTPP deposition and were taken by Xintai Wang (Figure 75). Previous work by Wang et al. showed that anthracene molecules form well-ordered monolayers.[104] The brighter spots visible on the AFM images show ZnTPP interacting with the monolayer of anthracene below. Evidently, there is little to no deposition of ZnTPP observed on anthracene 1 in comparison to anthracene 2, 3 and 4. SAM3 and SAM4 appear to have a more continuous layer of ZnTPP as opposed to the SAM2 sample where it clusters.

Nano-scratching measurements were then performed (by Xintai Wang) on samples 2-4 (with ZnTPP) to determine the height difference between the scratched area and non-scratched area indicating the thickness of SAMs formed (Figure 76). The thickness of SAM3 was found to be 1.2 nm which indicates that the molecules are standing upright with a tilt angle of 47°as the molecular length of anthracene 3 is

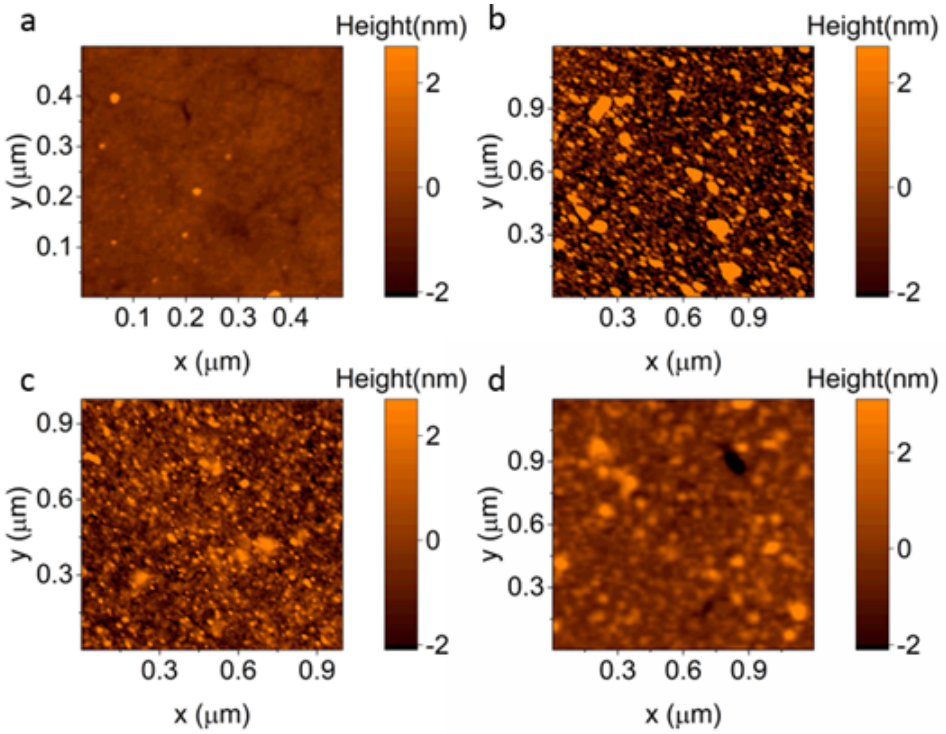

Figure 75: Topography of the four anthracene molecules after ZnTPP (P) deposition: (a) Au/SAM1/P (b) Au/SAM2/P (c) Au/SAM3/P (d) Au/SAM4/P.

around 1.9 nm. After ZnTPP deposition, the thickness was measured at 1.8 nm. The thickness of a single layer of ZnTPP is ∼0.45 nm lying flat to the substrate.[227] This is comparable with the difference found between SAM3 and SAM3/P. For SAM4, the thickness was measured to be 1.1 nm with an increase of 0.6 nm for the ZnTPP layer. The height of SAM4 indicates anthracene 4 has an average tilt angle of 50°.

With QCM, AFM topography and nano-scratching, they identified the order of amount of ZnTPP deposited to be SAM1 < SAM3 ∼ SAM4 > SAM2, following the same deposition procedure.

6.4 X-ray Photoelectron Spectroscopy

Each anthracene was deposited onto a gold substrate and examined by XPS before and after ZnTPP exposure to observe any changes in the chemical environments as a result of the complexation of the Zn core to anthracene anchor groups. An area of the sample (350 µm × 700 µm) was chosen, small enough to avoid possible multilayer deposition of ZnTPP and artefacts arising from template stripped gold.

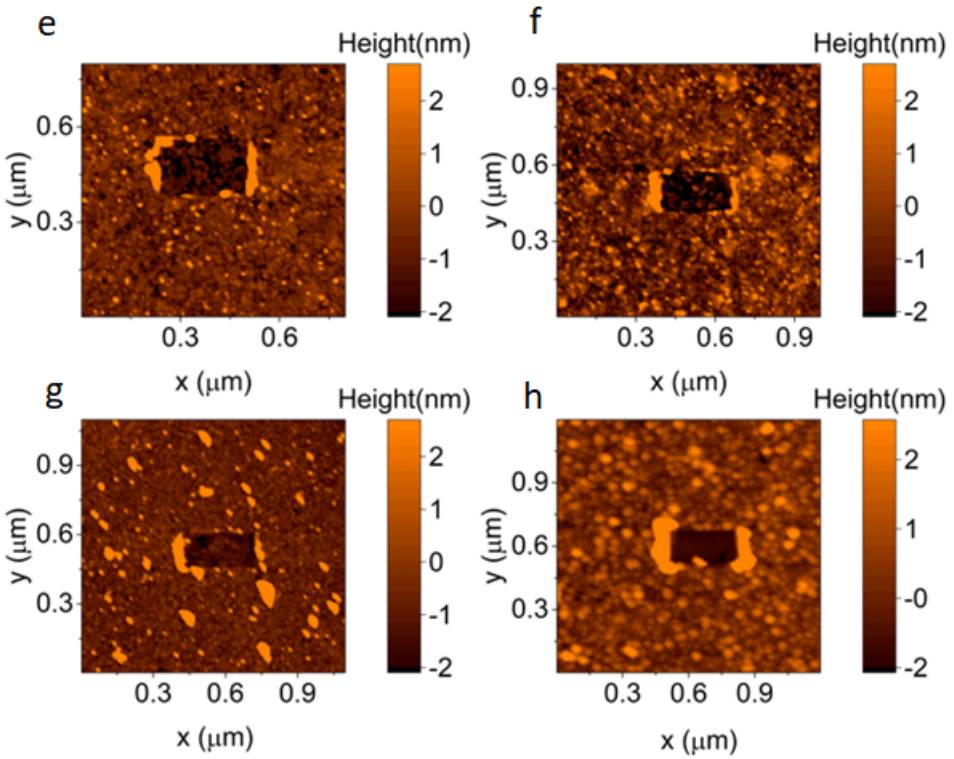

Figure 76: Nano-scratch images of (e) Au/SAM3 (f) Au/SAM3/P (g) Au/SAM2/P (h) Au/SAM4/P. Images taken by Xintai Wang.

All spectra was calibrated using C-C as the reference peak with a binding energy of 284.8 eV. Figure 77 shows the sulphur region for both SAM1 and SAM1/P. In both spectra, the typical characteristics of sulphur doublets can be seen. The doublets are Gaussian-Lorentzian fitted with a splitting of 1.2 eV.[182] The first set of doublets in SAM1 is found at 161.9 eV and 163.1 eV which arise due to the S $2p_{3/2}$ and S $2p_{1/2}$, respectively. These peaks will be assigned a 2:1 area ratio, corresponding to 4 electrons in the $2p_{3/2}$ level and 2 electrons in the latter. Sulphur chemisorbed to gold is a well-studied process and from previous literature, the peak (green) arising at 161.9 eV is attributed to bound sulphur to the surface.[211, 212, 183]. The second set of doublets peaks at 162.98 and 164.17 eV, and aligns with the assignment of the unbound free terminal SMe group.[110, 103] After deposition of the ZnTPP, the bound sulphur peak is found at 161.86 eV and the unbound sulphur is found at 163.05 eV. Comparing the values before and after ZnTPP deposition, there are no significant shifts in energy, indicating that the sulphur groups are unchanged.

The area of the unbound and bound sulphur lies very close to a 1:1 ratio, indicating equal amounts of sulphur bound to the substrate and 'free' sulphur groups i.e. a

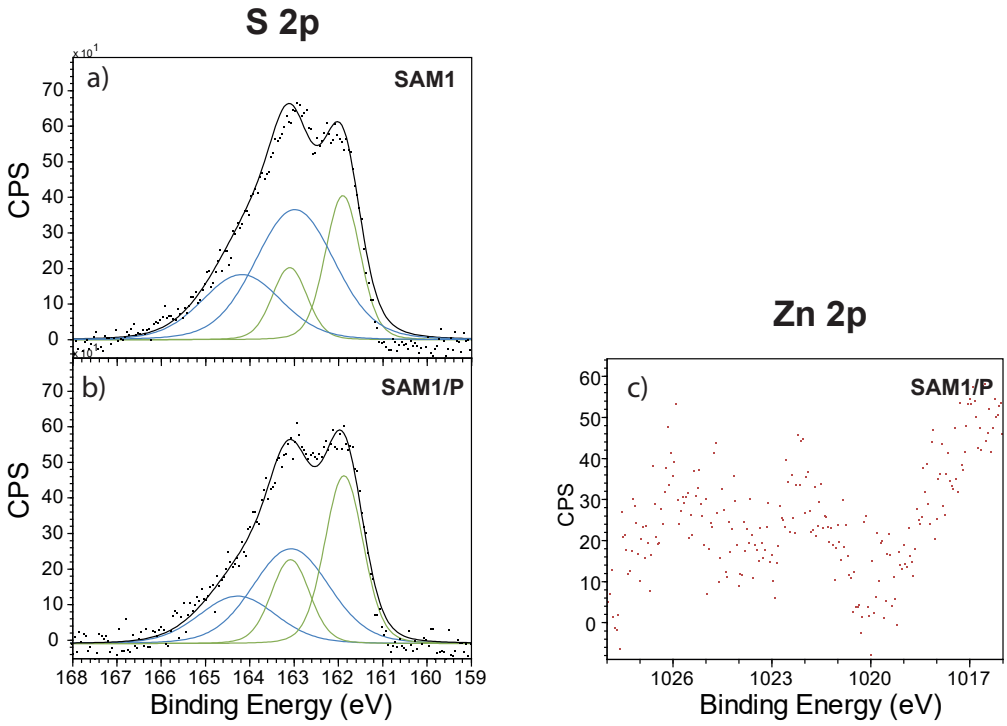

Figure 77: XPS characterisation of SAM1 before (a) and after (a, b). Spectra (a) and (b) show the sulphur 2p region where the blue curves represent unbound sulphur and green shows the bound sulphur. (c) shows the Zinc 2p region, specifically the 2p $_{3/2}$ spin orbital.

uniform monolayer. This is to be expected from the chemical structure of anthracene 1.

Figure 77 shows the spectra in the Zinc 2p region after exposure to ZnTPP. There were no peaks assigned here as the spectra was noisy. In comparison, the counts per second are significantly lower than those in the sulphur region. Both these points show that there were no Zn molecules that remained on the surface after deposition. This agrees with the findings observed in our ^{1}H-NMR studies.

Anthracene 2 with thiol and pyridyl-terminal groups were examined in the S 2p region and the N 1s region (Figure 78). Similarly to SAM1, the sulphur spectra show the typical characteristics of bound and unbound sulphur groups. The bound sulphur peaks at 161.89 eV, similar to SAM1. Likewise, the unbound sulphur atom is found at a binding energy of 163.4 eV. The two S 2p spectra of SAM2 show a taller peak S $2p_{1/2}$ peak for the unbound sulphur, causing the spectra to appear wider (a smaller additional shoulder is observed). It is more prominent in this particular anthracene SAM because the area between unbound and bound sulphur is not equal.

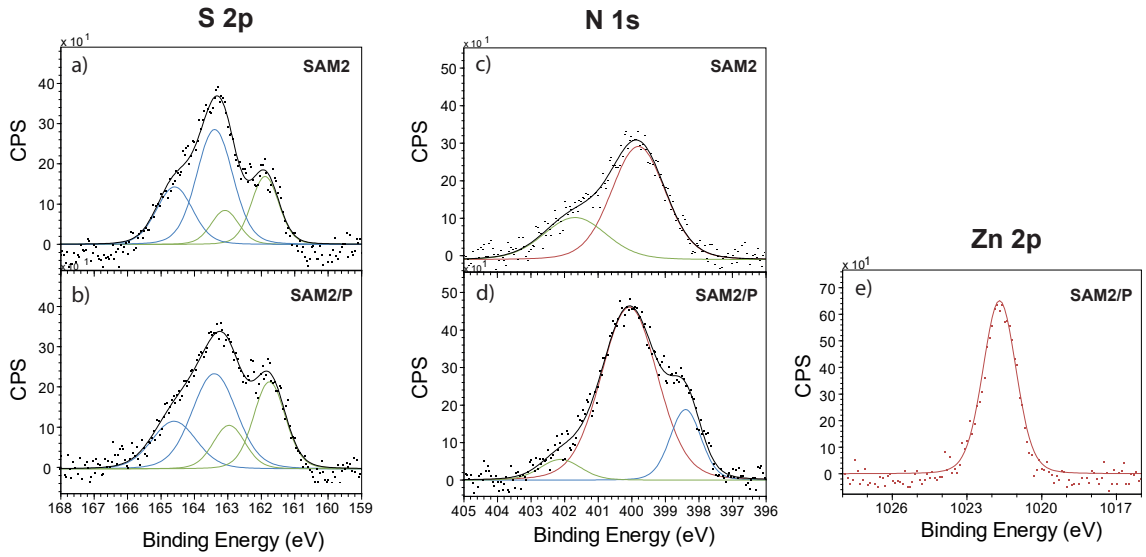

Figure 78: XPS characterisation of SAM2 before (a, c) and after (b, d, e). Spectra (a) and (b) show the sulphur 2p region where the blue curves represent unbound sulphur and green shows the bound sulphur. (c, d) show the peaks in the nitrogen 1s region, where green is assigned to the bound nitrogen and red is unbound. (e) Zn 2p region.

In this film, the area ratio is 2:1 unbound to bound sulphur, indicating that the thiol group is not always chemisorbed onto the surface. After ZnTPP deposition, the ratio gap becomes smaller at 1.5:1. This could be due to the solvent removing some of the molecules from the monolayer. To support the evidence of a mixed layer forming, XPS was taken in the N 1s range and is shown in Figure 78(a) and (b).

Considering SAM2, there are two peaks that can be seen in the N 1s region, which are contributions from unbound nitrogen showing photoemission at 399.8 eV and bound at 401.68 eV.[228, 183, 229, 230] This is in line with the previous results in Chapter 5. The film shows a larger unbound nitrogen species, this could be explained by the evidence of both terminal groups containing bound and unbound species, strongly indicating the presence of a mixed layer formation. As reported by Xintai Wang, the topography of the film formed with anthracene 2 is disordered which could contribute to the abnormalities between the unbound and bound species of sulphur and nitrogen in both cases.

After the addition of ZnTPP, there are no significant energy changes in the sulphur region however, an additional nitrogen peak appears at 398.4 eV. This arises because of the quaternary nitrogen within the porphyrin macrocycle, showing evidence that

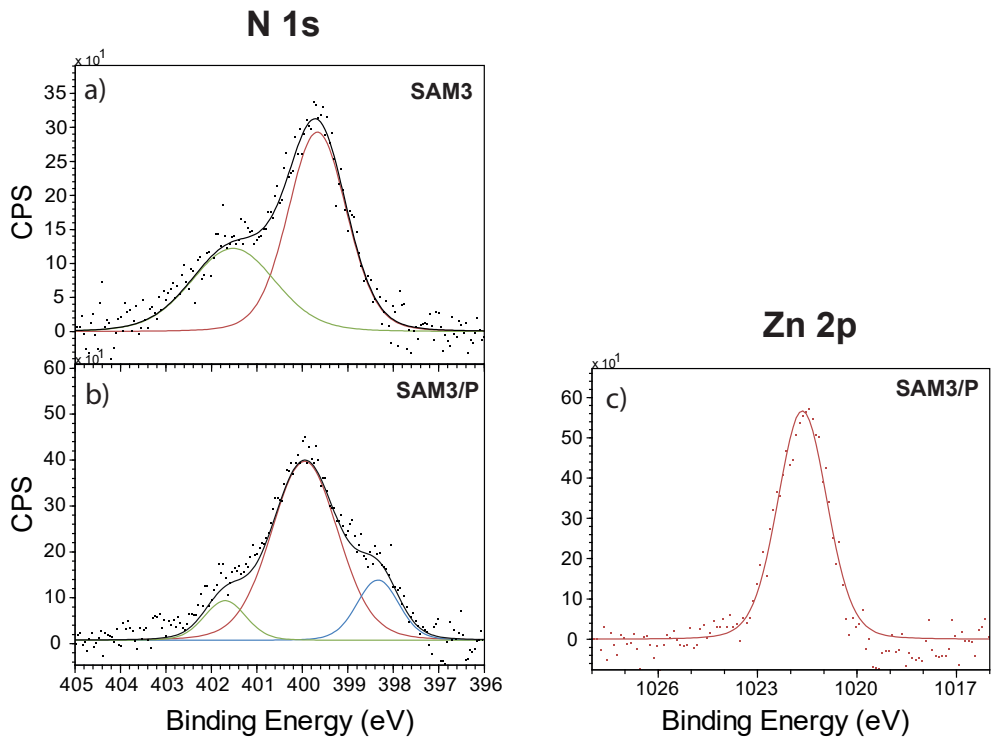

Figure 79: (a) and (b) are spectra taken in the nitrogen 1s region of SAM3 and SAM3/P. Green here represents the bound nitrogen and red represents unbound. The blue curve is attributed to the nitrogen in the porphyrin macrocycle. (c) Zn 2p region of SAM3/P.

ZnTPP is present on the sample.[231] To further support this fact, the zinc spectrum is shown in Figure 78(e) and a major peak is visible at 1021.7 eV. This arises due to the 2p $_{3/2}$ orbital of the Zinc. A peak can also be observed for the 2p $_{1/2}$ spin at 1044 eV, however as literature tends to compare the 2p $_{3/2}$ spin states, this peak is omitted from the figure.

Measurements on SAM3 also shown significant Zn-N binding (Figure 79). Unbound nitrogen is present at 399.7 eV and bound found at 401.5 eV. The Zn-N peak (blue line) appears at 398.3 eV, with little difference in the energy shift compared to SAM1 and SAM2. In most cases, the contribution from the unbound nitrogen is much larger than the contribution from the bound nitrogen. Although this result is unexpected it is not uncommon to find.[229, 231, 232, 233, 234] This is more prevalent in ZnTPP capped samples and can be attributed to the fact that the bound nitrogen is shielded from the x-ray by the larger porphyrin layers, increasing the attenuation factor. Figure 79(a) also shows that SAM3 produces unequal areas for the nitrogen peaks (1:1.5 bound to unbound). As the same with the porphyrin

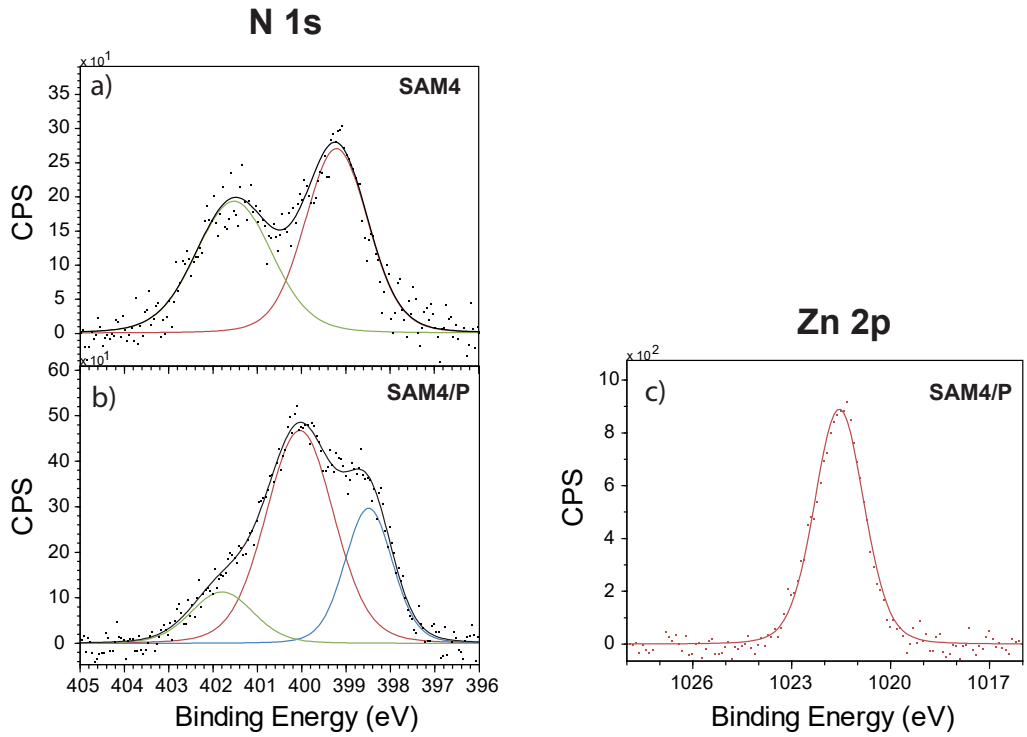

Figure 80: XPS characterisation of SAM4 before (a, c) and after (b, d, e). Spectra (a) and (b) show the sulphur 2p region where the blue curves represent unbound sulphur and green shows the bound sulphur. (c) and (d) are spectra taken in the nitrogen 1s region. Green here represents the bound nitrogen and red represents unbound. The blue curve is attributed to the nitrogen in the porphyrin macrocycle.

cap, as the molecule is 'straight', the top nitrogen could be shielding the bottom one slightly causing this difference.

The zinc peak present after the exposure arises at 1021.65 eV (Figure 79(c)), which agrees with the Zn peak produced by SAM2. This implies further that a complex will form between the ZnTPP and the nitrogen atoms of the anthracene.

Figure 80 shows the data recorded for SAM4 and SAM4/P. Bound nitrogen was found at 401.53 eV and unbound was found at 399.22 eV. Again, these values are similar to the previous data of SAM2 and SAM3, with no significant energy changes. The area ratio between these two peaks lies closer to 1:1 indicating a monolayer coverage.

Comparing the N 1s spectra of SAM3/P and SAM4/P, the area found for nitrogen within the porphyrin (398.3 eV and 398.5 eV, respectively) has a higher ratio in the latter. This indicates a higher concentration of Zn on the surface of anthracene 4. The formation of the top layer could be more uniform and compact due to the

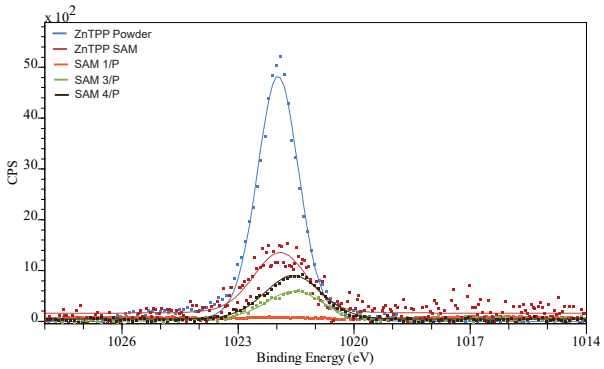

Figure 81: XPS characterisation of surface binding in the Zn 2p region for SAMs 1, 3 and 4 complexed to ZnTPP, referenced to a ZnTPP SAM and its powder form. Blue line shows the pure ZnTPP in powder form, red is a monolayer of ZnTPP on gold, orange represents monolayer of anthracene 1 + ZnTPP, green shows monolayer of anthracene 3 + ZnTPP and brown shows anthracene 4 + ZnTPP.

'kink' in the anthracene structure, spacing out the anthracene molecules which in turn aligns the ZnTPP capping layer better. This is in line with the QCM data where the amount of molecules increased from approximately 8×10^{17} for SAM3/P to $\sim$10 $\times 10^{17}$ for SAM4/P.

Comparing the capped samples and the non-capped samples of SAMX and SAMX/P, the area of the nitrogen peaks from the anthracene molecules tend to decrease as we add ZnTPP to the sample. This is most likely when submersion of the already prepared SAM in toluene, the toluene is removing some of the pristine layer.

Measurements taken in the Zn 2p region were recorded to confirm the presence of ZnTPP after deposition, shown in Figure 81. As we have seen, there has been evidence of Zn on SAM2, 3 and 4. Although this confirms that Zn is on the surface the complexation forming between the porphyrin and the anthracene is not confirmed. Two controls were prepared, a reference of the ZnTPP powder and a SAM of ZnTPP with no anthracene.

The Zn $2p_{3/2}$ peak arises at 1021.97 eV for a pure powder form of ZnTPP, which aligns with the values commonly found in the literature.[235, 236] When deposited as a monolayer on a gold substrate, there is little significant shift in the binding energy and a peak is emitted at 1022.11 eV. The difference in binding energy shifts 0.5 eV as we begin to expose ZnTPP onto anthracene layers, giving a binding energy of 1021.54 eV for SAM3 and 1021.58 eV for SAM4. This shift in eV can be explained

by the binding occurring between the zinc centre and the nitrogen terminal group. This peak is only visible for anthracenes 2-4, supporting the AFM images taken where little to no ZnTPP is visible on SAM1. Despite SAM2/P showing evidence of nitrogen complexing, due to the mixed layer foundation, further characterisation for this molecule and anthracene 1 was not carried out.

In addition to this if we assume that the Zn centre has complexed to the nitrogen we should expect a peak from the Zn-N interaction in the N 1s region. The reason this is not visible is due to the fact that the peaks emitted from the Au-N bond lie at the same energy emitted as the Zn-N and the contribution of that exceed the latter.[128]

6.5 I-V Characteristics and Electrical Transport Characterisation

Electrical measurements were performed using the C-AFM set up described in Section 4.1.3 with both Pt and graphene-coated AFM probes. The gold substrate acted as a source and the probe as the drain. The probes were coated in a layer of graphene using the Langmuir-Blodgett technique and their quality was checked against the standard Pt Budget Sensor Multi75-G probes used in this study by Xintai Wang. The radius of the graphene-coated was examined by SEM and was found to be similar to that of a standard Budget Sensor radius of 25 nm.

After checking the topography of the samples, an area of the surface was selected for investigation. The following electrical characterisations were only carried out with molecules 3 and 4 due to the lack of evidence displaying ZnTPP complexing to molecules 1 and 2. Figure 82 shows IV curves of anthracenes 3 and 4, with and without the ZnTPP cap. The red line indicates the average current of the sample. The curves display a typical semiconductor behaviour and by directly comparing the two visually (SAMs vs SAMs/P) the conductivity slightly decreases.

All measurements taken with a graphene-coated probe were taken by Xintai Wang. The conductance of a single molecule was estimated by scaling down from SAM by using the RKJ model[206, 207]:

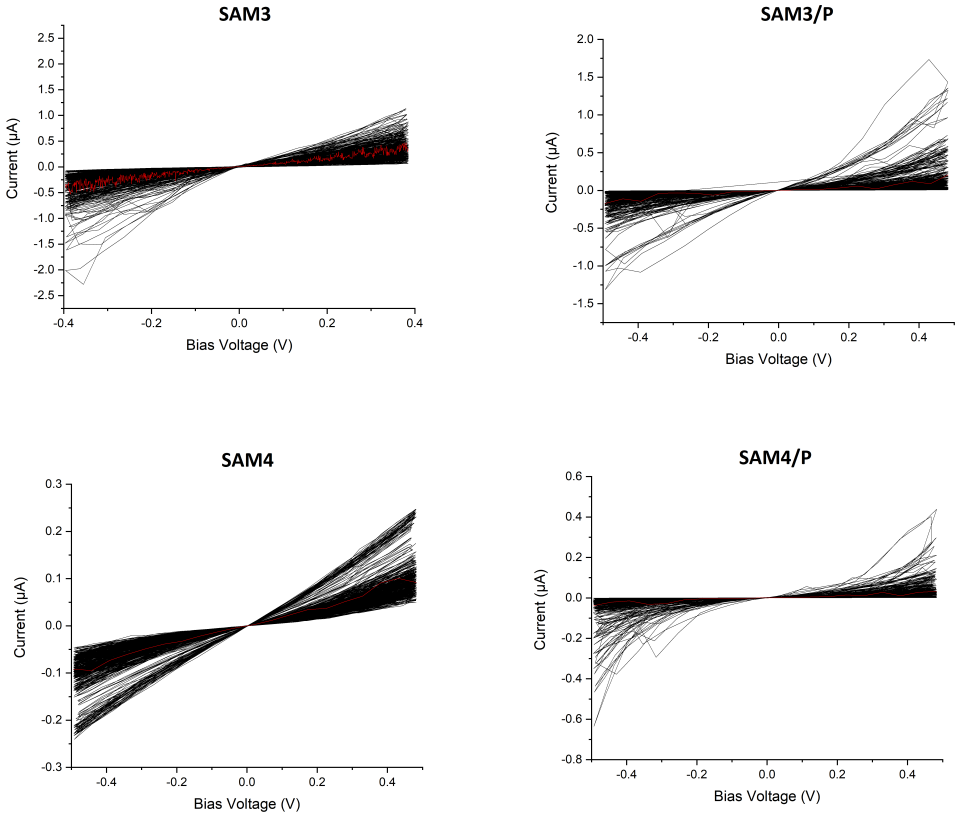

Figure 82: Taken with Pt/Cr probe. I-V curves of monolayers 3 and 4 with and without porphyrin caps. The red line shows the average curve of the statistical plots.

$$r = (F \times R \times \frac{1}{Y})^{\frac{1}{3}} \tag{6.1}$$

$$\frac{1}{Y} = \frac{3}{4} \times \left(\frac{1 - v_1^2}{E_1} + \frac{1 - v_2^2}{E_2} \right) \tag{6.2}$$

Here r represents the contact radius, F is the loading force, R is the radius of the probe, which was estimated to be 25 nm by SEM imaging v_1 and v_2 is the Poisson ratio of the material and E_1 and E_2 are the Young's Modulus of the probe and sample monolayer, respectively. The Young's Modulus was determined by PeakForce AFM and it resulted around 2 GPa for the SAMs. Additional parameters were taken from studies working on similar systems.

To gain more insight into the I-V characteristics, two-dimensional IV graphs are constructed from >200 different IV curves (Figure 82) by considering the differential, dI/dV.

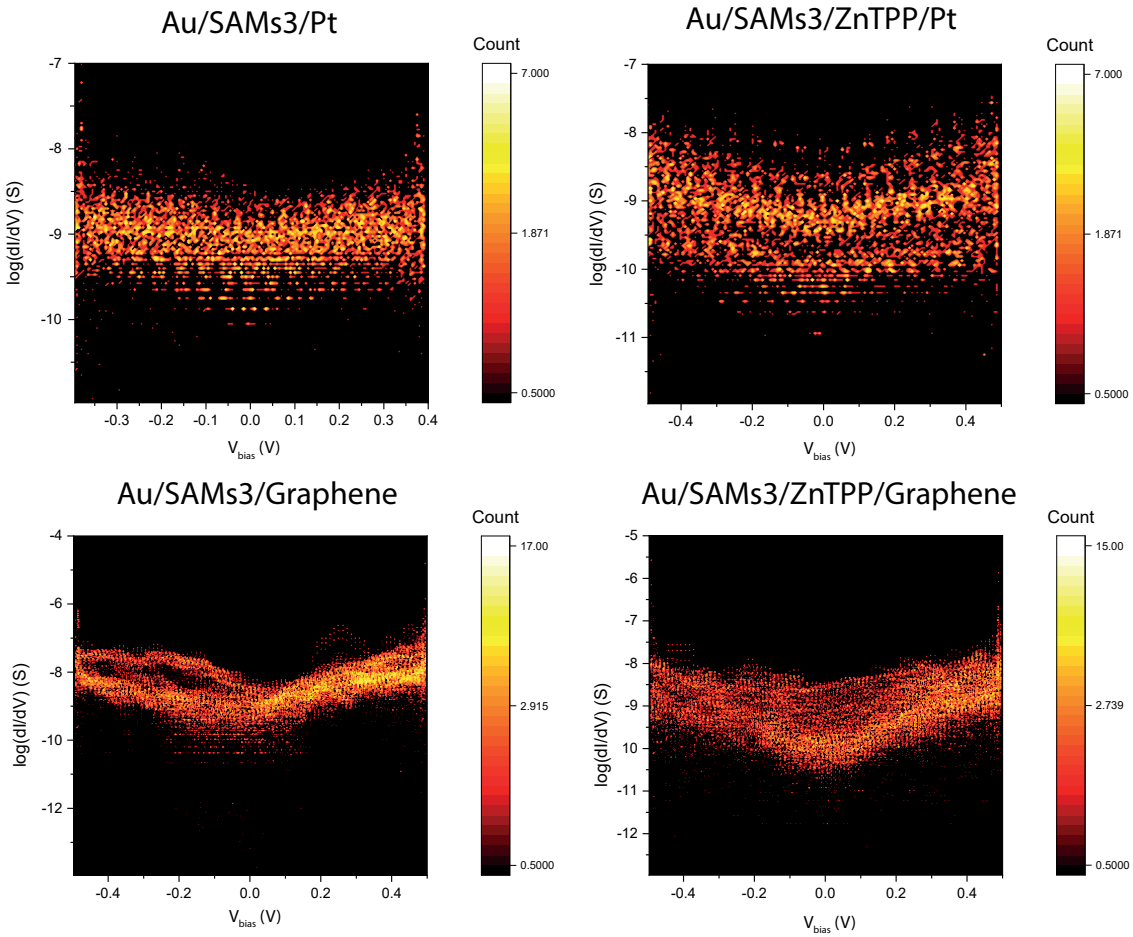

Figure 83: Electrical conductance counter maps of anthracene 3 and its junctions. Graphene-coated probe measurements were taken and extracted into histograms by Xintai Wang.

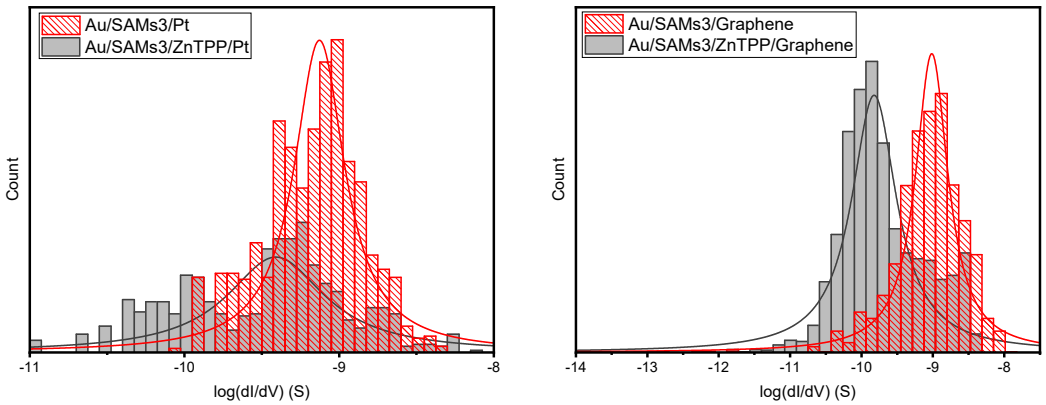

Figure 84: Conductance distributions of SAM 3 junctions close to the zero-bias region. Graphene data was collected by Xintai Wang. Histograms in red show monolayers of the SAM formation of 3 and 4. Grey histograms involve a ZnTPP cap.

The conductance values for SAM3 were scaled down to a single molecule. Through the calculation in equation 6.2, the number of anthracene molecules contacted was estimated to be 848 and with the ZnTPP capping, the junctions were estimated to be 212. Following this, the single molecular conductance ranged between 1.41 $\times 10^{-10}$ and 1.74 $\times 10^{-9}$ S. The statistical IV graphs of molecule 3 and its junctions are shown in Figure 83. From this, the statistically-most-probable differential conductance was evaluated at low bias voltages, between -0.05 V to 0.05 V and displayed in Figure 84. In both cases, we can clearly see, no matter the probe material, there was a decrease in conductivity after the addition of the ZnTPP.

SAM3/Pt showed a log(G) of -9.16 S and SAM3/P/Pt was calculated at log(G) = -9.49 S. The graphene counterparts of SAM3 and SAM3/P were found to be -8.76 and -9.85 S (log(G)), respectively. SAM4 also follows this trend after exposure to ZnTPP where the log of the conductance values before and after are -9.70 and -10.10 S for a Pt probe, and -9.03 and -9.90 S for graphene, respectively (Figure 85 and 86).

The conductance (G) ratio between the anthracene SAMs and their porphyrin-coupled structures was interpreted through the use of the following equation linking the internal and interfacial resistances (R) within the junction:

$$\frac{G_{Anth}}{G_{AnthZnTPP}} = \frac{R_{Substrate-Anth} \times R_{Anth} \times R_{ZnTPP} \times R_{ZnTPP-Probe}}{R_{Substrate-Anth} \times R_{Anth} \times R_{Anth-Probe}} \tag{6.3}$$

In all cases, this ratio was higher than 1, as expected due to the additional resistance arising in the junction from R_{ZnTPP}. Comparing the two probes, graphene was expected to produce a lower ratio due to further π-stacking of the porphyrin and graphene junction, which decreases the interfacial resistance $R_{ZnTPP-Probe}$. However, the opposite is observed and this is attributed to the higher binding energy associated with graphene. The transport properties were theoretically calculated by Colin Lambert's group at Lancaster University by using density functional theory (more details can be found in the ESI cited [237]). The binding energy including the graphene interface was calculated to be more than double of the junctions without. The calculations were performed on SAM3 and connected to a gold electrode. In both cases, the inclusion of the graphene layer in the junctions showed a binding energy of 1 eV. SAM3-Au junction had a binding energy of 0.4 eV and SAM3-ZnTPP-Au was calculated to be 0.5 eV, both significantly lower than the graphene-coated probes.

Interestingly, the theory shows that if the fraction of molecules making contact with the electrodes is unchanged by the inclusion of the graphene layer, then we should similarly see a decrease in conductance with the inclusion of the latter. This suggests that the higher binding energy associated with the graphene layer increases the fraction of molecules making contact with the top electrode.

SAM3 generally shows higher conductivity than SAM4 where the values are for a Pt junction: -9.16 S and -9.70 S, accordingly. SAM3/G shows -8.76 compared to SAM4/G at -9.03. This is also true when considering the porphyrin linkers, SAM3/P lies at log(-9.49) S and SAM4/P at log(-10.10) S, SAM3/P/G displays conductance at log(-9.85) S and SAM4/P/G at log(-9.90) S. Junctions of SAM3 and SAM3/P formed with Pt showed a decrease of 5.9 and 6.4 % with respect to SAM4 and SAM4/P, reflecting the higher degree of constructive quantum interference in the former.

This percentage difference is considerably lower for graphene-coated junctions where the decrease between SAM3/G and SAM4/G is 3.08 % and SAM3/P/G and SAM4/P/G is approximately 0.5 %. Although the percentage of enhancement is smaller with the graphene probe, the overall conductance is higher than those taken with a Pt probe,

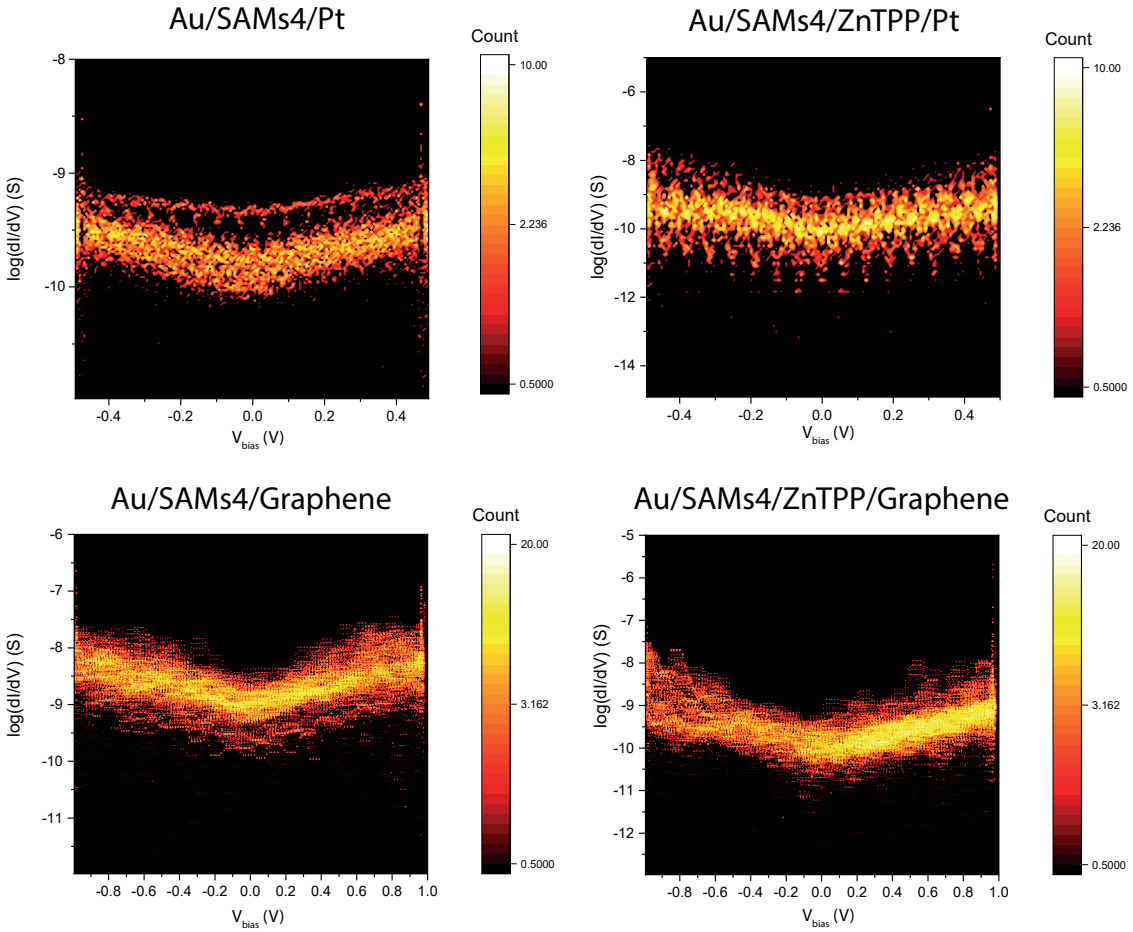

Figure 85: Electrical conductance counter maps of anthracene 4 and its junctions. Graphene data was collected by Xintai Wang.

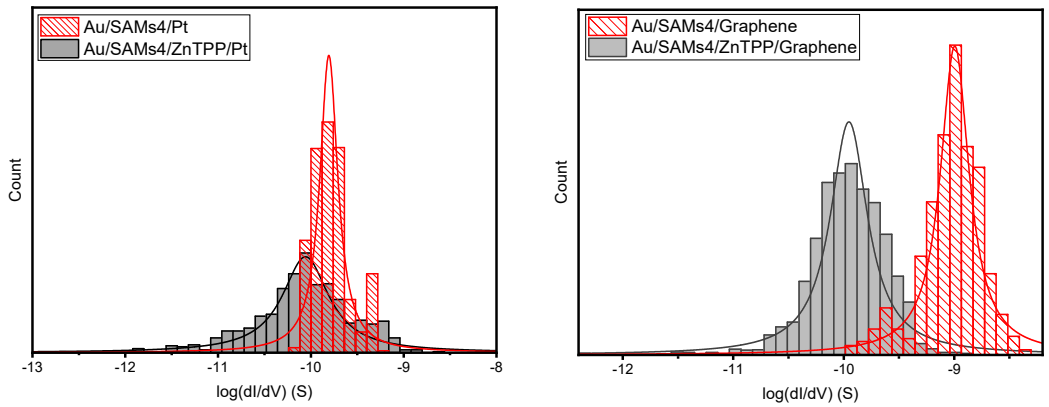

Figure 86: Conductance distributions of SAM 4 junctions. Graphene data was collected by Xintai Wang.

despite the length of the molecular component of the junction. This suggests that the graphene should be regarded as part of the electrode and that inelastic scattering takes place within the graphene as well as the metallic part of the electrode.

6.6 Thermoelectric Characterisation

Seebeck results were determined of all molecule combinations of anthracene 3 and 4 with and without their ZnTPP linkers using both platinum and graphene coated probes. The set-up used was described in Chapter 4.

The Seebeck measurement was obtained from a linear fit of thermal voltage, V_{Th}, vs. temperature difference between sample and probe, ΔT, at four different temperatures. It has been previously shown that the probe can be assumed to be at room temperature due to its high thermal conductivity (Si is ~150 W/mK) and contact with a large thermal reservoir, in this case, the probe holder and body of the microscope.[238]

The thermal voltage for anthracene 3 is plotted against the temperature difference in Figure 87. A positive slope can be observed for all four of its junctions, therefore, resulting in a negative Seebeck value according to the equation: $S = \frac{\Delta V}{\Delta T}$. The measured Seebeck for SAM3/Pt and SAM3/P/Pt was found at -1.22 ± 0.3 and -1.25 ± 0.2 µV/K, respectively. This result was unexpected as theoretical predictions suggested a greater decrease with ZnTPP, showing that experimentally, the addition of ZnTPP has little effect on the thermopower. DFT calculations also predict an improvement of the Seebeck coefficient after porphyrin deposition using a graphene electrode. The theoretical values were expected to come to -9.4 µV/K for just anthracene and -15.1 µV/K with the porphyrin cap, an enhancement of 60.6%. Experimentally, the trend followed what was expected and SAM3/P/G gave a larger Seebeck coefficient than SAM3/G. The results were reported to be SAM3/G = -8.8 ± 0.5 µV/K and SAM3/P/G = -12.9 ± 2.0 µV/K, which gave a 46.6% difference.

The thermal voltage vs temperature difference was then plotted for anthracene 4 in Figure 88. Likewise, the Seebeck obtained for these samples was also negative suggesting that the Fermi levels of both the anthracenes junctions lie closer to the

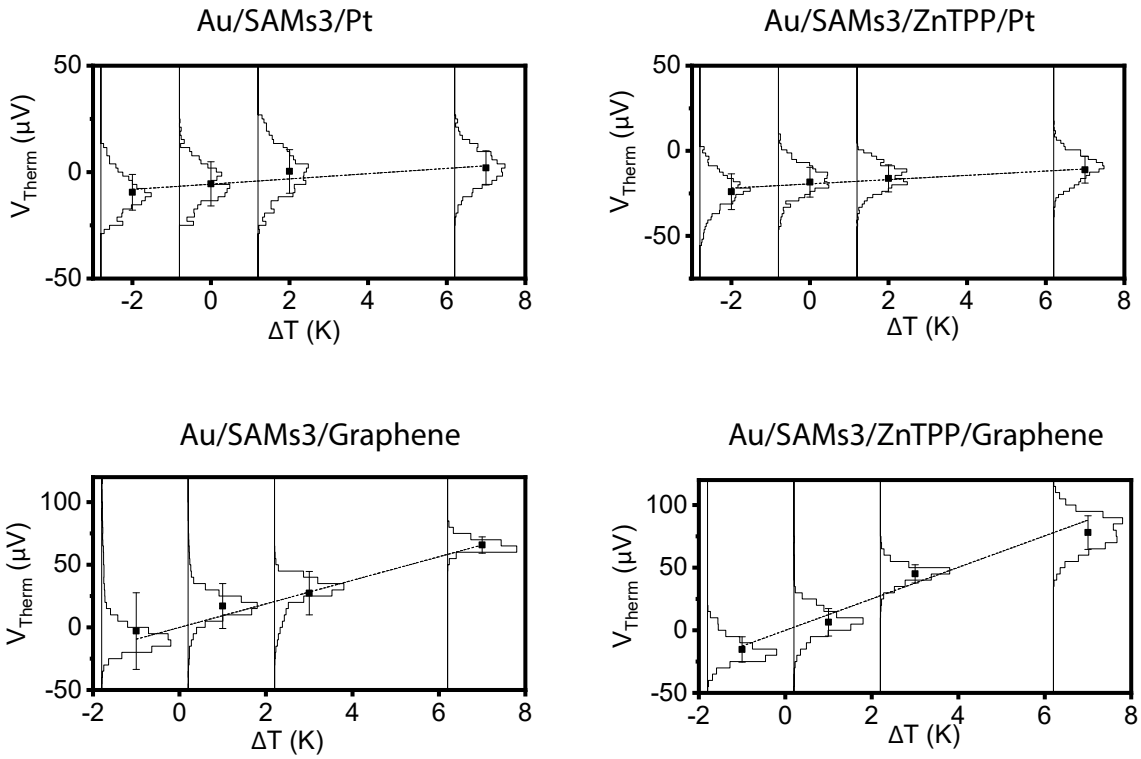

Figure 87: Thermoelectric characterisation of anthracene 3 and its counterparts. Graphene measurements conducted by Xintai Wang.

LUMO resonance of the molecule. This is to be expected due to the presence of pyridyl anchors. SAM4/Pt shows a positive gradient of -5.35 ± 1.3 μV/K whilst SAM4/P/Pt gives a gradient of -12.58 ± 1.3 μV/K. However, the theoretical calculations of the Seebeck indicates there is no significant effect on the Seebeck coefficient. The anthracene 4 and ZnTPP complex is capable of an enhancement of ∼135%. On the other hand, graphene-coated probes were estimated to have an increase of 46.2% increase in Seebeck. Experiments showed SAM4/G to have a value of -7.4 ± 1.6 μV/K and SAM4/P/G -16.8 ± 2.2 μV/K, resulting in a 127% improvement.

Graphene-coated probes all achieved a greater Seebeck than the Pt probes. A reason for this could be due to stronger interaction between the graphene and the molecules, increasing the coupling. The graphene also provides another π-layer in addition to the ZnTPP which will decrease the phonon transport across the junction.

Comparing SAM3 and 4, in most cases, anthracene 4 produces the most thermopower out of the two. From previous studies, this lies in the connectivity around the anthracene core and can also be observed by DFT.[104] The transmission coefficient curves are calculated by collaborators at Lancaster University. They were ob-

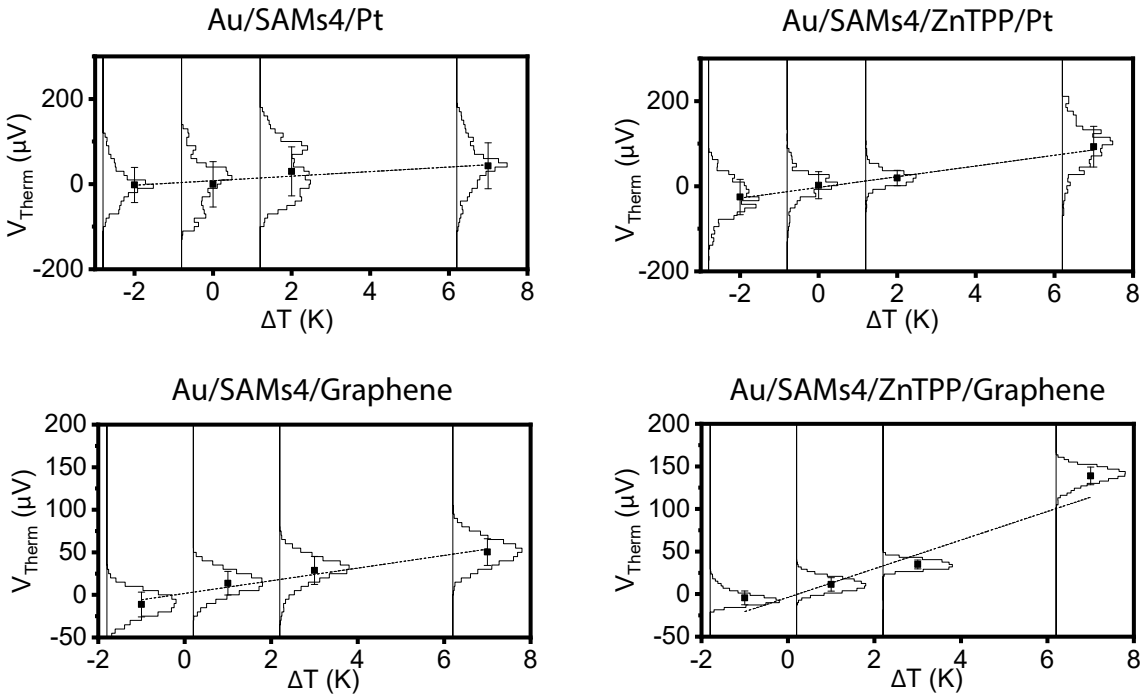

Figure 88: Thermoelectric characterisation of anthracene 4 and its counterparts. Graphene measurements conducted by Xintai Wang.

tained using the Gollum transport code, and comparisons between experiment and theory revealed that electron transport through polyaromatic hydrocarbons takes place near the middle of the energy gap between the highest occupied molecular orbital (HOMO) and the lowest unoccupied molecular orbital (LUMO).[221] These curves are displayed in Figure 89. The SAMs formed prior to the porphyrin layer all display common characteristics of constructive quantum interference whereas the inclusion of the porphyrin layer shows destructive interference. As a note, the theoretical analysis of the conductance indicated higher conductance values for anthracene 3 and can be visually seen where anthracene 4 has a lower log T(E) than 3. The experimental conductance results are in agreement with the DFT.

As the Seebeck is related to the gradient of the transmission function of the junction at the Fermi level, it is to be expected that the latter formation should produce a steeper slope due to the nature of DQI curves. The presence of the ZnTPP sandwiched between the electrode and the 'sticky' anthracene layer disperses some of the phonons and in turn, improves the Seebeck output. This is in line with almost all the experimental studies performed besides anthracene 3 and Pt probes. One of the possible reasons for poor Seebeck results concerning molecule 3 and Pt must lie

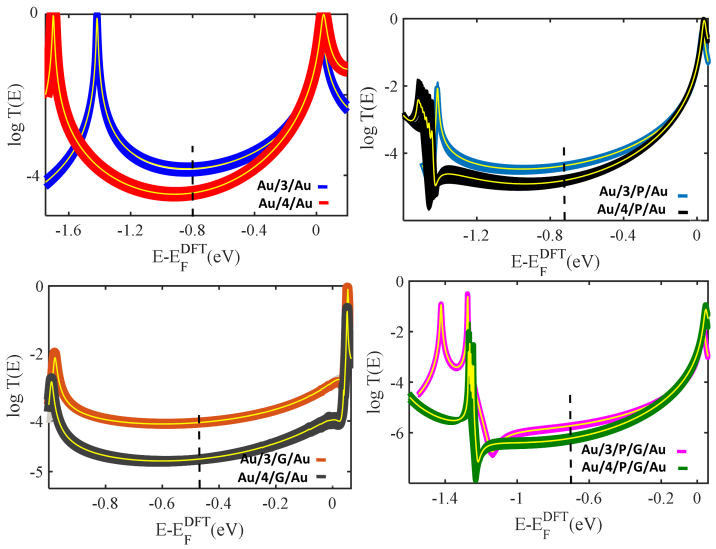

Figure 89: Zero-bias transmission coefficient T(E) of all eight junctions against electron energy, E. (Data courtesy of Lambert et al.)

within the contact area of the Pt probe and the molecule contact. The theoretical models were calculated with the tip directly in contact with the Zn centre, if this is the case experimentally, the practical results should reflect this. However, it is more than likely due to the structural difference in the anthracene molecule and its interaction with the Pt probe. The packing density for SAM3 is an order of magnitude higher than SAM4 according to the QCM results, which would lead to stronger intermolecular interactions in SAM3. Therefore, the overlapping of the pi-pi orbitals between neighbouring molecules means that this could shift frontier molecular orbital energies relative to the Fermi energy of the electrode, resulting in a minimal change of the slope of the transmission function at the Fermi energy.

6.7 Discussion and Summary of Findings

This chapter has shown that utilising multi-layered self-assembly and asymmetric design, the Seebeck coefficients of self-assembled monolayers have the possibility of being enhanced. Solution-based NMR experiments were used successfully to predict the ability of a series of anthracene-based molecular wires to bind to a porphyrin. Through this binding, SAMs of these molecules were able to stabilise the addition of a porphyrin layer to their top face. These SAMs were characterised extensively through the use of AFM and XPS both with and without the inclusion

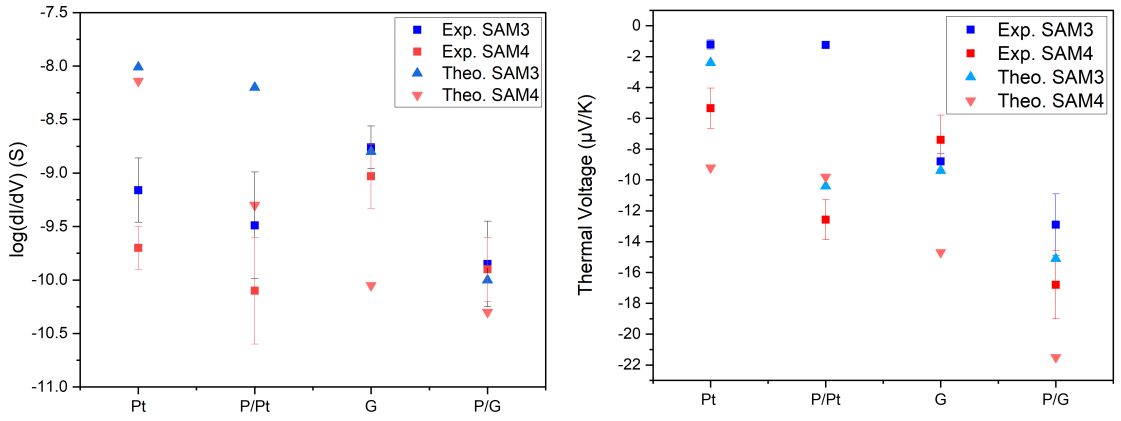

(a) (b)

Figure 90: (a) Electrical properties and (b) thermoelectrical properties of the 8 different junctions. Blue square represents experimental results obtained for Au/SAM3, blue triangle shows its theoretical predictions, red circle is assigned to experimental values obtained for SAM4 and pink triangles are the theoretical prediction for SAM4. Graphene data was collected by Xintai Wang.

of ZnTPP, confirming the discrete structure of these systems and demonstrating a clear translation between the binding behaviour of the molecules in solution and at the mesoscopic scale on a surface.

The key electrical and thermoelectrical results are summarised in Figure 90. Starting from the anthracene-based SAMs from 3 or 4, the conductance decreases after the addition of a porphyrin layer, which is expected. Anthracene 4 is predicted to have lower conductance values due to the smaller CQI effects associated with the 1,5 connectivity around the anthracene core. The inclusion of a graphene layer has shown improvements in the conductance when moving from SAMX/Pt to SAMX/G/Pt whereas SAM4/P/Pt to SAM4/P/G/Pt yields almost no change in conductance, suggesting that the assumption that the transport is phase coherent is incorrect. In the Landauer theory of electron transport, electrons are assumed to pass through a molecule, without undergoing inelastic scattering, i.e. their energy is conserved and they are said to remain phase-coherent. In such a theory, the electrons lose coherence by undergoing inelastic scattering in the electrodes. Provided electrons undergo phase-coherent tunnelling as they pass through the molecule, the conductance should decay exponentially with length. Therefore, the predictions for X/P/G were found to be lower as they followed this assumption.

The difference in the probe surface also influences its conductance and thermoelectric properties. The π-system in the graphene will interact with the headgroups and the π-system in the porphyrin. The only junction in which we do not observe an enhancement is the electrical conductance between SAM3/P and SAM3/P/G. This indicates that the metallic bonding occurring between Pt and porphyrin molecules is able to facilitate electronic transport better than its graphene counterparts. Additionally, any changes in the curvature can cause discrepancies in the conductance when modifying the probe. For example, if the radius of curvature decreases, there will be fewer molecules contacted in the junction, which would in turn cause the conductance to fall, as seen.

When starting with SAMs formed from anthracene 3 and 4, subsequent addition of either a porphyrin layer or a graphene layer can act to significantly increase their Seebeck coefficients. Though we note that this is dependent on the underlying structure. The addition of the porphyrin layer to SAM3/4 enhances the Seebeck by 2.4% and 135.14%. XPS shows results that the ratio of ZnTPP capping to anthracene molecule is lower for SAM3/P than SAM4/P. It is highly likely a lot of anthracenes in SAM3 remain uncapped. This would explain the large percentage difference in enhancement. The addition of both graphene and porphyrin leads to a further increase of 46.6% for SAM3 and 127.02% for SAM4. As mentioned earlier, these differences are attributed to the structural composition of the anthracenes. As for the differences between SAM3/Pt, SAM3/P/Pt and SAM3/G, SAM3/P/G, the $\pi - \pi$ interactions of the graphene and porphyrin could encourage the phonon suppressing qualities needed for a larger Seebeck coefficient. The highest Seebeck coefficient achieved for Pt probes was from SAM4/P/Pt at -12.58 µV/K. For graphene probes, the highest was also from SAM4/P/G junction giving a Seebeck of -16.8 µV/K. From these results, it is evident that anthracene 4 performs the best in terms of providing the highest Seebeck enhancement out of the two structures no matter the top electrode material, indicating that this connectivity will suppress the thermal conductivity more efficiently than anthracene 3.

Chapter 7

Layer-by-layer Assembly on Porphyrin and Phthalocyanines Templates

Here we expand on the ideas from Chapter 6 to examine methods for growing 3D molecular architectures. We explore combinations of deposition techniques to explore a series of porphyrin and phthalocyanine monolayers designed as surface templates for second layer molecular growth.

7.1 Porphyrin and Phthalocyanines

Porphyrins take part in many processes in nature, some examples include an iron(III) porphyrin centre enabling oxygen transport in the human blood and manganese(II) porphyrins are used in chlorophyll for energy conversion. Besides their important role in nature, they are also widely used in material science due to their thermal stability and robustness.[239] The planar nature of the structure with its pi-system allows for various intermolecular interactions to arise, for example, addition of pyridyl or cyano ligands allow the molecule to bond to the surface with different bonding motifs such as by hydrogen bonding and/or metal-coordination bonding.[240, 241]

Similar to porphyrins, phthalocyanines are also aromatic with an 18 conjugated π-

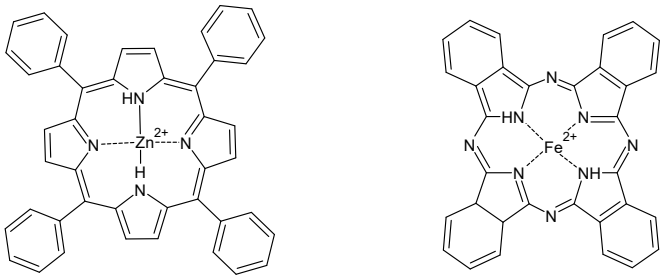

Figure 91: Chemical structure of Zinc tetraphenylporphyrin (ZnTPP) (left) and iron phthalocyanine (FePc) (right).

electrons system (Figure 91). They are more chemically stable than porphyrins and, for practicability purposes, cheaper. This system forms a planar ring and both can form metal complexes. For this reason, both molecules found their way into related research areas e.g. solar cells, photocatalysis and energy storage etc.[242, 243, 244, 245]

Chapter 6 established metal coordination between zinc and nitrogen was possible and thus, Figure 92 shows the linker molecules chosen for this particular study. Firstly, the study began with 4,4'-(1,4-Phenylenedi-2,1-ethynediyl)dipyridine (BipyOPE3) and ZnTPP as this junction is similar to Chapter 6. BipyOPE3 was chosen due to its similarities in length and rigidity as the anthracene molecules we experimented with. As we continued with this work, smaller molecules were chosen for experimentation due to the formation of phase separation between the porphyrin and BipyOPE3, discussed below. We have Figure 92b, BipyOPE2. BipyOPE2 is a smaller variant of BipyOPE3 and should have a more favourable upright formation.

As phase separation became an issue for ZnTPP and BipyOPE3, inspirations were drawn from Isvoranu's studies where similarly a nitrogen atom bonded to a metal centre.[128, 246] Thin films of iron phthalocyanine (FePc) were prepared by vacuum sublimation, followed by a molecule with a nitrogen terminal group (pyridine and ammonia) was then deposited onto the existing layer and examined by XPS. In both cases where ammonia and pyridine were used, XPS showed that the total full width at half-maximum (FWHM) of the Fe 2p peak becomes narrower indicating

(a) (b)

Figure 92: Bipyridine derivatives: (a) BipyOPE3: 4,4'-(1,4-Phenylenedi-2,1-ethynediyl)dipyridine (BipyOPE), (b) BipyOPE2: 4,4'-(ethyne-1,2-diyl)dipyridine.

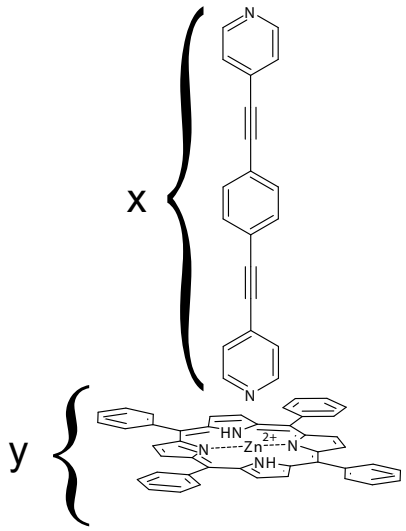

Figure 93: Schematic of desired junction. Here, x can be replaced by any of the other bipyridine derivatives from Figure 92 and y can be replaced by iron phthalocyanine.

high chances of adsorption occurring between the iron core and the lone pair of the nitrogen atom. Here, they assign they explain the narrowing is partly due to the decoupling of the iron core from the Au(111) substrate and additionally due to ligand field splitting, forming a low-spin compound. Thus, the later sections of this chapter will involve replacing the ZnTPP monolayer with a FePc monolayer.

The junction we are intending to prepare is shown in Figure 93. Where the bottom layer of porphyrin (y) is prepared under vacuum, creating a highly-ordered nanoporous network which will align more with the expectations calculated from DFT, and as we have established, a non-uniform layer will negatively affect the electrical properties of the SAMs.

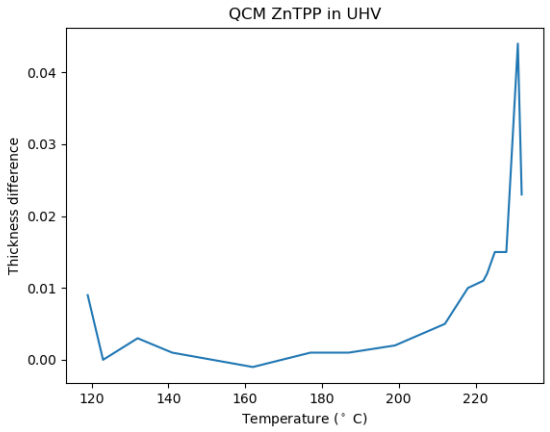

Figure 94: QCM rate of ZnTPP deposition in UHV. The difference in thickness against the temperature of the crucible, shown by the thermocouple.

7.2 Optimising Zinc Tetraphenylporphyrin (ZnTPP) Thermally Evaporated Monolayer

In this particular section, experimental procedures involving zinc tetraphenylporphyrin (ZnTPP) samples were made by thermal sublimation in UHV. ZnTPP was purchased from Sigma Aldrich with a purity of ≥97.5%. The molecular powder was introduced into a crucible as described in Section 4.0.3, and purified through a QCM-monitored sublimation process as described below.

First the thermal sublimation growth was monitored by QCM in vacuum to determine the deposition temperature using a gold coated crystal (diameter 14mm with frequency of 6 MHz). The rate of deposition was determined using INFICON STM-2XM and recorded correspondingly to the table below at regular time intervals of 10 minutes after reaching the desired temperature difference (∼5°C).

As shown in Figure 94, a significant deposition rate was observed at ∼220°C, indicating a high rate of molecular evaporation corresponding to the ZnTPP powder. A few depositions were attempted with a range of temperatures between ∼210-230°C at a constant time. Determining the ideal parameters for a monolayer deposition requires a rigorous and systematic approach whereby ZnTPP was deposited at its sublimation temperature (from QCM results) for 10-15 minutes and characterised by AFM with a NuNano SCOUT 70 Si probe with a tip radius of 5 nm. Once the thickness of the layers was determined, the time of deposition and/or deposition

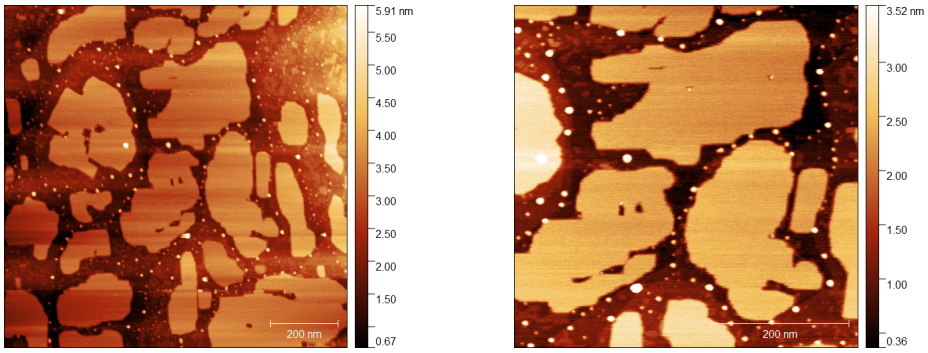

(a) (b)

Figure 95: AFM scans of multi-layer ZnTPP taken by Leo Forcieri. (a) 1 µm scan (b) 500 nm scan.

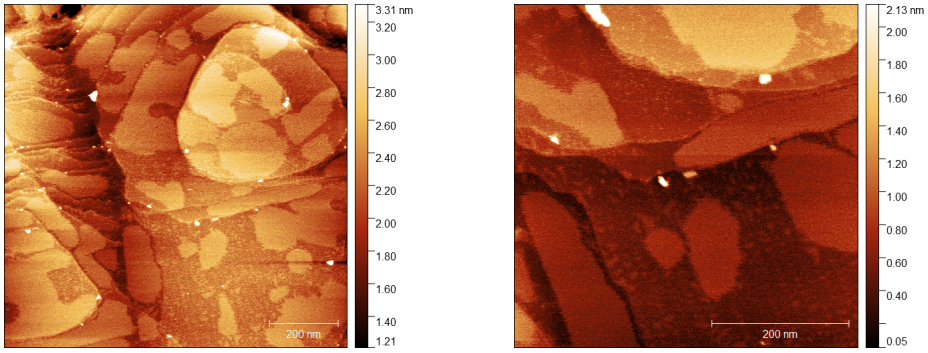

(a) (b)

Figure 96: AFM scans of mono-layer ZnTPP. (a) 1 µm scan (b) 500 nm scan.

temperature would be adjusted for optimisation.

Tetraphenylporphyrin molecules with and without the metal centre self-assemble into a stable order that resembles close to a square unit cell due to the in-plane interactions of the phenyl groups. The macrocycle will typically stay flat and lie on the surface of the substrate and has been shown in a few studies using STM.[247, 248, 249, 250]

Figure 95 shows images from the beginning of the optimisation process. The large islands formed were up to 300 nm in length and had a height of approximately 1.7 nm, strongly indicating the formation of at least a third layer or more, if we take into account the thickness of a singular porphyrin molecule should equal close to 300 pm. The porphyrin islands show some square characteristics as expected from the literature. It has been previously confirmed by STM that the second layer of ZnTPP would epitaxially form on the first layer, which indicates the growth of

more than two layers as we presumed.[250] We can visibly see the SK growth mode happening as the layers start to lose their square shape due to the sample having high molecular coverage. The perpendicular substrate-molecule interaction becomes weaker and the molecular arrangement starts to cluster as opposed to packing closely together, forming small circular islands that reached around ∼5 nm tall. It is widely believed that the governing forces that stabilise the formation of this planar network are due to intermolecular forces since the VdW forces between the substrate and the porphyrin are weaker.[247] The smaller faded islands show consistently a height of ∼0.3 nm, which indicates a single layer of porphyrin. The height of these single layers suggests that the porphyrin molecule lies planar to the surface as expected and can be deduced due to the width of the porphyrin molecule being approximately 1.4 nm.

Another point to suggest a large amount of ZnTPP was deposited is the large terraces clean gold typically presents is unclear in this sample as opposed to a submonolayer of ZnTPP deposited where the surface can be distinguished as seen in Figure 96. A previous study by Ruggieri et al. demonstrated that the gold substrate morphology is undisturbed by the addition of ZnTPP at room temperature.[248] The island sizes here reached around the same length of around 300 nm, however, they were consistently found to be between 0.3-0.4 nm tall. Au(111) terraces have a nominal height of around 0.23 nm.[251] Taking this into account, and the XPS analysis presented later, we can be sure what we are observing is molecules and not the surface substrate.

Figure 98(a) shows a high-resolution AFM image of the visibly highly ordered molecular network, where a single unit of ZnTPP can almost be seen. The molecular arrangement is represented in Figure 98(b) by space-filling models with the porphyrin macrocycle face-on and the phenyl groups rotated as the bonds naturally allow. The line selection was chosen for an area with the least amount of thermal drift and therefore, the distances between the unit cells were measured for comparison with the literature. Line profile 1 (Figure 98(c)) was taken from the top left to the bottom right and showed a distance of 1.2 nm from peak to peak on average whereas line profile 2 (Figure 98(d)) showed a dimension of 1.4 nm, on average. Line profile 2 shows a slightly larger gap than previously reported whereby the distance

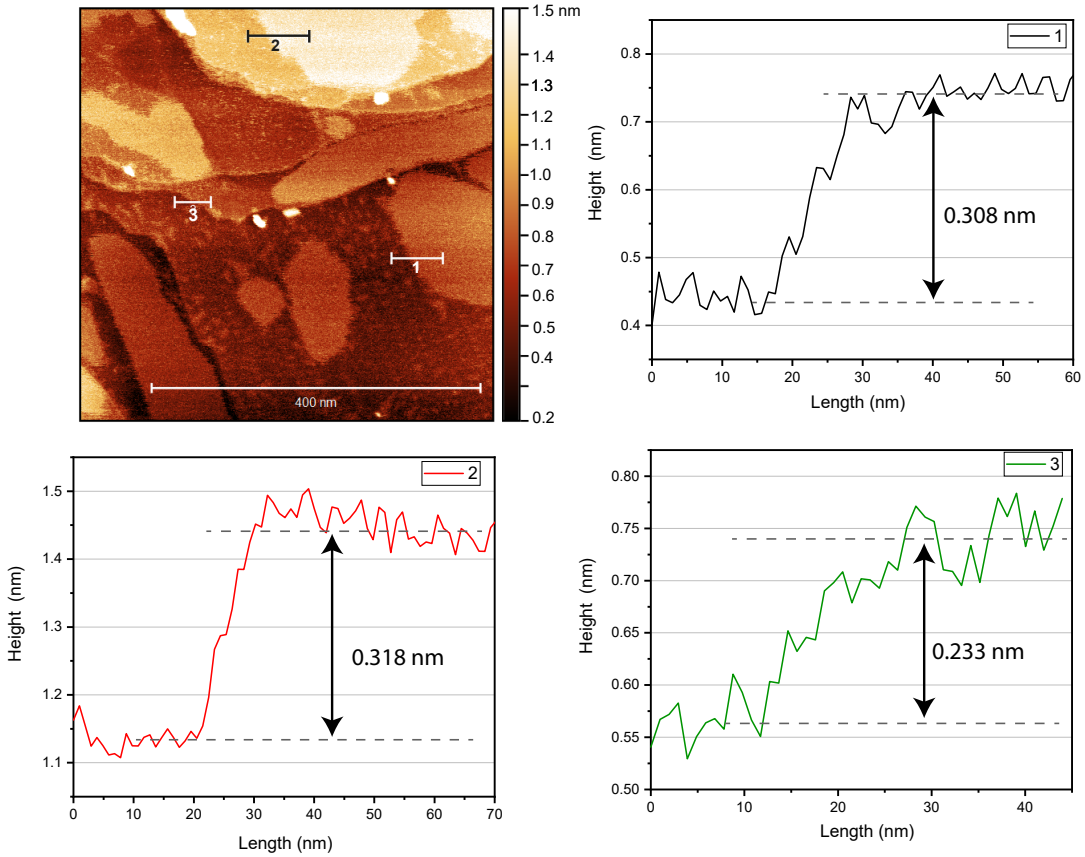

Figure 97: Line profiles of ZnTPP islands on a monolayer sample. 1 and 2 show the height of the single layer of islands at 0.309 nm and 0.318 nm, respectively. Line profile 3 shows the height of a gold terrace of the substrate, height ∼0.233 nm.

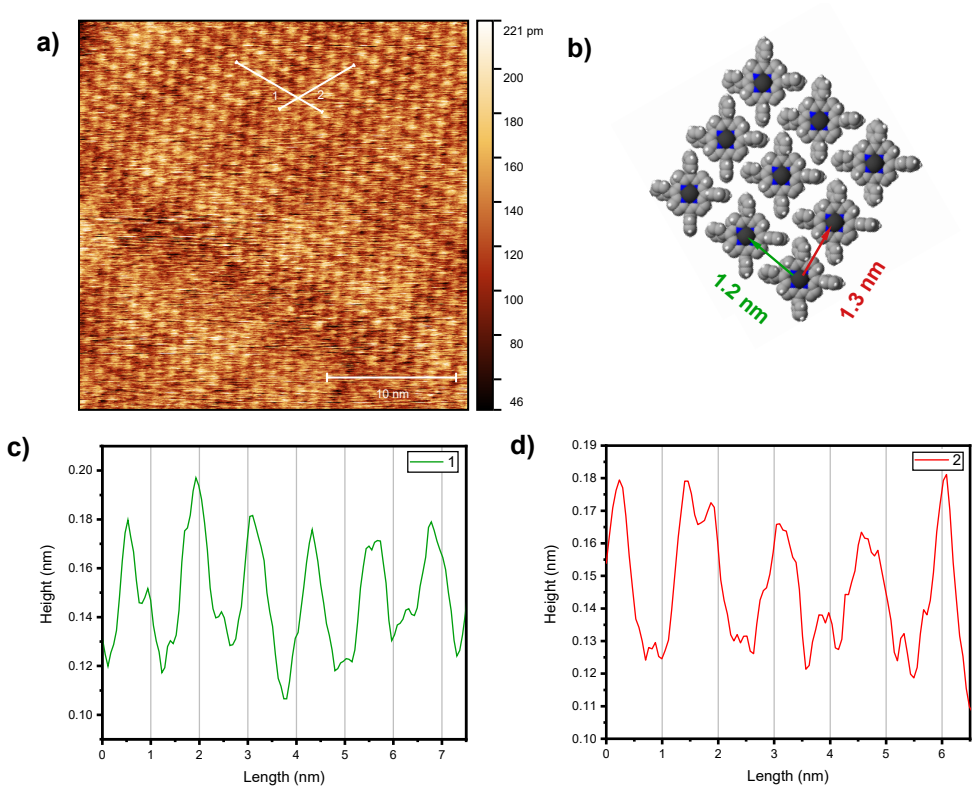

Figure 98: (a) 30 nm scan on top of a ZnTPP island showing the square units of the pophyrin network image scanned by Leo Forcieri. (b) Space-filling models ZnTPP molecular arrangement adapted from Zhang et al.[247] (c) Line profile 1 and (d) Line profile 2.

is typically found to be 1.3 nm.[248, 247] This indicates that the thermal drift runs parallel to line profile 2.

7.3 Thermal Evaporation of BipyOPE3 UHV

After optimisation of the ZnTPP layer, we began to experiment with BipyOPE3. First, the sublimation temperature of the molecule had to be checked by QCM and deposition time had to be estimated. The QCM data is shown below in Figure 99. Following the procedure for optimising the ZnTPP monolayer, the final parameters were BipyOPE3 was deposited for 15 minutes at a sublimation temperature of 75°C.

The following scans show BipyOPE3 deposited on sputtered and annealed Au(111) (Figure 100). As the scan size decreases, BipyOPE3 becomes more visible and appears to arrange in a linear formation. Figure 100c and 100d show some kind of

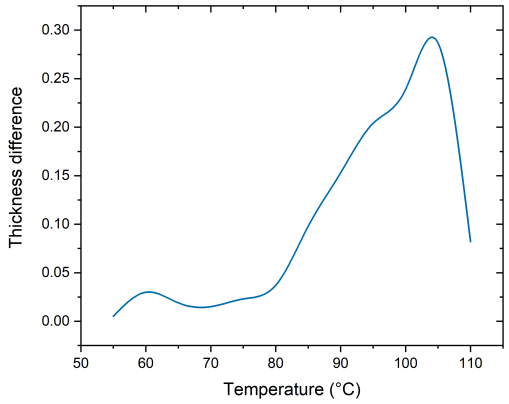

Figure 99: QCM rate of BipyOPE3 deposition in UHV. The difference in thickness against the temperature of the crucible, shown by the thermocouple.

artefact which shows that the height is inverted. We know this only inverted the height and that the features on the surface were not affected as Figure 100b and 100c are taken at very similar scan sizes which, in both cases, show the evidence of bipyridine assembling on the surface.

Figure 101(a) shows a 180 nm scan with relevant line profiles across the molecules. The height of these 'stripes' from the gold substrate range between 0.15-0.2 nm. This strongly indicates that the phenyl groups of the bipyridine molecule are lying flat on the gold surface and not standing upright as expected when self-assembling in solution. The molecular length of a fully extended BipyOPE3 molecule is calculated to be 1.6 nm from the centre of one nitrogen atom to the centre of other nitrogen.[87] The dimensions of BipyOPE3 are shown in Figure 101(b). From this, we can deduce both nitrogen atoms interact with the gold substrate and is likely to be from VdW forces due to the geometry of the nitrogen atom.

Measuring the length between peak to peak shown in the line profiles in Figure 101(c) and (d), we can deduce that gap between each 'stripe' is approximately 4 nm. If we presume that the length of the bipyridine molecule from the nitrogen atom on the phenyl ring to the nitrogen atom on the opposing side to be $\sim$ 1.6 nm, we can assume that each line represents two bipyridine molecules attached together end-to-end, equating to approximately be 3.2 nm across, not accounting for the interacting forces between the two molecules. As these images have not compensated for the thermal drift, it is also possible that the true value between the peaks lies closer to

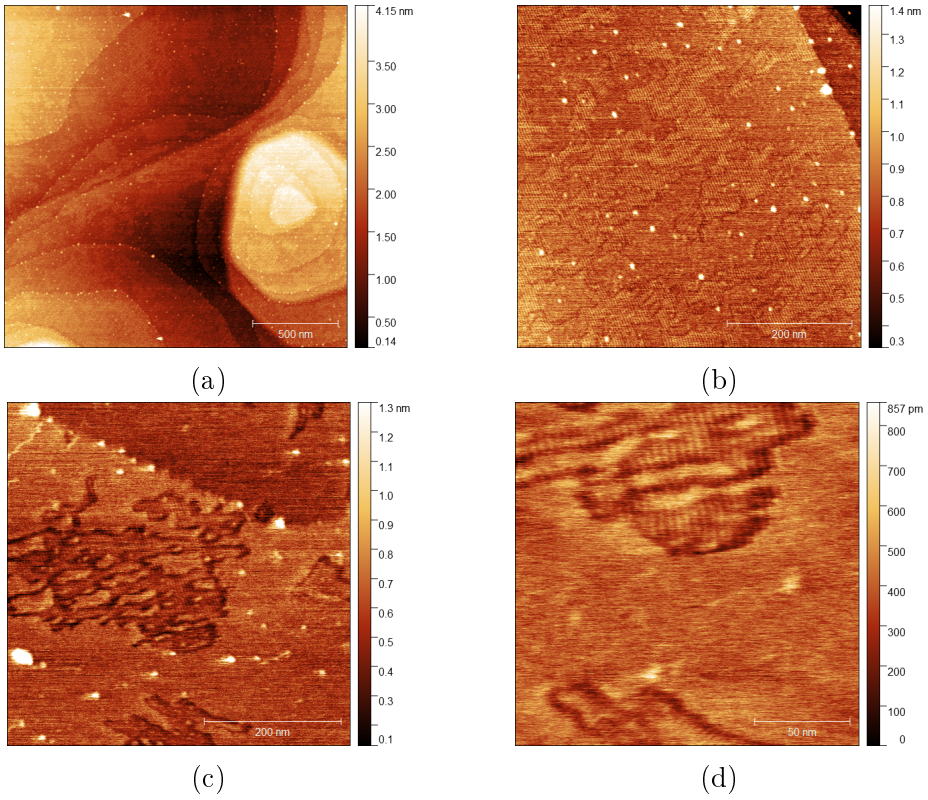

Figure 100: AFM scans of mono-layer BipyOPE3 on Au(111). (a) 2 µm scan, (b) 550 nm scan, (c) 500 nm scan and (d) 180 nm scan.

3.2 than measured.

The assembly pattern of BipyOPE3 is not well studied in vacuum, however, is more commonly found in the field of SAMs and molecular junctions.[174, 252, 69] In contrast to thermal deposition, the bond formation found in these papers reports the molecule standing upright where only one of the nitrogen atoms bonds to the gold surface. We return to a detailed description of OPE3-Au(111) binding in the next section.

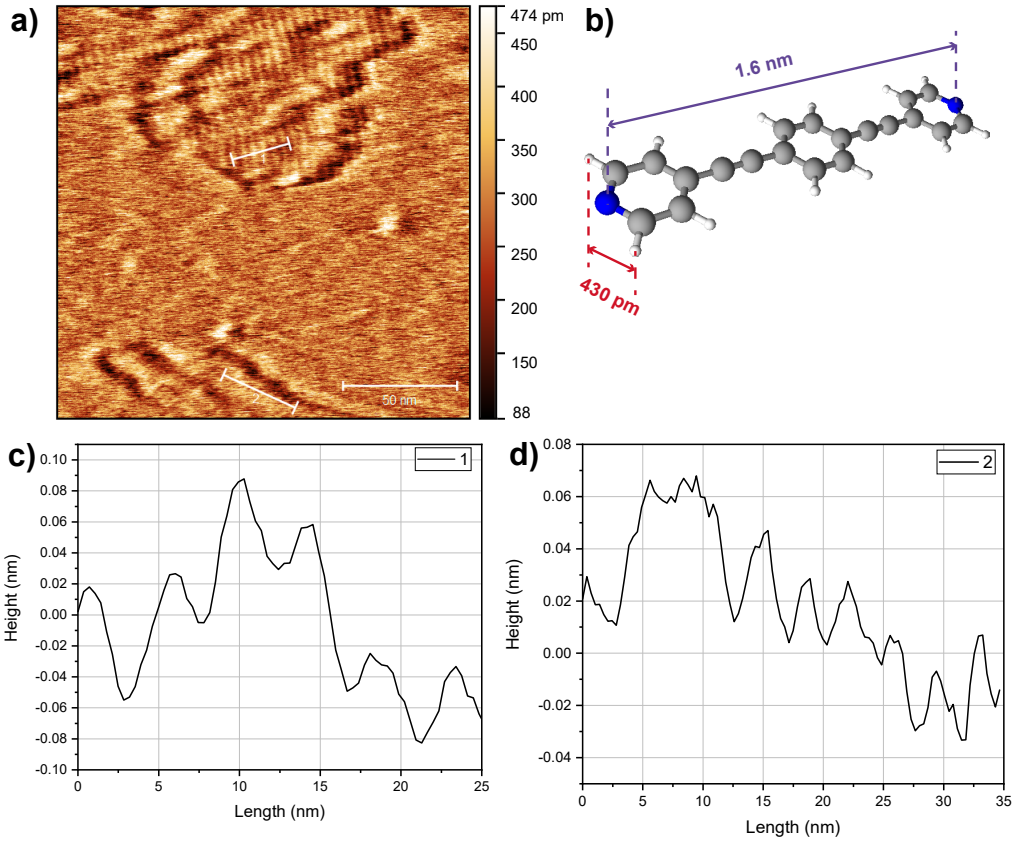

Figure 101: (a) 180 nm scan of BipyOPE3 showing the location of line profile 1 and 2 (b) Ball and stick structure of BipyOPE3 and the calculated length and width (c) Line profile 1 and (d) Line profile 2.

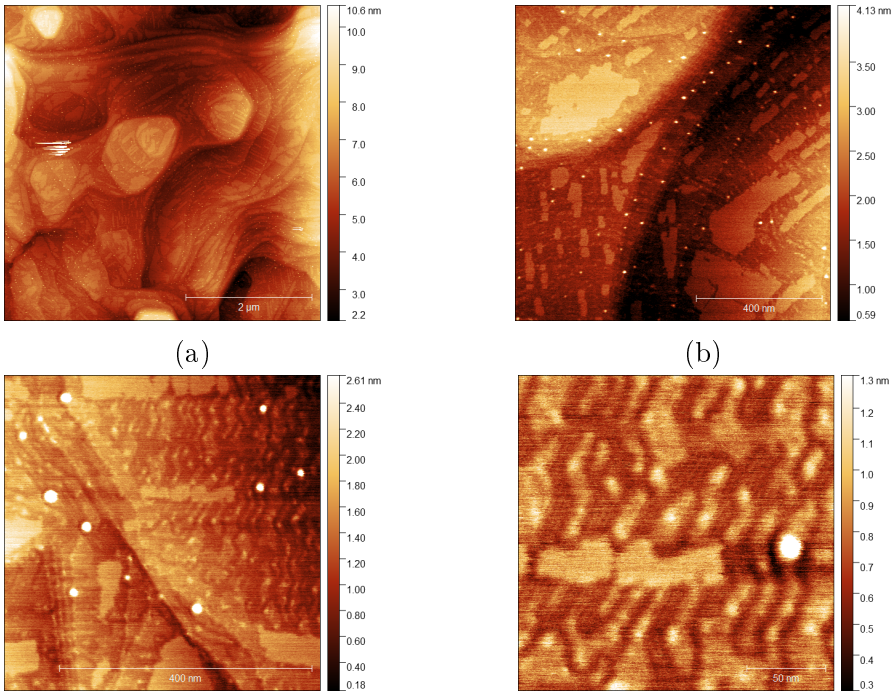

Figure 102: AFM scans of BipyOPE3 on ZnTPP Au(111). (a) 5 µm scan, (b) 850 nm scan, (c) 500 nm scan and (d) 200 nm scan.

7.4 Layer-by-layer Assembly of ZnTPP and BipyOPE3

7.4.1 Thermally Evaporated ZnTPP with Thermally Evaporated BipyOPE3

After achieving monolayers of both molecules, to form a complex (Figure 93), BipyOPE3 was deposited shortly after forming a monolayer of ZnTPP, both deposited via thermal sublimation. The results are shown in Figure 102. The larger scans show clearly the gold terraces, indicating the amount deposited was not too much.

At larger scan sizes of 850 nm, the typical characteristics of ZnTPP islands can be recognised. These islands were similar sizes to the islands observed on a monolayer of ZnTPP, between 20 nm and 300 nm. As we approach 500 nm and less scan size, the striped characteristic of BipyOPE3 can be seen sitting between the ZnTPP islands. The length from peak to peak is in line with previous results ~4 nm separation with heights at 15 pm.

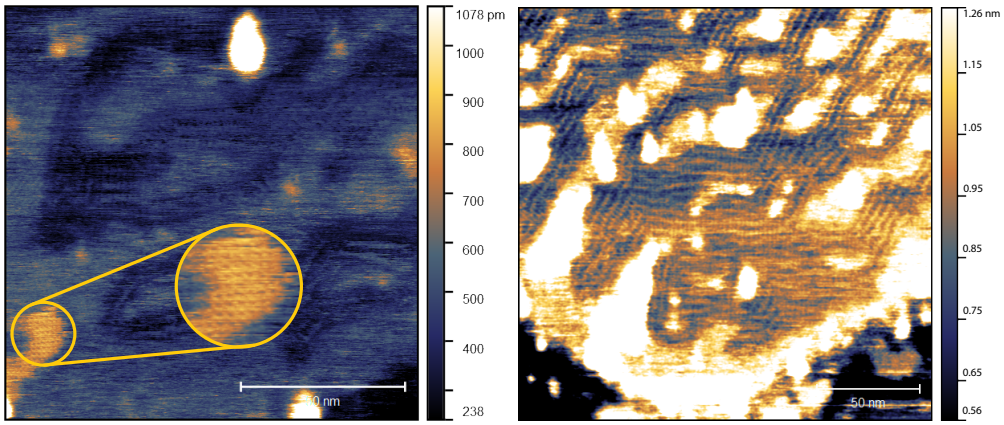

(a) (b)

Figure 103: 120 nm AFM scan of ZnTPP + BipyOPE3 in contrasting colours to highlight (a) the ZnTPP network on the surface (b) the bipyridine formation on the surface. Data courtesy of Leo Forcieri.

Figure 103 shows high-resolution scans of both molecules, highlighting the network of (a) ZnTPP and (b) BipyOPE3. The bottom left of Figure 103(a) displays the square porphyrin network as seen on a monolayer of ZnTPP. Figure 103(b) supports the theory of the packing order mentioned in the previous section, displaying the distinct stripes with ∼4 nm peak-to-peak distance as expected. Along the stripes, smaller distinct lines are visible in a perpendicular orientation to the stripe. A visual representation of this is displayed in Figure 104. Following the optimised geometry of an Au(111) surface found in Izzaouihda's work, here we reconstruct the surface to attempt to explain the packing formation.[253] Each BipyOPE3 molecule was placed onto adsorption sites common for gold surfaces, top, bridge or hollow sites.[254] The figure shows two large circles (pink and green) encompassing two different ways in which the bipyridine could pack. The arrangement of the bipyridines shows that if they are likely to pack as a couple, for example, if column 1 is packed with column 2 (and 3 with 4), the peak-to-peak distance from the middle of the two is found close to 4 nm. The troughs of the line profile are assumed to be due to the larger distance between the bipyridine pair. Through AFM analysis, it is assumed that the gap between the horizontal bipyridine molecules is between 1.5 nm to 2 nm apart. Taking into consideration the width of the molecule, which is approximately 430 pm, we assume that BipyOPE3 has a tendency to pack in formations of 3 or 4 as shown in the figure.

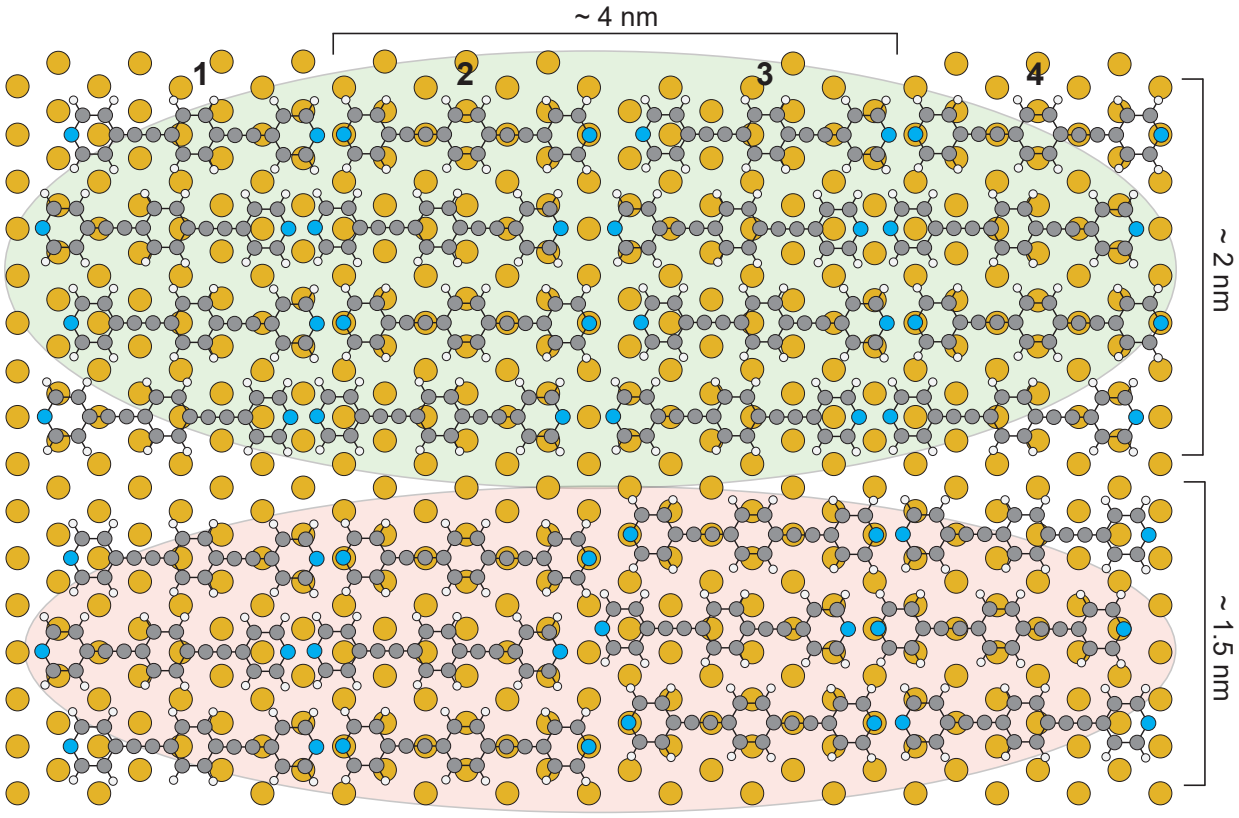

Figure 104: Two possible packing formations of BipyOPE3, shown in the green and pink ovals, overlayed on an Au(111) substrate. Green oval: BipyOPE3 aligned at the nitrogen anchor groups. Pink oval: staggered packing where the nitrogen atoms are misaligned. (Yellow circles represent gold atoms, grey circles are carbon atoms, blue atoms show the nitrogen atoms and white circles are hydrogen atoms.)

Within the green oval, the bipyridines are packed in a way where the nitrogen atoms are aligned with each other and show four rows of bipyridine which would approximately be 2 nm wide. The pink oval shows a possible conformation where the bipyridine pairs are staggered across three different columns which would represent ~1.5 nm.

Both components are clearly visible and show no evidence of interacting with each other. Following the evidence of both ZnTPP and BipyOPE3 being deposited, the main challenge was to overcome the phase separation of the two molecules and encourage complexation between the zinc and nitrogen. As the study from Isvoranu suggests, depositing the pyridine on a warm substrate, around 190°C, could provide the molecules with enough activation energy to interact. Thus, we then experimented with post-annealing the substrate in vacuum after deposition.[128]

After all options for vacuum deposition was exhausted, including post-annealing with

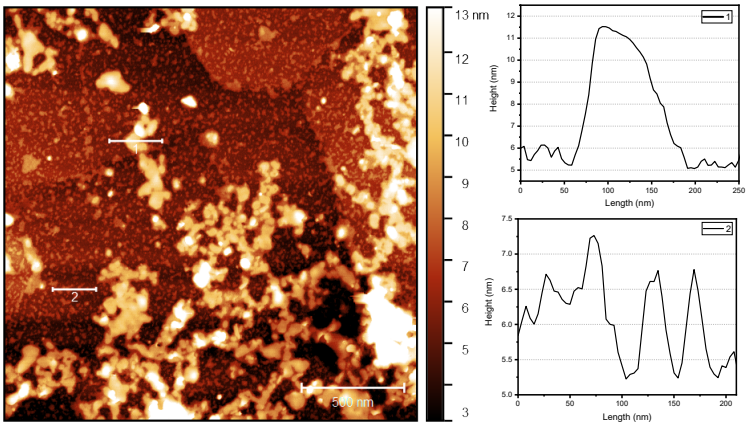

Figure 105: 2 µM AFM scan of a monolayer of ZnTPP deposited in UHV and immersed in a solution of BipyOPE3 for following deposition.

no significant findings, we attempted to self assemble a monolayer of BipyOPE3 in solution after initially putting down a layer of ZnTPP in vacuum.

7.4.2 Thermally Evaporated ZnTPP with Solution Self-Assembly Growth of BipyOPE3

To overcome the phase seperation observed in the previous section, we tested second layer deposition of OPE using solution self-assembly. The challenge when combining these two methods of deposition lies in keeping the highly ordered thermally grown ZnTPP template layer undisturbed by the solvent needed for self assembly. Much of this section includes experimenting with various solvents for a range of deposition times and characterising with XPS.

Figure 105 shows the self-assembly of BipyOPE3 following the formation of a ZnTPP monolayer on a gold substrate and the two corresponding line profiles attached. The solvent used here was toluene with a concentration of 1 mmol.

The heights of these newly formed islands are around 6 nm to 14 nm high (line profile 1). There becomes no evidence of the well-ordered ZnTPP as before. The smaller islands are 1.3 - 2 nm tall which we can either attribute to a cluster of standing bipyridines or a cluster of ZnTPP molecules. Nonetheless, it is clear that there becomes a non-uniform layer of what we assume to be a mixture of ZnTPP and bipyridine. Ideally, this sample would have been placed for characterisation in XPS to confirm the presence of both molecules.

Vacuum and vacuum deposition and vacuum and solution deposition pose two different challenges which would need overcoming to achieve the final desired junction. With both molecules thermally deposited there is clear evidence through AFM imaging that both molecules are present on the surface and both appear to have a stronger affinity to the gold substrate rather than each other. To counteract this, the second method of deposition after depositing the initial ZnTPP layer was to encourage the bipyridine to complex to the monolayer through self-assembly. From this method, characterisation through AFM showed that the solution phase disturbs the well-ordered layer put down and the sample is non-consistent.

7.5 Thermally Evaporated ZnTPP with Solution Self-Assembly Growth of BipyOPE2

After many trials and errors in attempting to facilitate the complexation between the nitrogen and the zinc centre, BipyOPE2 was chosen for experimentation instead. This molecule was chosen as it is smaller in size which would help movement in solution and have shorter deposition times in order to form well-ordered SAMs. In addition to this, it holds the same functional anchor groups as previously experimented molecules do. The shorter deposition times will be beneficial as we hope that it would leave less time to disturb the porphyrin monolayers. As we did with ZnTPP and BipyOPE3, first the ZnTPP layer was thermally deposited onto Au(111) and subsequently placed in a solution of BipyOPE2 with a 4:1 mix of ethanol: toluene for 20 minutes.

Again, we see here no clear evidence of ZnTPP islands, however, the sample appears more uniform than previous results observed with BipyOPE3. The heights of the peaks visible ranged between 300 to 900 pm. A scratch test was performed showing the heights from the substrate to the highest peaks were 1.1 nm and considering the length of BipyOPE2 is 1 nm, this strongly suggests that the molecules are bound to the gold through the nitrogen motif. As nothing conclusive can be determined through these images, further characterisation is needed to confirm the presence of ZnTPP and BipyOPE2.

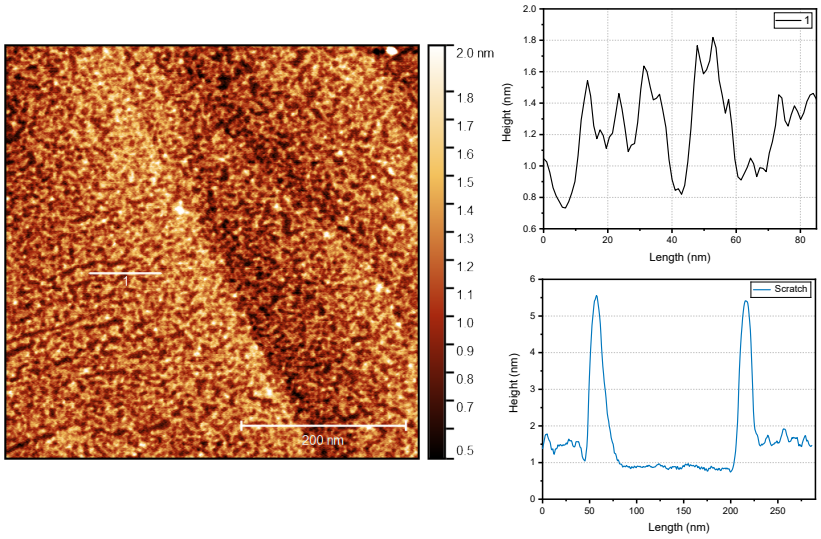

Figure 106: 500 nm AFM scan of a monolayer of ZnTPP deposited in UHV and immersed in a solution of BipyOPE2 for following deposition. Top right: Line profile of the corresponding line in the AFM image. Bottom right: Line profile of a nanoscratch image showing the thickness. (Scan not shown.)

7.5.1 XPS Characterisation of N-Zn Metal Organic Binding

Following these results, the XPS was used as a tool to check the binding between the zinc centre and nitrogen. Samples were then fabricated with a change in the BipyOPE2 deposition method each time. Various deposition times and solvents for washing were tested to encourage the ZnTPP monolayer to remain on the surface. The binding energies found for Zn $2p_{3/2}$ and N 1s are summarised in Table 7.1.

Here, the notations are as follows (THF)EtOH represents solutions of ethanol mixed with 0.2 mL of THF and 4.8 mL of ethanol. For the samples which do not state a deposition time, the samples were immersed for 20 minutes. Where the label is THF + EtOH, the mix is 1:4 ratio for the solvent. By decreasing the volume of THF, we hoped that the ZnTPP layer would be less likely to react with the THF molecules. The results show that all samples made contained some amount of ZnTPP due to the peaks arising in the Zn 2p region. The majority of the methods gave a Zn $2p_{3/2}$ peak close to 1022.0 eV indicating no significant changes were made to the structure of the ZnTPP layer. Comparing the emissions found from Chapter 6, evidence of zinc complexing to nitrogen should typically lie at approximately 1021.5 eV. Here, the sample submerged in (THF)EtOH gave the closest emission to a Zn-N bond at

Table 7.1: Table of samples involving ZnTPP and BipyOPE2 and the corresponding binding energy peaks for Zn 2p region and N 1s region.

	Sample Info	**Zn $2p_{3/2}$ (eV)**	**N 1s (eV)**
Reference	ZnTPP Monolayer	1022.10	400.05
Times	30 sec	1021.77	399.99
	1 min	1022.10	399.95
	5 min	1021.96	400.08
	20 min	1021.69	399.24
	1 hr	1022.00	401.41
	1 hr (control)	1022.25	400.38
Washes	THF + EtOH	1021.98	400.10
	None	1021.67	399.79
	EtOH	1021.90	400.07
	(THF)EtOH	1021.99	399.80
Solvents	(THF)EtOH	1021.56	399.80
	THF + EtOH	1022.07	400.10
	EtOH	1022.18	399.88

1021.56 eV. The N 1s peak lies within the range of all other samples prepared.

7.6 Optimising FePc Monolayer

Firstly, the procedure for depositing a single monolayer of FePc was optimised by a trial and error method as mentioned above for ZnTPP. FePc was deposited at a temperature of 275°C for 10 minutes. Similar to the literature, the sample was then annealed to arrive at a single layer of FePc, utilising the different desorption temperatures of multilayers and monolayers. Figure 107 shows the results of this process.

FePc typically forms close-packed islands on metals, similar to ZnTPP. FePc has been observed by STM and has been found to have high mobility on an Au(111) surface.[255] The four lobes of the FePc lie parallel to the metal surface with a protrusion at the centre. At around a third of a monolayer, the adsorbed FePc molecules are dispersed across the Au(111) substrate, suggesting a long-range repulsive molecule-molecule interaction mediated by the substrate surface.[256] The bond between the Au substrate and the FePc macrocycle is largely dominated by Van der Waals interactions although previous studies have shown that a weak chem-

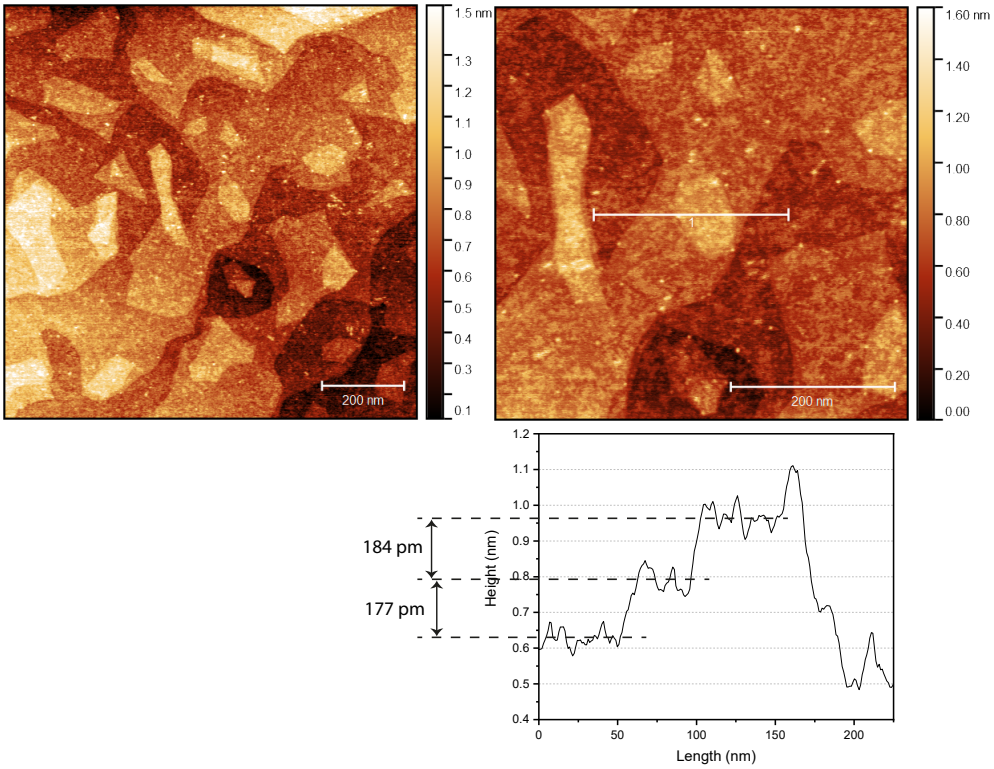

Figure 107: 1 µM (left) and 500 µM (right) AFM scan of a FePc monolayer.

ical bond forms between the iron core and Au substrate.[246]

Metal phthalocyanines can conform to a planar or non-planar shape depending on the metal centre of the molecule. For example, metals such as Sn and Pb have a large atomic area, which does not completely fit into the centre of the Pc skeleton, resulting in a non-planar molecule. Iron is smaller in size and hence is considered a planar molecule.[257] The thickness of FePc is thinner than that of ZnTPP and was measured to be around just less than 200 pm. We can deduce this from the line profile shown in Figure 107, as the height of Au(111) steps equal to 230 pm.

7.7 Combining FePc + BipyOPE3

After optimising the FePc monolayer, similar methods were used to self-assemble BipyOPE3 onto the surface. Here, BipyOPE3 was dissolved in a solution of THF and ethanol, 1:4 mix. The deposition times were varied and placed in the XPS to monitor the Fe 2p and N 1s region to confirm the presence of FePc islands, shown in Figure 108 and 109. As it can be seen, as the deposition times become longer, the intensity of both Fe 2p and N 1s peaks drops. This indicates that the solvent is

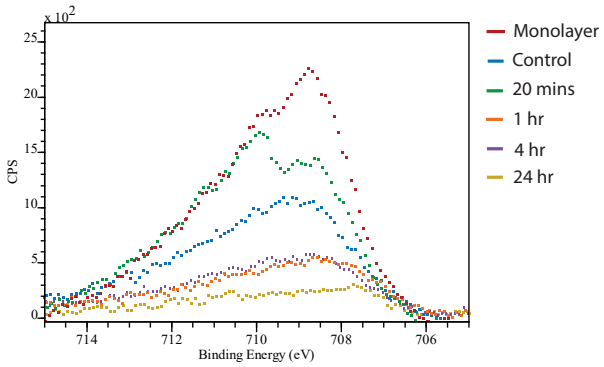

Figure 108: XPS spectra of the Fe 2p region of FePc + BipyOPE3.

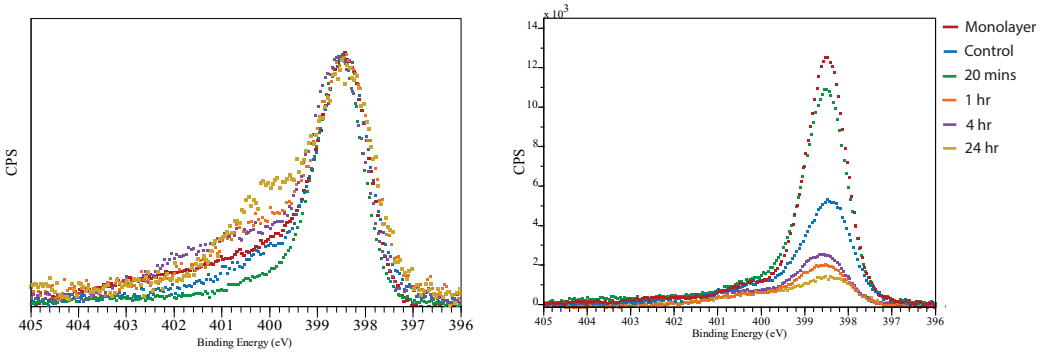

Figure 109: XPS spectra of the N 1s region of FePc + BipyOPE3. Left: normalised peaks, right: spectra adjusted to the same scale.

gradually removing the FePc monolayer as we immerse the substrate in the solvent. As the nitrogen on the surface is also decreasing, this suggests a little to no amount of BipyOPE2 is binding to the gold surface. Following the study by Isvoranu, the Fe 2p peak should become significantly narrower as evidence of nitrogen complexing to Fe.

In these particular cases, the total full width at half-maximum (FWHM) of the Fe $2p_{3/2}$ signal of a FePc monolayer lies at approximately 4.3 eV, decreasing to 4.1 eV at 4 hour deposition and then increasing to 4.8 eV at 24 hours. With no significant reduction after exposure to bipyridine, this suggests no successful complexation occurring.

Figure 109 shows two spectra in the N 1s region, the spectrum on the left shows normalised peaks found in the N 1s region and the spectrum on the right is scaled to the same CPS. Typical N 1s spectra of pyridine adsorbed onto an iron centre of FePc should produce three different emissions at ∼398, ∼399 and ∼400 eV due to photoemission from the nitrogen atoms within the Pc skeleton, nitrogen atoms of the

multilayer of BipyOPE3 and bonding to sites other than Fe and finally, an emission from nitrogen atoms coordinating with Fe, respectively.[128] Here, the nitrogen peak emission for nitrogen atoms within the Pc macrocycle arose at 398.70 eV.

As we begin to expose the FePc layers to BipyOPE3, changes in the N 1s spectra appear after deposition of around 4 hours. With the deposition of 4 hours, two additional peaks arise at 399.96 and 401.04 eV. These values closely match the values found in the literature, indicating that there is some presence of bipyridine interacting with the iron.[246, 128] However, the shape of the Fe $2p_{3/2}$ does not significantly change, suggesting the amount of FePc on the surface is insufficient to produce the expected narrower shape. At 24 hours, there appear to be fewer FePc molecules on the surface as observed from the Fe 2p XPS results. Similar to 4 hr deposition, the peaks arising in the N 1s region at 24 hours appeared at 398.62, 399.42 and 400.52 eV. The amount of FePc left on the gold surface after 24 hours was less than half of that found at 4 hours.

7.8 Combining FePc + BipyOPE2

The solvents and methods used for depositing BipyOPE2 were the same as 1, a THF:EtOH mix of 1:4. Similar results were discovered at 4 hours and 24 hours in the N 1s region when combining FePc and BipyOPE2 (Figure 110). At 4 hours, three distinct energy emissions were found at 398.8, 399.1 and 400.2 eV, which are aligned with the literature as stated previously. The area ratio between the nitrogen atoms found in the macrocycle compared with the Fe-N bonds was approximately 2:1, indicating about half of the FePc molecules left on the surface after solution self-assembly had interacted with the nitrogen of the bipyridine.

As we found with BipyOPE3 samples, the FWHM of the Fe 2p peak for depositions between 20 minutes, 1 hour and 4 hours are 4.2, 4.8 and 4.4 eV, respectively. As we reach 24 hours, the FWHM decreases to 3.4 eV, this could indicate some level of decoupling is occurring between the FePc and the pyridine moiety. Expected FWHM suggests a narrowing of at least half of the original monolayer value to $\sim$1.75 eV. Interestingly, the difference in intensity does not differ between each sample except for the monolayer and the 24-hour sample indicating that as the self-

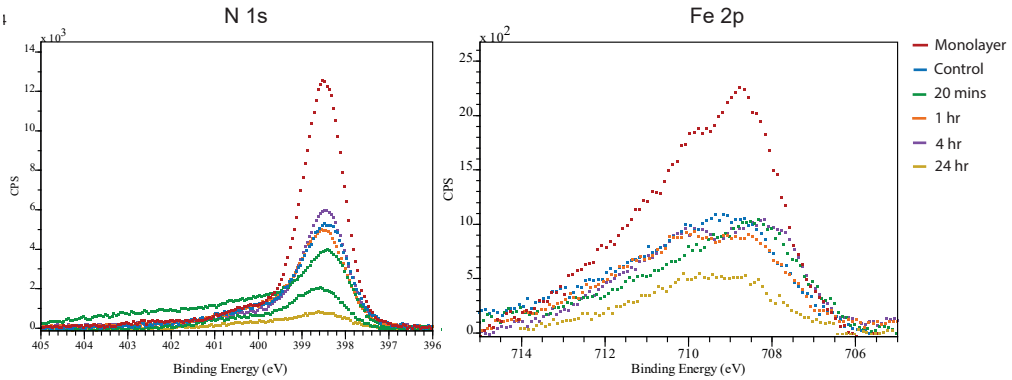

Figure 110: XPS spectra of the N 1s (left) and Fe 2p region (right) of FePc + bipyridine 1

assembly deposition time increases the FePc monolayer is not greatly affected until we reach a time between 4 to 24 hours. At 24 hours, there appear to be fewer FePc molecules remaining on the surface, which is in line with previous results.

Considering some of the evidence found for 24-hour deposition of BipyOPE2, such as the additional peaks found in the N 1s spectra combined with the evidence of Fe 2p narrowing by 0.9 eV, shows the initial stages of complexing happening. To further confirm this theory, additional experiments need to be carried out to prevent damage to the FePc monolayer after 24 hours of submersion in solvent.

7.9 Summary of Findings and Future Work

We have confirmed through AFM, ZnTPP and BipyOPE3 can form highly-ordered networks on an Au(111) surface via thermal sublimation on separate occasions. The challenge we had here was to encourage the SAM formation of bipyridine to interact with the substrate upright as opposed to both nitrogen atoms on the surface. This in turn affected the ability for complexation to occur and caused a phase separation between the two molecules.

To attempt to overcome this problem, BipyOPE3 was deposited in solution as past studies on BipyOPE3 showed upright standing packing formation of the SAMs. However, as longer deposition times were required for the packing of BipyOPE3 due to the length of the molecule, AFM showed disruption to the pristine ZnTPP monolayer whilst simultaneously depositing BipyOPE3 upright. The following steps

were taken to prevent the removal of the ZnTPP layer. First, limiting the deposition time in solution by experimenting with a smaller bipyridine molecule would mean less time for the solvent to interact with the bottom surface layer. During experimentation with BipyOPE2, a large amount of characterisation was performed using an XPS to confirm the presence of a Zn-N bond. There had been evidence of one sample exhibiting a peak emission at 1021.56 eV, indicative of a Zn-N bond. Ideally, this sample will be replicated for AFM characterisation and further characterisation if successful.

Alternatively, FePc was swapped out from ZnTPP following Isvoranu's studies on pyridine and ammonia adsorption onto FePc. Experiments in these studies were performed in a vacuum as opposed to vacuum and solution. As we discovered through XPS, the longer the deposition time of BipyOPE3, the weaker the Fe $2p_{3/2}$ signal becomes, indicating the decrease in FePc molecules left on the substrate. In contrast to this, BipyOPE2 appears to retain the FePc molecules at similar intensities at 20 mins, 1 hour and 4 hours showing that the deposition time for FePc here is not the limiting factor, but potentially the solvent used was the problem.

Next, we would have liked to continue this work with a few more experiments to confirm the complex formation between the metal centre and the nitrogen of the linker above. As evident from the results produced in this chapter, following vacuum deposition the immersion in solvent disturbs the pristine monolayer formed by sublimation. Part of the reason for this is as the planar molecule interaction to the surface is from the pi system, the molecule is physisorbed onto the substrate. As we had used THF to dissolve the bipyridine derivates, we suspect that THF is flat enough to come in between the porphyrin or phthalocyanine molecule, lifting it off the surface of the substrate. To test this theory, we had intended to use various non-planar solvents for the solution self-assembly. For example, MeTHF and acetone both contain sp3 hybridised carbon atoms preventing a planar structure. This can be proved successful by examining the resulting samples by XPS and analysing the binding energies.

Another advantage of using MeTHF as an alternative to THF is that it is derived from plant sources (corncobs and bagasse) making it a both economical and envi-

ronmentally friendly substitute. Its production method also provides further environmentally options as there is lower peroxide formation and ease of separation and recovery from water which reduces the waste stream, to name a few.[258]

Chapter 8

Conclusions

As outlined earlier in this work, the three aims of this thesis was to translate single molecular measurements to monolayers and examine their feasibility, experiment with phonon suppressing molecules to measure the impact on its thermoelectric/electric properties and to design a novel method of fabricating thermoelectric thin films.

Chapter 5 experiments with two derivatives of ferrocenes: thiol and pyridyl ferrocenes. The molecules of choice were based on ferrocene derivatives which were previously studied as single molecular junctions (outside the scope of this work). These molecules assembled well on the Au surface with nitrogen-based molecules assembling in a 'hairpin' conformation. Thiol-based molecules tended to prefer an 'open' conformation. In addition to successfully forming a self-assembled layer, it was discovered that the angle between the arms will effect the thermoelectricity despite not significantly impacting the conductivity.

The fabrication of these novel 'sticky' to 'slippery' linker systems presents a significant breakthrough in the field of molecular electronics, overcoming the need for rigid contacts to metallic electrodes, a critical step in the design of future thin-film devices. Chapter 6 demonstrates the use of stacking two molecules to disrupt the phonon transport through the device to in turn enhance the thermoelectric properties. This study could also reasonably be extended to further work in tailoring different ends of a multi-component system to different materials, as a route toward decoupling

electronic and thermal contributions in the generation of thermopower.

The following chapter, Chapter 7, then took this a step further by using a novel method of attempting to create multi-component systems by combining thermal sublimation and self-assembly. The results discussed in this chapter have shown that there is potential for bipyridine to complex onto the iron core of FePc. Although this study didn't achieve what it was set out to do, the findings confirmed that good progress has been made towards a novel fabrication method for thin film thermoelectrics.

Bibliography

[1] Jian He and Terry M Tritt. *Advances in thermoelectric materials research: Looking back and moving forward*. 2017.

[2] Jing Jing Feng, Wei Zhu, and Yuan Deng. *An overview of thermoelectric films: Fabrication techniques, classification, and regulation methods*. 2018.

[3] Timothy G Gutowski et al. "The energy required to produce materials: Constraints on energy-intensity improvements, parameters of demand". In: *Philosophical Transactions of the Royal Society A: Mathematical, Physical and Engineering Sciences* 371.1986 (2013).

[4] Grégoire Wallenborn. "Rebounds Are Structural Effects of Infrastructures and Markets". In: *Frontiers in Energy Research* 6.October (2018), pp. 1–13.

[5] Zhaoxia Luo et al. "System thermal analysis for mobile phone". In: *Applied Thermal Engineering* 28.14-15 (2008), pp. 1889–1895.

[6] Reynir Atlason and Runar Unnthorsson. "Ideal EROI (energy return on investment) deepens the understanding of energy systems". In: *Energy* 67 (2014), pp. 241–245.

[7] Hee Seok Kim et al. "Relationship between thermoelectric figure of merit and energy conversion efficiency". In: *Proceedings of the National Academy of Sciences of the United States of America* 112.27 (2015), pp. 8205–8210.

[8] Lauryn L. Baranowski, G. Jeffrey Snyder, and Eric S. Toberer. "Concentrated solar thermoelectric generators". In: *Energy and Environmental Science* 5.10 (2012), pp. 9055–9067.

[9] R. P. Feynman. "There's Plenty of Room at the Bottom". In: *Engineering and Science* 23.5 (1960), pp. 22–36.

[10] G. E. Moore. “Cramming More Components onto Integrated Circuits”. In: *Electronics* 38.8 (1965).

[11] Arieh Aviram and Mark A. Ratner. “Molecular Rectifiers”. In: *Chemical Physics Letters* 29.2 (1974), pp. 277–283.

[12] Bingqian Xu, Xiaoyin Xiao, and Nongjian J Tao. “Measurements of Single-Molecule Electromechanical Properties”. In: *Journal of the American Chemical Society* 125.52 (2003), pp. 16164–16165.

[13] Dong Xiang et al. “Molecular-Scale Electronics: From Concept to Function”. In: *Chemical Reviews* 116.7 (2016), pp. 4318–4440.

[14] Colin Van Dyck and Mark A. Ratner. “Molecular rectifiers: A new design based on asymmetric anchoring moieties”. In: *Nano Letters* 15.3 (2015), pp. 1577–1584.

[15] Devens Gust, Thomas A. Moore, and Ana L. Moore. “Molecular switches controlled by light”. In: *Chemical Communications* 11 (2006), pp. 1169–1178.

[16] Lin Qi Pei et al. “Mechanically Induced Switching between Two Discrete Conductance States: A Potential Single-Molecule Variable Resistor”. In: *ACS Applied Materials and Interfaces* 13.48 (2021), pp. 57646–57653.

[17] Ritu Gupta, Priyajit Jash, and Prakash Chandra Mondal. “Nanoscale molecular layers for memory devices: challenges and opportunities for commercialization”. In: *Journal of Materials Chemistry C* 9.35 (2021), pp. 11497–11516.

[18] H Julian Goldsmid. *Introduction to Thermoelectricity*. 2010.

[19] Mariano Campoy-Quiles. “Will Organic Thermoelectrics Get Hot?” In: *Philosophical Transactions of the Royal Society A: Mathematical, Physical and Engineering Sciences* 377.2152 (2019).

[20] Paothep Pichanusakorn and Prabhakar Bandaru. “Nanostructured thermoelectrics”. In: *Materials Science and Engineering R: Reports* 67.2-4 (2010), pp. 19–63.

[21] Achim Harzheim. *Thermoelectricity in single-molecule devices*. 2018.

[22] C M Finch, V M García-Suárez, and C J Lambert. "Giant thermopower and figure of merit in single-molecule devices". In: *Physical Review B - Condensed Matter and Materials Physics* 79.3 (2009).

[23] D. Dragoman and M Dragoman. "Giant thermoelectric effect in graphene". In: *Applied Physics Letters* 91.20 (2007), p. 203116.

[24] Charalambos Evangeli et al. "Engineering the thermopower of C60 molecular junctions". In: *Nano Letters* 13.5 (2013), pp. 2141–2145.

[25] Kumar Gaurav and Sudhir K Pandey. "Efficiency calculation of thermoelectric generator using temperature dependent material's properties". In: *Condensed Matter* (2016). arXiv: 1603.01757.

[26] Terry M Tritt. *Thermoelectrics run hot and cold*. 1996.

[27] Lanlan Sun et al. *Single-molecule electronics: From chemical design to functional devices*. 2014.

[28] D.M. Rowe. *Thermoelectrics Handbook: Marco to Nano*. 2006.

[29] N. W. Ashcroft and D. N. Mermin. *Solid State Physics*. 1976.

[30] M. Jonson and G. D. Mahan. "Mott's formula for the thermopower and the Wiedemann-Franz law". In: *Physical Review B* 21.10 (1980), pp. 4223–4229.

[31] Juan Carlos Cuevas and Elke Scheer. *Molecular Electronics: An Introduction to Theory and Experiment*. 2010.

[32] David Rowe and C Bhandari. *Handbook of Thermoelectrics*. 1995.

[33] H Julian Goldsmid. *The Physics of Thermoelectric Energy Conversion*. 2017.

[34] G. Jeffrey Snyder and Alemayouh H Snyder. "Figure of merit ZT of a thermoelectric device defined from materials properties". In: *Energy and Environmental Science* 10.11 (2017), pp. 2280–2283.

[35] Zhi Gang Chen et al. *Nanostructured thermoelectric materials: Current research and future challenge*. 2012.

[36] Yiming Zhou and Li Dong Zhao. "Promising Thermoelectric Bulk Materials with 2D Structures". In: *Advanced Materials* 29.45 (2017), p. 1702676.

[37] Mi Kyung Han et al. “Thermoelectric properties of Bi2Te3: CuI and the effect of its doping with Pb atoms”. In: *Materials* 10.11 (2017).

[38] Hilaal Alam and Seeram Ramakrishna. “A review on the enhancement of figure of merit from bulk to nano-thermoelectric materials”. In: *Nano Energy* 2.2 (2013), pp. 190–212.

[39] Jing Feng Li et al. *High-performance nanostructured thermoelectric materials.* 2010.

[40] C J Lambert. *Basic concepts of quantum interference and electron transport in single-molecule electronics.* 2015.

[41] Cronin B Vining. “An inconvenient truth about thermoelectrics”. In: *Nature Materials* 8.2 (2009), pp. 83–85.

[42] J P Heremans. “Low-Dimensional Thermoelectricity”. In: *Acta Phys. Polonica A* 108 (2005).

[43] Yonatan Dubi and Massimiliano Di Ventra. “Colloquium: Heat flow and thermoelectricity in atomic and molecular junctions”. In: *Reviews of Modern Physics* 83.1 (2011), pp. 131–155.

[44] Olga Bubnova et al. “Optimization of the thermoelectric figure of merit in the conducting polymer poly(3,4-ethylenedioxythiophene)”. In: *Nature Materials* 10.6 (2011), pp. 429–433.

[45] David G Cahill and R O Pohl. “Thermal conductivity of amorphous solids above the plateau”. In: *Physical Review B* 35.8 (1987), pp. 4067–4073.

[46] Feng-Xing Jiang et al. “Thermoelectric Performance of Poly(3,4- ethylenedioxythiophene): Poly(styrenesulfonate)”. In: *Chinese Physics Letters* 25.6 (2008), p. 2202.

[47] Magnus Paulsson and Supriyo Datta. “Thermoelectric effect in molecular electronics”. In: *Physical Review B - Condensed Matter and Materials Physics* 67.24 (2003). arXiv: `0301232 [cond-mat]`.

[48] Longji Cui et al. “Perspective: Thermal and thermoelectric transport in molecular junctions”. In: *Journal of Chemical Physics* 146.9 (2017).

[49] Colin J. Lambert and Shi Xia Liu. "A Magic Ratio Rule for Beginners: A Chemist's Guide to Quantum Interference in Molecules". In: *Chemistry - A European Journal* 24.17 (2018), pp. 4193–4201.

[50] Pramod Reddy et al. "Thermoelectricity in molecular junctions". In: *Science* 315.5818 (2007), pp. 1568–1571.

[51] Jonathan A Malen et al. "Identifying the length dependence of orbital alignment and contact coupling in molecular heterojunctions". In: *Nano Letters* 9.3 (2009), pp. 1164–1169.

[52] Supriyo Datta. *Quantum transport: Atom to transistor*. Vol. 9780521631. 2005, pp. 1–404.

[53] Alex Zevalkink et al. "A practical field guide to thermoelectrics: Fundamentals, synthesis, and characterization". In: *Applied Physics Reviews* 5.2 (2018).

[54] Kun Wang, Edgar Meyhofer, and Pramod Reddy. "Thermal and Thermoelectric Properties of Molecular Junctions". In: *Advanced Functional Materials* 30.8 (2020), pp. 1–29.

[55] G. Breit and E. Wigner. "Capture of slow neutrons". In: *Physical Review* 49.7 (1936), pp. 519–531.

[56] U Fano. "Effects of configuration interaction on intensities and phase shifts". In: *Physical Review* 124.6 (1961), pp. 1866–1878.

[57] M. P. Fok and P. R. Prucnal. "Switching based on optical nonlinear effects". In: *Optical Switches: Materials and Design*. Woodhead Publishing, 2010, pp. 181–205.

[58] Yueqi Li et al. "Gate controlling of quantum interference and direct observation of anti-resonances in single molecule charge transport". In: *Nature Materials* 18.4 (2019), pp. 357–363.

[59] N. J. Tao. "Electron transport in molecular junctions". In: *Nature Nanotechnology* 1.3 (2006), pp. 173–181.

[60] John K Tomfohr and Otto F Sankey. "Complex band structure, decay lengths, and Fermi level alignment in simple molecular electronic systems". In: *Physical Review B - Condensed Matter and Materials Physics* 65.24 (2002), pp. 1–12.

[61] Xiaoyin Xiao, Bingqian Xu, and Nongjian Tao. "Conductance Titration of Single-Peptide Molecules". In: *Journal of the American Chemical Society* 126.17 (2004), pp. 5370–5371.

[62] Myeong H. Lee, Gil Speyer, and Otto F. Sankey. "Electron transport through single alkane molecules with different contact geometries on gold". In: *Physica Status Solidi (B) Basic Research* 243.9 (2006), pp. 2021–2029.

[63] Jeremy M Beebe et al. "Contact resistance in metal-molecule-metal junctions based on aliphatic SAMs: Effects of surface linker and metal work function". In: *Journal of the American Chemical Society* 124.38 (2002), pp. 11268–11269.

[64] M. Teresa González et al. "Conductance values of alkanedithiol molecular junctions". In: *New Journal of Physics* 10 (2008).

[65] Sung Yeon Jang et al. "Interpretation of stochastic events in single molecule conductance measurements". In: *Nano Letters* 6.10 (2006), pp. 2362–2367.

[66] Latha Venkataraman et al. "Dependence of single-molecule junction conductance on molecular conformation". In: *Nature* 442.7105 (2006), pp. 904–907.

[67] Aaron Tan et al. "Effect of length and contact chemistry on the electronic structure and thermoelectric properties of molecular junctions". In: *Journal of the American Chemical Society* 133.23 (2011), pp. 8838–8841.

[68] Hongmei Liu et al. "Length-dependent conductance of molecular wires and contact resistance in metal-molecule-metal junctions". In: *ChemPhysChem* 9.10 (2008), pp. 1416–1424.

[69] Veerabhadrarao Kaliginedi et al. "Correlations between molecular structure and single-junction conductance: A case study with oligo(phenylene-ethynylene)-type wires". In: *Journal of the American Chemical Society* 134.11 (2012), pp. 5262–5275.

[70] Liang Luo and C. Daniel Frisbie. “Length-dependent conductance of conjugated molecular wires synthesized by stepwise "click" chemistry”. In: *Journal of the American Chemical Society* 132.26 (2010), pp. 8854–8855.

[71] M. Magoga and C. Joachim. “Conductance of molecular wires connected or bonded in parallel”. In: *Physical Review B - Condensed Matter and Materials Physics* 59.24 (1999), pp. 16011–16021.

[72] Constant M Guédon et al. “Observation of quantum interference in molecular charge transport”. In: *Nature Nanotechnology* 7.5 (2012), pp. 305–309.

[73] Matthias Ernzerhof, Min Zhuang, and Philippe Rocheleau. “Side-chain effects in molecular electronic devices”. In: *Journal of Chemical Physics* 123.13 (2005), p. 181103.

[74] Gemma C. Solomon et al. “Quantum interference in acyclic systems: Conductance of cross-conjugated molecules”. In: *Journal of the American Chemical Society* 130.51 (2008), pp. 17301–17308.

[75] Gemma C. Solomon et al. “Electron transport through conjugated molecules: When the π system only tells part of the story”. In: *ChemPhysChem* 10.1 (2009), pp. 257–264.

[76] Marius Bürkle et al. “First-principles calculation of the thermoelectric figure of merit for [2,2]paracyclophane-based single-molecule junctions”. In: *Physical Review B - Condensed Matter and Materials Physics* 91.16 (2015). arXiv: 1503.02134.

[77] Xintai Wang et al. “Thermoelectric properties of organic thin films enhanced by π–π stacking”. In: *Journal of Physics: Energy* 4.2 (2022), p. 024002.

[78] Hatef Sadeghi, Sara Sangtarash, and Colin J Lambert. “Oligoyne Molecular Junctions for Efficient Room Temperature Thermoelectric Power Generation”. In: *Nano Letters* 15.11 (2015), pp. 7467–7472.

[79] Mark D Losego et al. “Effects of chemical bonding on heat transport across interfaces”. In: *Nature Materials* 11.6 (2012), pp. 502–506.

[80] Qian Li et al. "A Strategy to Suppress Phonon Transport in Molecular Junctions Using π-Stacked Systems". In: *Journal of Physical Chemistry C* 121.13 (2017), pp. 7175–7182.

[81] Gediminas Kiršanskas et al. "Designing π-stacked molecular structures to control heat transport through molecular junctions". In: *Applied Physics Letters* 105.23 (2014).

[82] Linda A. Zotti et al. "Revealing the role of anchoring groups in the electrical conduction through single-molecule junctions". In: *Small* 6.14 (2010), pp. 1529–1535.

[83] Jinxuan Liu et al. "Structural characterization of self-assembled monolayers of pyridine-terminated thiolates on gold". In: *Physical Chemistry Chemical Physics* 12.17 (2010), pp. 4273–4274.

[84] Wenjing Hong et al. "Single molecular conductance of tolanes: Experimental and theoretical study on the junction evolution dependent on the anchoring group". In: *Journal of the American Chemical Society* 134.4 (2012), pp. 2292–2304.

[85] Veerabhadrarao Kaliginedi et al. "Promising anchoring groups for single-molecule conductance measurements". In: *Physical Chemistry Chemical Physics* 16.43 (2014), pp. 23529–23539.

[86] Aaron Tan, Seid Sadat, and Pramod Reddy. "Measurement of thermopower and current-voltage characteristics of molecular junctions to identify orbital alignment". In: *Applied Physics Letters* 96.1 (2010), p. 13110.

[87] Xiaotao Zhao et al. "Oligo(aryleneethynylene)s with terminal pyridyl groups: Synthesis and length dependence of the tunneling-to-hopping transition of single-molecule conductances". In: *Chemistry of Materials* 25.21 (2013), pp. 4340–4347.

[88] Fang Chen et al. "Effect of anchoring groups on single-molecule conductance: Comparative study of thiol-, amine-, and carboxylic-acid-terminated molecules". In: *Journal of the American Chemical Society* 128.49 (2006), pp. 15874–15881.

[89] Woon Kie Paik et al. "Adsorption of carboxylic acids on gold by anodic reaction". In: *Langmuir* 19.10 (2003), pp. 4211–4216.

[90] Jonathan R Widawsky et al. "Simultaneous determination of conductance and thermopower of single molecule junctions". In: *Nano Letters* 12.1 (2012), pp. 354–358.

[91] Sriharsha V Aradhya and Latha Venkataraman. "Single-molecule junctions beyond electronic transport". In: *Nature Nanotechnology* 8.6 (2013), pp. 399–410.

[92] Jacob N. Israelachvili. *Intermolecular and Surface Forces*. 2011.

[93] S.O. Kasap. *Principles of Electronic Materials & Devices*. 2018.

[94] Geoffrey A. Lawrance. *Introduction to Coordination Chemistry*. 2010, pp. 1–290.

[95] Vasishta Bhatt. *Essentials of Coordination Chemistry: A Simplified Approach with 3D Visuals*. 2015, pp. 1–269.

[96] Arthur W. Adamson and Alice P. Gast. *Physical Chemistry of Surfaces*. Vol. 6th Ed. 1. Wiley, 1997, p. 808.

[97] J. Christopher Love et al. *Self-assembled monolayers of thiolates on metals as a form of nanotechnology*. Vol. 105. 4. 2005, pp. 1103–1169.

[98] Johannes V. Barth, Giovanni Costantini, and Klaus Kern. "Engineering atomic and molecular nanostructures at surfaces". In: *Nature* 437.7059 (2005), pp. 671–679.

[99] Christian Joachim and Mark A Ratner. "Molecular electronics: Some views on transport junctions and beyond". In: *Proceedings of the National Academy of Sciences of the United States of America* 102.25 (2005), pp. 8801–8808.

[100] G E Poirier and E. D. Pylant. "The self-assembly mechanism of alkanethiols on Au(111)". In: *Science* 272.5265 (1996), pp. 1145–1148.

[101] Abraham Ulman. "Formation and structure of Self-Assembled Monolayers". In: *Chem. Rev.* 96 (1996), pp. 1533–1554.

[102] Frederik Tielens and Elizabeth Santos. "AuS and SH bond formation/breaking during the formation of alkanethiol SAMs on Au(111): A theoretical study". In: *Journal of Physical Chemistry C* 114.20 (2010), pp. 9444–9452.

[103] Nora Gonzalez-Lakunza, Nicolás Lorente, and Andrés Arnau. "Chemisorption of sulfur and sulfur-based simple molecules on Au(111)". In: *Journal of Physical Chemistry C* 111.33 (2007), pp. 12383–12390.

[104] Xintai Wang et al. "Scale-up of room-temperature constructive quantum interference from single molecules to self-assembled molecular-electronic films". In: *Journal of the American Chemical Society* (2020).

[105] Daniel K Schwartz. "Mechanisms and Kinetics of Self-Assembled Monolayer Formation". In: *Annu. Rev. Phys. Chem* 52 (2001), pp. 107–137.

[106] Kevin A Peterlinz and R Georgiadis. "In situ kinetics of self-Assembly by surface plasmon resonance spectroscopy". In: *Langmuir* 12.20 (1996), pp. 4731–4740.

[107] M Buck et al. "Adsorption kinetics of n -alkyl thiols on gold studied by second harmonic generation and x-ray photoelectron spectroscopy". In: *Journal of Vacuum Science & Technology A: Vacuum, Surfaces, and Films* 10.4 (1992), pp. 926–929.

[108] D. S. Karpovich and G. J. Blanchard. "Direct Measurement of the Adsorption Kinetics of Alkanethiolate Self-Assembled Monolayers on a Microcrystalline Gold Surface". In: *Langmuir* 10.1 (1994), pp. 3315–3322.

[109] Hans A. Biebuyck, Colin D. Bain, and George M. Whitesides. "Comparison of Organic Monolayers on Polycrystalline Gold Spontaneously Assembled from Solutions Containing Dialkyl Disulfides or Alkanethiols". In: *Langmuir* 10.6 (1994), pp. 1825–1831.

[110] C Vericat et al. "Self-assembled monolayers of thiols and dithiols on gold: new challenges for a well-known system". In: *Chemical Society Reviews* 39.5 (2010), pp. 1805–1834.

[111] Guohua Yang and Gang Yu Liu. "New insights for self-assembled monolayers of organothiols on Au(111) revealed by scanning tunneling microscopy". In: *Journal of Physical Chemistry B* 107.34 (2003), pp. 8746–8759.

[112] Frank Schreiber. *Structure and Growth of Self- Assembling Monolayers*. Tech. rep. September. 2014, pp. 151–256.

[113] Ludwig Bartels. "Tailoring molecular layers at metal surfaces". In: *Nature Chemistry* 2.2 (2010), pp. 87–95.

[114] Leonhard Grill et al. "Nano-architectures by covalent assembly of molecular building blocks". In: *Nature Nanotechnology* 2.11 (2007), pp. 687–691.

[115] Willi Auwärter et al. "Porphyrins at interfaces". In: *Nature Chemistry* 7.2 (2015), pp. 105–120.

[116] Jonas Björk, Felix Hanke, and Sven Stafström. "Mechanisms of halogen-based covalent self-assembly on metal surfaces". In: *Journal of the American Chemical Society* 135.15 (2013), pp. 5768–5775.

[117] Shawulienu Kezilebieke et al. "Hierarchy of Chemical Bonding in the Synthesis of Fe-Phthalocyanine on Metal Surfaces: A Local Spectroscopy Approach." In: *Journal of Physical Chemistry Letters* (2014).

[118] Sumanta Bhandary et al. "Manipulation of spin state of iron porphyrin by chemisorption on magnetic substrates". In: *Physical Review B* (2013).

[119] Stefanie Ditze et al. "Activation Energy for the Self-Metalation Reaction of 2H-Tetraphenylporphyrin on Cu(111)". In: *Angewandte Chemie* (2012).

[120] Rui Zhang et al. "Chemical mapping of a single molecule by plasmon-enhanced Raman scattering". In: *Nature* (2013).

[121] Katharina Diller et al. "Investigating the molecule-substrate interaction of prototypic tetrapyrrole compounds: Adsorption and self-metalation of porphine on Cu(111)". In: *Journal of Chemical Physics* (2013).

[122] Hannes Spillmann et al. "A two-dimensional porphyrin-based porous network featuring communicating cavities for the templated complexation of fullerenes". In: *Advanced Materials* 18.3 (2006), pp. 275–279.

[123] Tibor Kudernac et al. "Two-dimensional Supramolecular Self-assembly: Nanoporous networks on surfaces". In: *Chemical Society Reviews* 38.2 (2008), pp. 402–421.

[124] Alexander B Sorokin. *Phthalocyanine metal complexes in catalysis*. 2013.

[125] Francesco Sedona et al. "Tuning the catalytic activity of Ag(110)-supported Fe phthalocyanine in the oxygen reduction reaction". In: *Nature Materials* (2012).

[126] Zhexin Zhu et al. "Catalytic degradation of recalcitrant pollutants by Fenton-like process using polyacrylonitrile-supported iron (II) phthalocyanine nanofibers: Intermediates and pathway." In: *Water Research* (2016).

[127] Wangyang Lu et al. "The role of multiwalled carbon nanotubes in enhancing the catalytic activity of cobalt tetraaminophthalocyanine for oxidation of conjugated dyes". In: *Carbon* (2009).

[128] Cristina Isvoranu et al. "Pyridine adsorption on single-layer iron phthalocyanine on Au(111)". In: *Journal of Physical Chemistry C* 115.41 (2011), pp. 20201–20208.

[129] Simon Watson et al. "Challenges and developments of self-assembled monolayers and polymer brushes as a green lubrication solution for tribological applications". In: *RSC Advances* 5.109 (2015), pp. 89698–89730.

[130] Jason J Davis et al. "Mechanically interlocked and switchable molecules at surfaces". In: *Chemical Communications* (2010).

[131] Bruno Schmaltz, Tanja Weil, and Klaus Müllen. "Polyphenylene-Based Materials: Control of the Electronic Function by Molecular and Supramolecular Complexity". In: *Advanced Materials* (2009).

[132] Paul E. Laibinis et al. "Comparisons of Self-Assembled Monolayers on Silver and Gold: Mixed Monolayers Derived from HS(CH2)21X and HS(CH2)10Y (X, Y = CH3, CH2OH) Have Similar Properties". In: *Langmuir* 7.12 (1991), pp. 3167–3173.

[133] V S Dilimon et al. "Self-assembled monolayer formation on copper: A real time electrochemical impedance study". In: *Journal of Physical Chemistry C* 115.37 (2011), pp. 18202–18207.

[134] Paul E Laibinis et al. "Comparison of the Structures and Wetting Properties of Self-Assembled Monolayers of n-Alkanethiols on the Coinage Metal Surfaces, Cu, Ag, Au". In: *Journal of the American Chemical Society* 113.19 (1991), pp. 7152–7167.

[135] Angelo Lamantia. "THERMOELECTRIC PROPERTIES OF ULTRA-THIN FILM FORMED BY MOLECULAR SELF ASSEMBLY AND LANGMUIR-BLODGETT DEPOSITION". PhD thesis. 2020, p. 226.

[136] Peter Wagner et al. "Formation and in Situ Modification of Monolayers Chemisorbed on Ultraflat Template-Stripped Gold Surfaces". In: *Langmuir* 11.10 (1995), pp. 3867–3875.

[137] Emily A. Weiss et al. "Si/SiO2-templated formation of ultraflat metal surfaces on glass, polymer, and solder supports: Their use as substrates for self-assembled monolayers". In: *Langmuir* 23.19 (2007), pp. 9686–9694.

[138] Andrzej Wieckowski. *Interfacial Electrochemistry: Theory: Experiment, and Applications*. 1999.

[139] Thomas Michely, Karl H. Besocke, and George Comsa. "Observation of sputtering damage on Au(111)". In: *Surface Science* 230.1-3 (1990).

[140] C. Lu and A. W. Czanderna. *Applications of Piezoelectric Quartz Crystal Microbalances*. 1984.

[141] *The sensitivity distribution at the QCM crystal surface.*

[142] Günter Sauerbrey. "Verwendung von Schwingquarzen zur Wägung dünner Schichten und zur Mikrowägung". In: *Zeitschrift für Physik* 155.2 (1959), pp. 206–222.

[143] A. Dayo, W. Alnasrallah, and J. Krim. "Superconductivity-dependent sliding friction". In: *Physical Review Letters* 80.8 (1998), pp. 1690–1693.

[144] L. Bruschi et al. "Ultrahigh vacuum apparatus for quartz crystal microbalance measurements in the temperature range 4-400 K". In: *Review of Scientific Instruments* 76.2 (2005), pp. 2–7.

[145] J. Krim, D. H. Solina, and R. Chiarello. "Nanotribology of a Kr Monolayer: A Quartz-Crystal Microbalance Study of Atomic-Scale Friction". In: *Physical Review Letters* 66.2 (1991), p. 181.

[146] Lucía Herrer, Santiago Martín, and Pilar Cea. *Nanofabrication techniques in large-area molecular electronic devices*. 2020.

[147] Colin. D. Bain, Joe Evall, and George M. Whitesides. "Formation of Monolayers by the Coadsorption of Thiols on Gold: Variation in the Head Group, Tail group, and Solvent". In: *J. Am. Chem. Soc* 111.18 (1989), p. 7155.

[148] Daniel Käfer et al. "A comprehensive study of self-assembled monolayers of anthracenethiol on gold: Solvent effects, structure, and stability". In: *Journal of the American Chemical Society* 128.5 (2006), pp. 1723–1732.

[149] Jun Ki Ahn et al. "Vapor-phase deposition-based self-assembled monolayer for an electrochemical sensing platform". In: *AIP Advances* 10.4 (2020).

[150] Ernst Bauer. "Phänomenologische Theorie der Kristallabscheidung an Oberflächen. I". In: *Zeitschrift Fur Kristallographie* (1958).

[151] John A. Venables. *Introduction to Surface and Thin Film Processes*. Vol. 31. 9. 2000.

[152] Li Nan, D Allan, and Liu Gang-Yu. "In situ STM study of thermal annealing of Au thin films: An investigation on decay of nanometer Au clusters and 2D islands". In: *Acta Phys. Sin. (Overseas Edn)* 6 (1997), p. 531.

[153] G. Binning and H. Rohrer. "Scanning tunneling microscopy". In: *Surface Science* 126 (1983), p. 236.

[154] G. Binning, C. F. Quate, and Ch. Gerber. "Atomic Force Microscope". In: *Physical Review Letters* 56.9 (1986), pp. 930–934.

[155] Naoyuki Ishida and Vincent S.J. Craig. *Direct measurement of interaction forces between surfaces in liquids using atomic force microscopy*. 2019.

[156] G. Binnig et al. "Atomic resolution with atomic force microscope". In: *Europhysics Letters* 3.12 (1987), pp. 1281–1286.

[157] Gerhard Meyer and Nabil M Amer. "Optical-beam-deflection atomic force microscopy: The NaCl (001) surface". In: *Applied Physics Letters* 56.21 (1990), pp. 2100–2101.

[158] Franz J. Giessibl. "AFM's path to atomic resolution". In: *Materials Today* 8.5 (2005), pp. 32–41. arXiv: `0503671 [cond-mat]`.

[159] D. Rugar and P. Hansma. "Atomic force microscopy". In: *Phys. Today* 43 (1990), p. 23.

[160] F J Giessibl and G Binnig. "Investigation of the (001) cleavage plane of potassium bromide with an atomic force microscope at 4.2 K in ultra-high vacuum". In: *Ultramicroscopy* 42-44.PART 1 (1992), pp. 281–289.

[161] F Ohnesorge and G. Binning. "True Atomic Resolution by Atomic Force Microscopy Through Repulsive and Attractive Forces". In: *Science* 260 (1993), p. 1451.

[162] T R Albrecht et al. "Frequency modulation detection using high-Q cantilevers for enhanced force microscope sensitivity". In: *Journal of Applied Physics* 69.2 (1991), pp. 668–673.

[163] Ricardo García. *Amplitude Modulation Atomic Force Microscopy*. 2010.

[164] Takeshi Fukuma et al. "True-molecular resolution imaging by frequency modulation atomic force microscopy in various environments". In: *Applied Physics Letters* 86.3 (2005), pp. 1–3.

[165] B W Hoogenboom et al. "Quantitative dynamic-mode scanning force microscopy in liquid". In: *Applied Physics Letters* 88.19 (2006), p. 193109.

[166] Y Martin, C C Williams, and H K Wickramasinghe. "Atomic force microscope-force mapping and profiling on a sub 100-Å scale". In: *Journal of Applied Physics* 61.10 (1987), pp. 4723–4729.

[167] Ewelina Lipiec et al. *Revealing dna structure at liquid/solid interfaces by afm-based high-resolution imaging and molecular spectroscopy*. 2021.

[168] Lucel Sirghi, Robert Szoszkiewicz, and Elisa Riedo. "Volume of a nanoscale water bridge". In: *Langmuir* 22.3 (2006), pp. 1093–1098.

[169] J Colchero, A Gil, and A M Baró. "Resolution enhancement and improved data interpretation in electrostatic force microscopy". In: *Physical Review B - Condensed Matter and Materials Physics* 64.24 (2001).

[170] B Mokaberi and A. A.G. Requicha. "Towards automatic nanomanipulation: Drift compensation in scanning probe microscopes". In: *Proceedings - IEEE International Conference on Robotics and Automation*. Vol. 2004. 1. 2004, pp. 416–421.

[171] AFMWorkshop. *Measuring and Understanding Force Distance Curves*. Tech. rep. 888. 2020, pp. 4–6.

[172] Franz J Giessibl. *High-speed force sensor for force microscopy and profilometry utilizing a quartz tuning fork*. 1998.

[173] Leo Gross et al. "The Chemical Structure of a Molecule Resolved by Atomic Force Microscopy". In: *Science* 325.August (2009), pp. 1110–4.

[174] Henrry M Osorio et al. "Electrical characterization of single molecule and Langmuir-Blodgett monomolecular films of a pyridineterminated oligo(phenyleneethynylene) derivative". In: *Beilstein Journal of Nanotechnology* 6.1 (2015), pp. 1145–1157.

[175] John F. Watts and John Wolstenholme. *An Introduction to Surface Analysis by XPS and AES*. 2003.

[176] D Briggs and M. P. Seah. *Practical Surface Analysis, Auger and X-ray Photoelectron Spectroscopy*. 1990, pp. 7–12.

[177] Grzegorz Greczynski and Lars Hultman. "A step-by-step guide to perform x-ray photoelectron spectroscopy". In: *J. Appl. Phys* 132 (2022), p. 11101.

[178] U. Gelius. "Recent progress in ESCA studies of gases". In: *Journal of Electron Spectroscopy and Related Phenomena* 5.1 (1974), pp. 985–1057.

[179] Oksana Travnikova et al. "The ESCA molecule - Historical remarks and new results". In: *Journal of Electron Spectroscopy and Related Phenomena* 185.8-9 (2012), pp. 191–197.

[180] Caroline M Whelan et al. "An XPS study of heterocyclic thiol self-assembly on Au(111)". In: *Applied Surface Science* 134.1-4 (1998), pp. 144–158.

[181] T L Freeman, S D Evans, and A Ulman. "XPS Studies of Self-Assembled Multilayer Films". In: *Langmuir* 11.11 (1995), pp. 4411–4417.

[182] David G Castner, Kenneth Hinds, and David W Grainger. "X-ray photoelectron spectroscopy sulfur 2p study of organic thiol and bisulfide binding interactions with gold surfaces". In: *Langmuir* 12.21 (1996), pp. 5083–5086.

[183] Sirnegeda D Techane, Lara J Gamble, and David G Castner. "X-ray photoelectron spectroscopy characterization of gold nanoparticles functionalized with amine-terminated alkanethiols". In: *Biointerphases* 6.3 (2011), pp. 98–104.

[184] Didier Astruc. "Why is Ferrocene so Exceptional?" In: *European Journal of Inorganic Chemistry* 2017.1 (2017), pp. 6–29.

[185] Amanda L Eckermann et al. "Electrochemistry of redox-active self-assembled monolayers". In: *Coordination Chemistry Reviews* 254.15-16 (2010), pp. 1769–1802.

[186] Adwitiya Pal, Sushil Ranjan Bhatta, and Arunabha Thakur. "Recent advances in the development of ferrocene based electroactive small molecules for cation recognition: A comprehensive review of the years 2010–2020". In: *Coordination Chemistry Reviews* 431 (2021).

[187] Lucy E. Wilson et al. "Ferrocene- and Biferrocene-Containing Macrocycles towards Single-Molecule Electronics". In: *Angewandte Chemie - International Edition* 56.24 (2017), pp. 6838–6842.

[188] María Camarasa-Gómez et al. "Mechanically Tunable Quantum Interference in Ferrocene-Based Single-Molecule Junctions". In: *Nano Letters* 20.9 (2020), pp. 6381–6386.

[189] Stephanie A Getty et al. "Near-perfect conduction through a ferrocene-based molecular wire". In: *Physical Review B - Condensed Matter and Materials Physics* 71.24 (2005).

[190] Marc Vollmann and Holger Butenschön. "Synthesis of a functionalized dialkynylferrocene for molecular electronics". In: *Comptes Rendus Chimie* 8.8 SPEC. ISS. (2005), pp. 1282–1285.

[191] Ke Wang et al. "Preparation and characterization of pH-sensitive hydrogel for drug delivery system". In: *RSC Advances* 2.20 (2012), pp. 7772–7780.

[192] Qi Lu et al. "Enhancing molecular conductance of oligo(p-phenylene ethynylene)s by incorporating ferrocene into their backbones". In: *Journal of Physical Chemistry C* 116.33 (2012), pp. 17853–17861.

[193] Yan Yan Sun et al. "Enhancing electron transport in molecular wires by insertion of a ferrocene center". In: *Physical Chemistry Chemical Physics* 16.6 (2014), pp. 2260–2267.

[194] Luke J. O'Driscoll and Martin R Bryce. "A review of oligo(arylene ethynylene) derivatives in molecular junctions". In: *Nanoscale* 13.24 (2021), pp. 10668–10711.

[195] Yuru Liu et al. "Charge transport through molecular ensembles: Recent progress in molecular electronics". In: *Chemical Physics Reviews* 2.2 (2021), p. 021303.

[196] Andrea Moneo et al. "Towards molecular electronic devices based on 'all-carbon' wires". In: *Nanoscale* 10.29 (2018), pp. 14128–14138.

[197] Davood Taherinia. "Investigation of the interfacial electron transfer kinetics in ferrocene-terminated oligophenyleneimine self-assembled monolayers". In: *Langmuir* 36.42 (2020), pp. 12572–12579.

[198] Toshikazu Kitagawa et al. "Ideal redox behavior of the high-density self-assembled monolayer of a molecular tripod on a Au(111) surface with a terminal ferrocene group". In: *Langmuir* 29.13 (2013), pp. 4275–4282.

[199] Bruno Fabre et al. "Micropatterned ferrocenyl monolayers covalently bound to hydrogen-terminated silicon surfaces: Effects of pattern size on the cyclic voltammetry and capacitance characteristics". In: *Langmuir* 30.24 (2014), pp. 7235–7243.

[200] Luke A Wilkinson et al. "Supporting Information Assembly, structure and thermoelectric properties of 1,1'-dialkynylferrocene 'hinges'". In: (2022).

[201] Ekkehard Lindner et al. "Preparation, properties, and reactions of metal-containing heterocycles 1 Part CVIII. A novel generation of rigid, nanoscaled 1,1'-ferrocenediyl-bridged bis(pyridine), bis(bipyridine), and bis(phenanthroline) ligands". In: *Journal of Organometallic Chemistry* 660 (2002), pp. 78–84.

[202] Ekkehard Lindner, Ruifa Zong, and Klaus Eichele. "Syntheses and Characterization of 1,1'-Bis(3- Pyridylethynyl)Ferrocene and 1,1'-Bis(4- Pyridylethynyl)Ferrocene". In: *Phosphorus, Sulfur and Silicon* 169 (2001), pp. 219–222.

[203] Tobias Wachter et al. “Pyridine as a Resonantly Addressable Group to Study Electron- Transfer Dynamics in Self-Assembled Monolayers”. In: *J. Phys. Chem. C* 122 (2018), pp. 12534–12544.

[204] Christophe Silien et al. “Self-assembly of a pyridine-terminated thiol monolayer on Au(111)”. In: *Langmuir* 25.2 (2009), pp. 959–967.

[205] Yan Zubavichus et al. “X-ray Photoelectron Spectroscopy and Near-Edge X-ray Absorption Fine Structure Study of Water Adsorption on Pyridine-Terminated Thiolate Self-Assembled Monolayers”. In: *Langmuir* 20 (2004), pp. 11022–11029.

[206] K L Johnson, K Kendall, and A D Roberts. “Surface energy and the contact of elastic solids”. In: *Proceedings of the Royal Society of London* 324.1558 (1971), pp. 301–313.

[207] N. A. Burnham, R. J. Colton, and H. M. Pollock. “Work-Function Anisotropies as an Origin of Long-Range Surface Forces Institut”. In: *Physical Review Letters* 69.2 (1992), p. 246.

[208] Ali Ismael et al. “Tuning the thermoelectrical properties of anthracene-based self-assembled monolayers”. In: *Chemical Science* 11.26 (2020), pp. 6836–6841.

[209] Taekyeong Kim et al. “Determination of energy level alignment and coupling strength in 4,4-bipyridine single-molecule junctions”. In: *Nano Letters* 14.2 (2014), pp. 794–798.

[210] Emma J Dell et al. “Molecular length dictates the nature of charge carriers in single-molecule junctions of oxidized oligothiophenes”. In: *Nature Chemistry* 7.3 (2015), pp. 209–214.

[211] Marie Caroline Bourg, Antonella Badia, and R. Bruce Lennox. “Gold-sulfur bonding in 2D and 3D self-assembled monolayers: XPS characterization”. In: *Journal of Physical Chemistry B* 104.28 (2000), pp. 6562–6567.

[212] J E Baio et al. “Amine terminated SAMs: Investigating why oxygen is present in these films”. In: *Journal of Electron Spectroscopy and Related Phenomena* 172.1-3 (2009), pp. 2–8.

[213] Bin Li et al. “Ferrocene particles incorporated into Zr-based metal-organic frameworks for selective phenol hydroxylation to dihydroxybenzenes”. In: *RSC Advances* 7.61 (2017), pp. 38691–38698.

[214] A. P. Grosvenor et al. “Investigation of multiplet splitting of Fe 2p XPS spectra and bonding in iron compounds”. In: *Surface and Interface Analysis* 36.12 (2004), pp. 1564–1574.

[215] C M Woodbridge et al. “HREELS and XPS Studies of Ferrocene on Ag(100)”. In: *Journal of Physical Chemistry B* 104.14 (2000), pp. 3085–3093.

[216] Alasdair W. Taylor and Peter Licence. “X-ray photoelectron spectroscopy of ferrocenyl- and ferrocenium-based ionic liquids”. In: *ChemPhysChem* 13.7 (2012), pp. 1917–1926.

[217] D. O. Cowan et al. “X-Ray photoelectron spectroscopy of ferrocene compounds”. In: *Journal of the Chemical Society D: Chemical Communications* 1971.22 (1971), pp. 1444–1446.

[218] David B. Cook. “Broken symmetry in the electronic structure of the ferrocene molecule”. In: *International Journal of Quantum Chemistry* 43.2 (1992), pp. 197–207.

[219] Luke A Wilkinson et al. “Assembly, structure and thermoelectric properties of 1,1-dialkynylferrocene ‘hinges’”. In: *Chemical Science* 13.28 (2022), pp. 8380–8387.

[220] Troy Bennett et al. “Multi-Component Self-Assembled Molecular-Electronic Films: Towards New High-Performance Thermoelectric Systems”. In: *Chemical Science* 13 (2022), p. 5176.

[221] Chong Xiao et al. “Decoupling interrelated parameters for designing high performance thermoelectric materials”. In: *Accounts of Chemical Research* 47.4 (2014), pp. 1287–1295.

[222] Jian Liu et al. “N-type organic thermoelectrics: demonstration of ZT $>$ 0.3”. In: *Nature Communications* 11.1 (2020).

[223] Kun Zhang, Yue Zhang, and Shiren Wang. "Effectively decoupling electrical and thermal conductivity of polymer composites". In: *Carbon* 65 (2013), pp. 105–111.

[224] Yan Geng et al. "Magic Ratios for Connectivity-Driven Electrical Conductance of Graphene-like Molecules". In: *Journal of the American Chemical Society* 137.13 (2015), pp. 4469–4476.

[225] Markus Gantenbein et al. "Quantum interference and heteroaromaticity of para-and meta-linked bridged biphenyl units in single molecular conductance measurements". In: *Scientific Reports* 7.1 (2017).

[226] Mohsin K Al-Khaykanee et al. "Oscillating Seebeck coefficients in π-stacked molecular junctions". In: *RSC Advances* 8.44 (2018), pp. 24711–24715.

[227] Jeremy L Ruggles et al. "Interfacial behavior of tetrapyridylporphyrin monolayer arrays". In: *Langmuir* 22.2 (2006), pp. 681–686.

[228] Geoffrey J Ashwell et al. "Self-assembly of amino-thiols via gold-nitrogen links and consequence for in situ elongation of molecular wires on surface-modified electrodes". In: *Journal of Physical Chemistry C* 115.10 (2011), pp. 4200–4208.

[229] M Hasik et al. "XPS studies of nitrogen-containing conjugated polymers – palladium systems". In: *Surface Science* 510 (2002), pp. 916–921.

[230] David M Sarno, Luis J Matienzo, and Wayne E Jones. "X-ray photoelectron spectroscopy as a probe of intermolecular interactions in porphyrin polymer thin films". In: *Inorganic Chemistry* 40.24 (2001), pp. 6308–6315.

[231] David M Sarno et al. "Self-assembled molecular architectures on surfaces: New strategies involving metal-organic copolymers". In: *Langmuir* 16.15 (2000), pp. 6191–6199.

[232] Claudia Wöckel et al. "Pyridine on flat Pt (111) and stepped Pt (355) — An in situ HRXPS investigation of adsorption and thermal evolution". In: *J. Chem. Phys* 144 (2016).

[233] Johannes Poppenberg et al. “Successive coordination of palladium(II)-ions and terpyridine-ligands to a pyridyl-terminated self-assembled monolayer on gold”. In: *Surface Science* 606.3-4 (2012), pp. 367–377.

[234] Maurizio Muniz-Miranda et al. “SERS, XPS and DFT investigation on palladium surfaces coated with 2,2-bipyridine monolayers”. In: *Applied Surface Science* 457 (2018), pp. 98–103.

[235] Jianfang Jing et al. “Supramolecular Zinc Porphyrin Photocatalyst with Strong Reduction Ability and Robust Built-In Electric Field for Highly Efficient Hydrogen Production”. In: *Advanced Energy Materials* 11.29 (2021).

[236] Manuela S Killian et al. “ToF-SIMS and XPS studies of the adsorption characteristics of a Zn-porphyrin on TiO2”. In: *Langmuir* 26.5 (2010), pp. 3531–3538.

[237] Troy L R Bennett et al. “Electronic Supporting Information Multi-Component Self-Assembled Molecular-Electronic Films: Towards New High-Performance Thermoelectric Systems”. In: (2022).

[238] Li Shi and Arunava Majumdar. “Thermal transport mechanisms at nanoscale point contacts”. In: *Journal of Heat Transfer* 124.2 (2002), pp. 329–337.

[239] F Studener et al. “From hydrogen bonding to metal coordination and back: Porphyrin-based networks on Ag(111)”. In: *Journal of Chemical Physics* 142.10 (2015), p. 101926.

[240] T. Yokoyama et al. “Selective Assembly on a Surface of Supramolecular Aggregates with Controlled Size and Shape”. In: *Nature* 413 (2001), pp. 619–621.

[241] Nikolai Wintjes et al. “Supramolecular synthons on surfaces: Controlling dimensionality and periodicity of tetraarylporphyrin assemblies by the interplay of cyano and alkoxy substituents”. In: *Chemistry - A European Journal* 14.19 (2008), pp. 5794–5802.

[242] M. G. Walter, A. B. Rudine, and C. C. Wamser. “Porphyrins and Phthalocyanines in Solar Photovoltaic Cells”. In: *Journal of Porphyrins and Phthalocyanines* 14 (2010), pp. 759–792.

[243] X. Guo et al. "Zinc porphyrin-based electron donor–acceptor-conjugated microporous polymer for the efficient photocatalytic oxidative coupling of amines under visible light". In: *Applied Catalysis A* 590 (2020).

[244] Maxence Urbani et al. "Phthalocyanines for dye-sensitized solar cells". In: *Coordination Chemistry Reviews* 381 (2019), pp. 1–64.

[245] Anuj Kumar, Vinod Kumar Vashistha, and Deepak Kumar Das. "Recent development on metal phthalocyanines based materials for energy conversion and storage applications". In: *Coordination Chemistry Reviews* 431 (2021).

[246] Cristina Isvoranu et al. "Ammonia adsorption on iron phthalocyanine on Au(111): Influence on adsorbate-substrate coupling and molecular spin". In: *Journal of Chemical Physics* 134.11 (2011), p. 114710.

[247] Xiao Lei Zhang et al. "Identifying the Assembly Configuration and Fluorescence Spectra of Nanoscale Zinc-Tetraphenylporphyrin Aggregates with Scanning Tunneling Microscopy". In: *Scientific Reports* 6 (2016).

[248] Charles Ruggieri et al. "Zinc(II) tetraphenylporphyrin adsorption on Au(111): An interplay between molecular self-assembly and surface stress". In: *Journal of Physical Chemistry C* 119.11 (2015), pp. 6101–6110.

[249] Lieve G Teugels, L. Gaby Avila-Bront, and S J Sibener. "Chiral domains achieved by surface adsorption of achiral nickel tetraphenyl- or octaethylporphyrin on smooth and locally kinked Au(111)". In: *Journal of Physical Chemistry C* 115.6 (2011), pp. 2826–2834.

[250] Oreste De Luca et al. "Zinc(II) tetraphenylporphyrin on Au(111) investigated by scanning tunnelling microscopy and photoemission spectroscopy measurements". In: *Nanotechnology* 31.36 (2020).

[251] J V Barth et al. "Scanning tunneling microscopy observations on the reconstructed Au(111) surface: Atomic structure, long-range superstructure, rotational domains, and surface defects". In: *Physical Review B* 42.15 (1990), pp. 9307–9318.

[252] Luz M Ballesteros et al. "Single gold atom containing oligo(phenylene)ethynylene: Assembly into LB films and electrical characterization". In: *Journal of Physical Chemistry C* 119.1 (2015), pp. 784–793.

[253] Safia Izzaouihda et al. “Adsorption of imidazole on Au(111) surface: Dispersion corrected density functional study”. In: *Applied Surface Science* 383.May (2016), pp. 233–239.

[254] Sónia A.C. Carabineiro and Bernard E Nieuwenhuys. “Reactions of small molecules on gold single crystal surfaces”. In: *Gold Bulletin* 43.4 (2010), pp. 252–266.

[255] Rafal Zuzak, Marek Szymonski, and Szymon Godlewski. “Extended iron phthalocyanine islands self-assembled on a Ge(001):H surface”. In: *Beilstein Journal of Nanotechnology* 11 (2021), pp. 232–241.

[256] Y H Jiang et al. “Self-assembly of metal phthalocyanines on Pb(111) and Au(111) surfaces at submonolayer coverage”. In: *Journal of Physical Chemistry C* 115.44 (2011), pp. 21750–21754.

[257] Z H Cheng et al. “Epitaxial growth of iron phthalocyanine at the initial stage on Au(111) surface”. In: *Journal of Physical Chemistry C* 111.6 (2007), pp. 2656–2660.

[258] Sigma-Aldrich. *Greener Solvent Alternatives Supporting the Advancement of Chemistry through Sound Environmental, Social & Fiscal Responsibilities.* 2015.